A BACKSCATTER LIDAR FORWARD OPERATOR FOR AEROSOL-REPRESENTING ATMOSPHERIC CHEMISTRY MODELS

**Dissertation zur Erlangung des Doktorgrades
der Naturwissenschaften (Dr. rer. nat.)**

Fakultät Naturwissenschaften

Universität Hohenheim

Institut für Physik und Meteorologie

vorgelegt von
Armin Benjamin Geisinger

aus Kirchheim unter Teck

2019

Dekan   Prof. Dr. Uwe Beifuß
1. berichtende Person   Prof. Dr. Volker Wulfmeyer
2. berichtende Person   Prof. Dr. Roland Potthast
Eingereicht am: 04. Juli 2019
Mündliche Prüfung am: 13. März 2020

Die vorliegende Arbeit wurde am **13. März 2020** von der Fakultät Naturwissenschaften der Universität Hohenheim als „Dissertation zur Erlangung des Doktorgrades der Naturwissenschaften" angenommen.

ABSTRACT

State-of-the-art atmospheric chemistry models are capable of simulating the transport and evolution of aerosols and trace gases but there is a lack of reliable methods for model validation and data assimilation. Networks of automated ceilometer lidars (ACLs) could be used to fill this gap. These networks are already used for the detection of clouds and aerosols, providing a 3D dataset of atmospheric backscatter profiles. But as the aerosol number concentration cannot be obtained from the ACL data alone; one needs a backscatter-lidar forward model to simulate lidar profiles from the model variables. Such an operator allows then for a qualitative and quantitative model validation based on ACL data. In this work, a newly developed backscatter-lidar forward operator and the related sensitivity studies are presented and results of the forward operator applied on model output data are compared to measured ACL profiles in the frame of a case study. As case study, the eruption of the Icelandic volcano Eyjafjallajökull from 20 March 2010 to 24 May 2010 was chosen and extensively analyzed. The Consortium for Small-scale Modeling - Aerosols and Reactive Trace gases (COSMO-ART) model of DWD (Deutscher Wetterdienst) was operated during this event for ash-transport simulations over Europe. For the forward model, the attenuated backscatter coefficient is used as lidar-independent variable, which only relies on the laser wavelength. To calculate the attenuated backscatter coefficient, the size-dependent aerosol number concentration and the scattering properties of each aerosol type and size have to be simulated. While the aerosol number concentration is a model output variable, the scattering properties were determined by extensive scattering calculations. As these scattering calculations require assumptions about the aerosol refractive indices and shapes, sensitivity studies were performed to estimate the uncertainties related to the particle properties as represented by the model system. The strong sensitivity of the scattering characteristics to the particle radius could be reduced by size-averaging algorithms. An analysis of the particle shape effect for the extinction and backscatter coefficients resulted in huge differences of the scattering properties between spherical, ellipsoidal and cylindrical particle shapes. Due to a particle shape mixture in typical volcanic ash plumes, the application of non-spherical scattering calculation methods for estimating the effective optical properties requires more information related to the particle shape distribution (specifically: a particle size and shape distribution). As such information was not available for the present case study, it was necessary to assume spherical shaped volcanic ash particles but estimate the uncertainty related to this assumption within the frame of additional sensitivity studies. Finally, the forward modeled lidar profiles were compared to ACL measurements from stations of the German ACL network. The comparison required an extraction of common time

and height intervals of the ACL and forward modeled COMSO-ART data as well as reshaping the datasets to the same vertical and temporal resolution. Significant differences between ACL profiles and the output of the forward operator applied to the COSMO-ART data were found. Some ash layer structures were at similar coordinates which is remarkable due to the uncertainties related to the model dynamics and the limited amount of measurement data that could be used for model validation. In detail, however, the major fraction of the compared time and height interval differed both in the relative signal intensity and the layer structures of the volcanic ash plume. Based on such quantitative comparison, a future data assimilation system could correct the model prediction of the forward modeled attenuated backscatter coefficient, the time of arrival, as well as the vertical structure of the volcanic ash plume. In summary, the continuous and distributed data stream provided by ACL stations was found to deliver valuable verification information for dispersion simulations of aerosol events. But major issues have been determined which limit current realizations of backscatter-lidar forward operators for aerosol transport simulations: First, it is suggested that the ACL systems improve their dynamic range and perform automatic calibration to increase the precision of ACL data and for calculating the measured attenuated backscatter coefficient with a minimum leftover of uncertainties. This will allow for the calculation of the attenuated backscatter coefficient in the presence of clouds as well as of faint aerosol signals. Second, the aerosols' scattering properties have to be analyzed even more extensively which includes both the variety of aerosol sizes or types as well as the size distribution information. From the findings within this study, the particle size distribution was indentified to be a critical component when using monodisperse size classes. To reduce the amount of time required for initializing the backscatter lidar forward operator in future studies and to provide high-quality look-up tables of scattering properties, the creation of an open-access scattering database for various scatterer types, sizes, and shapes would be a sustainable approach. Apart from that, this study presents a standalone backscatter lidar forward operator and the steps required for a qualitative and quantitative comparison of ACL measurement and aerosol dispersion simulation data during an aerosol dispersion event.

ZUSAMMENFASSUNG

Atmosphärenchemie-Modelle der aktuellen Generation können Transportvorgänge und chemische Veränderungen von Aerosolen und Spurengasen in der Atmosphäre simulieren und prognostizieren. Die Qualität und Validität der Simulation lässt sich mit den derzeit vorhandenen Messmitteln nur unzureichend beurteilen - geschweige denn mittels Datenassimilation verbessern, da umfassende und zuverlässig verfügbare Validierungsdaten sowie Validierungsmethoden praktisch nicht vorhanden sind. Einen Lösungsansatz - insbesondere für die Bereitstellung von Validierungsinformationen zu Aerosolbewegungen in der Atmosphäre - stellen Netzwerke aus automatisierten Ceilometer-Lidarsystemen (engl.: automated ceilometer lidars, ACL) dar. Diese Systeme werden üblicherweise für die Erkennung von Wolken eingesetzt, eignen sich jedoch auch für die Erkennung von Aerosolschichten wie Vulkanasche, Saharastaub und weiteren Aerosolarten. Durch den Zusammenschluss mehrerer vertikal messender oder scannender Lidar-Systeme kann ein dreidimensionaler Datensatz von atmosphärischen Rückstreuprofilen mit hoher vertikaler und sehr hoher zeitlicher Auflösung erzeugt werden. Diese Daten sind jedoch nicht direkt für die Validierung von Aerosoltransport-Vorhersagen verwendbar, da die Aerosolkonzentration einzelner Größenklassen oder Größenverteilungen nicht - oder nur unter bestimmten Annahmen - aus den Rückstreuprofilen ableitbar ist. Ein alternativer Ansatz besteht in der Simulation von Lidarprofilen auf Basis der vom Vorhersagemodell berechneten Atmosphärensituation und dem anschließenden Vergleich der simulierten und gemessenen Lidarprofile. Eine Implementierung eines solchen sogenannten Rückstreulidar-Vorwärtsoperators ist Gegenstand dieser Arbeit; ebenso die Analyse der Unsicherheiten im Rahmen von Sensitivitätsstudien sowie Vergleiche zwischen vorwärtsmodellierten Modell-Prognoseergebnissen und gemessenen Rückstreuprofilen im Fall des Vulkanausbruchs des Eyjafjallajökull (Island) im Jahr 2010. Hierfür wurden Simulationsergebnisse des Atmosphärenchemie-Modells COSMO-ART (Consortium for Small-scale Modeling - Aerosols and Reactive Trace gases) verwendet. Die in COSMO-ART mittels monodisperser Größenklassen beschriebenen Vulkanaschedaten bewirken eine sehr hohe Sensitivität der simulierten Streueigenschaften, sodass Methoden für eine repräsentative Berechnung der Rückstreuquerschnitte von Vulkanasche bei Verwendung von monodispersen Größenklassen entwickelt werden mussten. Durch Mittelungsverfahren konnte die Sensitivität des Rückstreuquerschnitts der dargestellten Größenklassen deutlich reduziert werden. Als gemeinsame physikalische Messgröße der gemessenen und simulierten Lidarprofilen wurde der sogenannte abgeschwächte Rückstreukoeffizient (engl.: attenuated backscatter coefficient) verwendet, da diese Größe - mit Ausnahme der eingesetzten Wellenlänge des emittierten Lichts - unabhängig von den

Eigenschaften des simulierten Lidargeräts ist. Für die Berechnung des abgeschwächten Rückstreukoeffizienten müssen die Streueigenschaften und Anzahldichten jeder relevanter, vom Modell abgebildeter Aerosolart berechnet werden. Während die Anzahl an Vulkanascheteilchen pro Größenklasse eine Ausgabegröße von COSMO-ART ist, waren für die Bestimmung der Streueigenschaften der im Modell vorhandenen Aerosolarten und -größenklassen umfangreiche Streuberechnungen nötig. Die Unsicherheiten der simulierten Lidarprofile wurden im Rahmen von Sensitivitätsstudien bezüglich komplexem Brechungsindex, Partikelform sowie Schwankungen der emittierten Wellenlänge des Lasers quantifiziert. Nach Anwenden des Vorwärtsoperators auf die Simulationsergebnisse von COSMO-ART und Berechnen des abgeschwächten Rückstreukoeffizienten aus Messdaten des Deutschen Ceilometernetzwerks wurden Modellprognose und Messung qualitativ und quantitativ miteinander verglichen. Der Vergleich an der Ceilometer-Station Deuselbach ergab signifikante Unterschiede zwischen Simulation und Messung: Die erkannten Ascheschichten und -strukturen waren nicht nur in ihrer Form und Position unterschiedlich, sondern auch in den absoluten Werten des abgeschwächten Rückstreukoeffizienten. Anhand dieser Arbeit konnten wesentliche Aspekte identifiziert werden, die die Validierung von Simulationsergebnissen mittels ACL Messungen unter Verwendung eines Rückstreu-Lidar Vorwärtsoperators bisher stark einschränken und für zukünftige Validierungsansätze zu deutlich aussagekräftigeren Ergebnissen führen werden: Die Erweiterung des dynamischen Messbereichs sowie eine automatisierte und transparente Kalibrierung der Ceilometer ist unabdingbar, um die Qualität des Referenzdatensatzes selbst zu verbessern. Eine Verbesserung der Vorwärtsoperator-Qualität wird primär durch weitere Analysen und Optimierungen zur Berechnung der effektiven Streueigenschaften der Aerosolklassen und -Arten erreicht, aber auch durch das Optimieren der Aerosol-Repräsentation im Vorhersagemodell. Dies beinhaltet sowohl das Erweitern der abgebildeten Aerosolarten (insbesondere Hintergrundaerosol) als auch der Optimierung der Aerosoldarstellung im Sinne von Modalen Darstellungen oder einer besseren Auflösung bestimmter Größenklassenbereiche. Vorhersagen zur Vulkanascheverteilung können jedoch mit dem hier vorgestellten Rückstreu-Lidar Vorwärtsoperator basierend auf reinen Rückstreuprofil-Messungen bestehender ACL Systeme bewertet und verifiziert bzw. falsifiziert werden.

ACKNOWLEDGMENTS

CONTENTS

viii

LIST OF FIGURES

LIST OF TABLES

ACRONYMS

COSMO-ART Consortium for Small-scale Modeling, Aerosols and Reactive Trace gases

COSMO-MUSCAT Multiscale Chemistry Aerosol Transport

ECMWF European Center for Mesoscale Weather Forecast

ENVIRO-HIRLAM Environment - High Resolution Limited Area Model

MACC-II Monitoring Atmospheric Composition and Climate - Interim
Implementation

MesoNH Non-Hydrostatic Mesoscale Atmospheric Model of the French Research
Community

WRF-CHEM Weather Research and Forecast Model coupled to Chemistry

MCCM Multiscale Coupled Chemistry Model

DWD   Deutscher Wetterdienst

OPS   Optical Particle Spectrometer

Lidar Light Detection and Ranging

UV   Ultraviolet

DIAL Differential Absorption Lidar

RRL   Rotational Raman Lidar

HSRL High Spectral Resolution Lidar

ACL   Automated Ceilometer Lidar Systems

AOD   Atmosphere Optical Depth

CTM-MOCAGE Chemical-Transport Model, Modèle de Chimie Atmosphérique à Grande Echelle

aerFO Cloud-Free Aerosol Forward Operator

EURAD-IM European Air Pollution and Dispersion - Inverse Model

BaLiFOp Backscatter Lidar Forward Operator

DDA   Discrete Dipole Approximation

IDL   Interactive Data Language

AOPP Department of Atmospheric, Oceanic and Planetary Physics

ACP   Atmospheric Chemistry and Physics Journal

SEVIRI Spinning Enhanced Visible and Infrared Imager

MODIS Moderate Resolution Imaging Spectroradiometer

NASA National Aeronautics and Space Administration

CALIPSO Cloud-Aerosol Lidar and Infrared Pathfinder Satellite Observations

CALIOP Cloud-Aerosol Lidar with Orthogonal Polarization

NetCDF Network Common Data Form

SNR   Signal-To-Noise-Ratio

KIT   Karlsruhe Institute of Technology

ASCII   American Standard Code for Information Interchange

DLR   German Aerospace Center

LUT   Look-Up Table

ASL   Above Sea Level

ESA   European Space Agency

EarthCARE   Earth Clouds, Aerosols and Radiation Explorer

EARLINET   European Aerosol Research Lidar Network

E-PROFILE   EUMETNET Profiling Programme

NWP   Numerical Weather Prediction

1 INTRODUCTION

In Spring 2010, the Icelandic volcano Eyjafjallajökull erupted several times. The emitted ash was found to be harmful for aircraft and due to uncertain information about spatial distribution and concentration of volcanic ash, the European air space was closed for several days (Sandrini et al., 2014). The high economic costs and impact on public transport lead to efforts of DWD to improve at monitoring and predicting ash plumes in the atmosphere. Therefore, DWD decided to start a dedicated project on backscatter lidar forward operators for validating aerosol dispersion models using available remote-sensing measurement data and for future assimilation of lidar backscatter and extinction data.

Atmospheric chemistry models which allow for aerosol dispersion predictions are, amongst others, COSMO-ART (Consortium for Small-scale Modeling, Aerosols and Reactive Trace gases, Vogel et al. (2009)), COSMO-MUSCAT (Multiscale Chemistry Aerosol Transport, Wolke et al. (2004)), ECMWF (European Center for Mesoscale Weather Forecast, Benedetti (2009)), ENVIRO-HIRLAM (Environment - High Resolution Limited Area Model, Zakey, Solmon, and Giorgi (2006)), MACC-II (Monitoring Atmospheric Composition and Climate - Interim Implementation, Cuevas et al. (2015)), MCCM (Multiscale Coupled Chemistry Model, Emeis et al. (2011)), MesoNH (Non-Hydrostatic Mesoscale Atmospheric Model of the French Research Community, Mallet et al. (2009)), WRF-CHEM (Weather Research and Forecast Model coupled to Chemistry, Chen et al. (2014)). Using these model systems, scientists have analyzed the aerosol influence on, for example, precipitation (Rieger et al., 2014), temperature (Bangert et al., 2012), radiative fluxes (Vogel et al., 2009), and convection initiation (Chaboureau et al., 2011). These models are potentially capable of simulating such ash dispersion scenarios and could thus benefit from the methodology presented here.

The simulation of aerosols can be separated in components: sources, sinks and evolution as well as transport processes in between. While the transport processes are similar for any aerosol type with only sedimentation being potentially different, the sources and sinks have to be described individually. For example, the emission rate of mineral dust from deserts depends on the wind speed near ground (Vogel et al., 2014). Processes leading to sinks are washout, chemical reactions, and particle aggregation. The transport processes mainly depend on the model dynamics (wind speed, wind direction) and sedimentation properties of each individual aerosol type. In consequence, the validation of aerosol transport model simulations with observations allows not only for the validation of the sources and sinks but serves also to validate the model dynamics. If such validation can be done automatically, data assimilation is the next step to continuously converge simulation and reality. Compared to other atmospheric

variables such as pressure and temperature, there are - to the best of knowledge - no comprehensive measurement systems in use so far to validate aerosol simulations operationally.

In-situ instruments allow for the quantitative measurement of the aerosol number concentration as well as aerosol number-size distributions but the number of operationally-available measurement stations is very low. For a model validation attempt using in-situ aerosol measurements, for example in Germany, there are only two Optical Particle Spectrometer (OPS) devices operated by the national meteorological service DWD. To make matters worse, these instruments are limited to particle diameters ranging from 12 nm to 900 nm and from 0.25 µm to 31 µm[1]. Consequently, the spatial and vertical density of measurements as well as the particle size range is of limited use for reliable validation of aerosol dispersion simulations.

Light Detection and Ranging (Lidar) is capable of providing information on atmospheric particles with high temporal and spatial resolution. The most basic lidar type is the backscatter lidar which measures the backscattered signal intensity of a volume at a certain range. Comparing the data of such a backscatter lidar that is operated in the Ultraviolet (UV) with simulations of an atmospheric chemistry model, allows, e.g., for the characterization of transport and optical properties of aerosol particles near sources (Behrendt et al., 2011; M. Valdebenito B et al., 2011). Using ground-based DIAL (Differential Absorption Lidar, Dagan (2008) and Späth et al. (2016)), water-vapor can be measured, which can even be combined with backscatter measurements to derive more details of aerosol particle properties (Wulfmeyer and Feingold, 2000). Lidar techniques based on the vibrational and rotational Raman effect, like Rotational Raman Lidar (RRL) allow for the measurement of trace gas profiles (Whiteman, Melfi, and Ferrare, 1992; Turner et al., 2002; Wulfmeyer et al., 2010; Haarig et al., 2016), as well as profiles of atmospheric temperature, particle backscatter cross section, particle extinction cross section, and particle depolarization properties (Behrendt et al., 2002; Hammann et al., 2015; Radlach, Behrendt, and Wulfmeyer, 2008). High Spectral Resolution Lidar (HSRL) systems furthermore allow for cloud and particle characterization (Shipley et al., 1983). Multi-wavelength lidar systems offer the potential to retrieve the optical, microphysical and chemical properties of aerosols (Mamouri et al., 2012) but these systems are rare and the inversion algorithms are very complex. Profiles of the radial wind speed can be obtained by Doppler-Lidar systems, e.g., Banta et al. (2012).

While the number of sophisticated lidar instruments that provide thermodynamic data is still low (Wulfmeyer et al., 2015), there are already automated aerosol lidar networks in operation in Europe and Asia (Pappalardo et al., 2014; Sugimoto et al., 2008). The data of such a network offers 3D particle information with a high temporal, high vertical, and a moderate horizontal resolution. ACL have been used to detect cloud and boundary layer heights (Emeis, Schäfer, and Münkel, 2009) but the received

---

[1] https://www.dwd.de/EN/research/observing_atmosphere/composition_atmosphere/aerosol/cont_nav/particle_size_distribution_node.html

signal delivers also information about aerosols. It is therefore worthwhile to use the ACL network measurements for the validation of particle transport model simulations. Unfortunately, it is not possible to obtain the particle number concentration from an elastic backscatter signal alone without ancillary information and assumptions which are partly critical. The alternative way is using the detailed atmospheric description of the model to simulate lidar profiles for a model-given atmospheric state. Such a lidar simulator is called lidar forward operator. Using an ideal lidar forward operator, the signal of a given lidar system can be calculated from the model prediction at any time interval, grid location, and measurement direction.

There are already several backscatter lidar forward operators available or in development. At European Center for Mesoscale Weather Forecast (ECMWF), a lidar forward operator was developed and tested in an ice cloud scenario (Benedetti, 2009), based on assumptions concerning the lidar ratio S_{lidar}. Newer implementations of the ECMWF model allow for simulating the backscatter coefficient measurement of CALIOP at two wavelengths 532 nm and 1064 nm for spherical sea salt and mineral dust particles (Morcrette et al., 2009). The lidar forward model of SIČ (2014) has the capability to calculate the Atmosphere Optical Depth (AOD) and the aerosol extinction coefficient from simulations of the Chemical-Transport Model, Modèle de Chimie Atmosphérique à Grande Echelle (CTM-MOCAGE). But similar to the ECMWF forward operator, assumptions on the lidar ratio S_{lidar} are mandatory to calculate the particle backscatter coefficient.

At MetOffice, UK, the Cloud-Free Aerosol Forward Operator (aerFO, Warren et al. (2018)) is being investigated which is also based on the assumption of fixed values for the lidar ratio S_{lidar}. Another lidar forward model is being developed for the EURAD-IM (European Air Pollution and Dispersion - Inverse Model, Lange and Elbern (2014)), but no published results have been found in literature. These backscatter lidar forward operators are based on forward modeling the extinction coefficient and calculating the backscatter coefficient from the extinction coefficient by assuming a fixed lidar ratio. The backscatter coefficient, however, is not calculated explicitly for given atmospheric scatterer species. On the one hand, this method benefits from the fact that the extinction coefficient is less sensitive to the particle dimension and shape than the backscatter coefficient. On the other hand, the precision of this method is limited to the correctness of assumed lidar ratio values. The method becomes furthermore unusable once there is a mixture of scatterers.

To become independent of the assumption of a lidar ratio, a forward operator was developed which is based on the distinct calculation of extinction and the backscatter coefficients in the model system. This forward operator can be adapted to particle-representing atmospheric model and backscatter lidar systems even using multiple wavelengths. It has the capability to calculate both the attenuated backscatter coefficient and the lidar ratio from model output data with a minimum set of external
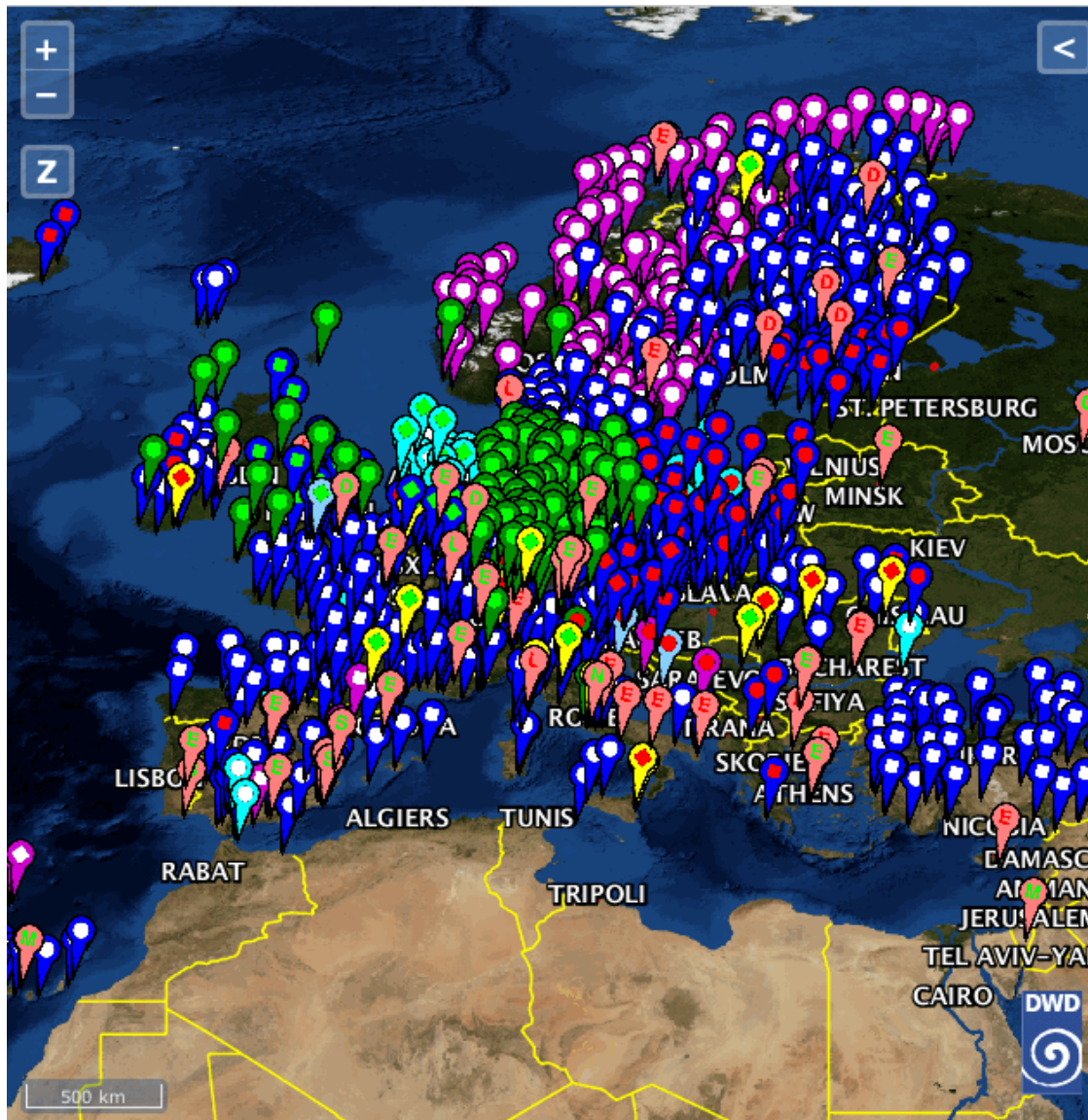
Figure 1.1: Automated lidar devices in Europe displayed by the DWD Ceilometer Viewer (https://www.dwd.de/EN/research/projects/ceilomap/ceilomap_node.html). Each needle represents one lidar station which could potentially be used for model validation of aerosol transport simulations.

information. The name of the forward model is Backscatter Lidar Forward Operator (BaLiFOp)

In Chapter 2, the lidar principles and the theoretical background for the backscatter lidar forward operator is explained. This is followed by an introduction to the case study in Chapter 3. Sensitivity studies of the aerosols' scattering properties are presented in Chapter 4. Results of the forward operator and a comparison to ACL measurement data are shown in Chapter 5. Finally, both the benefits and the requirements of ACL data assimilation systems are discussed in Chapter 6.

2 THEORY OF BACKSCATTER LIDAR

The lidar principle is based on the emission of laser pulses into the atmosphere and the measurement and analysis of the backscatter signals. The received photon number per pulse $N_{rec,\lambda}(z)$ from range z is described by the following equation for elastic backscatter lidars which detect the backscatter signal at the emitted wavelength

$$N_{rec,\lambda}(z) = N_{tr,\lambda} \frac{\tau c}{2} \, \eta_\lambda \, O(z) \, \frac{A_{tel}}{z^2} \, \beta_\lambda(z) \, \exp\left(-2\int_0^z \alpha_\lambda(z') \, dz'\right). \tag{2.1}$$

Instrument-dependent variables of the lidar equation are the wavelength λ, the laser emitted photon number per pulse $N_{tr,\lambda}$, the temporal length of a laser pulse τ, the efficiency of the receiving system and detectors η_λ, the overlap function $O(z)$, and the net area of the receiving telescope A_{tel}. The received signal intensity can be given either as power or in photon counts. Here, we use photon counts per laser pulse unless otherwise noted.

The range resolution is usually matched to the temporal resolution of the data acquisition system by $\frac{\tau c}{2} = \Delta z$ with c as speed of light. Typical Δz values for ACL systems are a few meters. The overlap function $O(z)$ is zero (no overlap) near ground and becomes 1 (full overlap) above a certain height which is typically 200 m to 1500 m above ground for ACL systems (Wiegner et al., 2014; Flentje et al., 2010b). The missing overlap limits the capability to measure and calibrate in near range but has no effect where full overlap has accomplished. Heights where $0 < O(z) < 1$ can be overlap-corrected if the device-specific overlap function is known. A sketch of the lidar measurement geometry is Fig. 2.1.

Processes in the atmosphere are described by the backscatter coefficient $\beta_\lambda(z)$ and the extinction coefficient $\alpha_\lambda(z)$. The backscatter coefficient $\beta_\lambda(z)$ is the scattering strength into the direction of the receiving telescope and depends on wavelength, type, shape and size of scatterers, and their respective number-concentrations; $\beta_\lambda(z)$ is given in units of $m^{-1} \, sr^{-1}$. The extinction coefficient $\alpha_\lambda(z)$ is a description for laser radiation absorption and scattering capabilities of objects in a volume; it is given in units of m^{-1}.

Elastic backscatter lidar systems do not allow for a separate measurement of $\beta_\lambda(z)$ and $\alpha_\lambda(z)$ as two unknowns cannot be determined with one measured variable. For

receiver field of view

laser beam

R   t

laser
pulse

A_L

scattering volume

V $\Delta h(z)$

z_1 τ

z_2 $\tau/2$

effective
pulse length

A/z^2

perception angle

A

telescope area
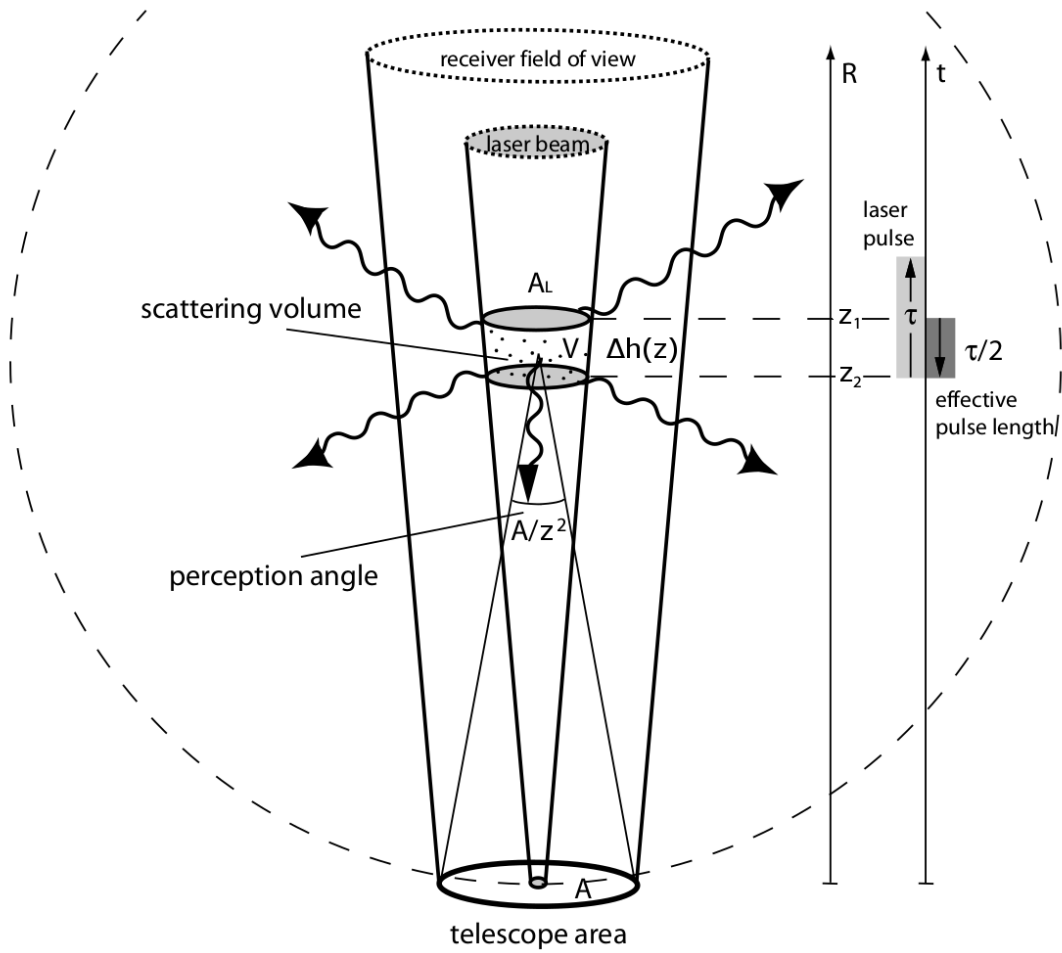
Figure 2.1: Lidar measurement geometry, adapted from (Weitkamp, 2005).

calibrated backscatter lidar systems, it is thus convenient to calculate the attenuated backscatter coefficient $\gamma_\lambda(z)$ from the measured profiles

$$\gamma_\lambda(z) = \beta_\lambda(z) \, \exp\left(-2\int_0^z \alpha_\lambda(z') \, dz'\right). \tag{2.2}$$

It is given in units of $m^{-1} \, sr^{-1}$. The attenuated backscatter coefficient is independent of all instrument-specific parameters except the wavelength. Therefore, it is the best suitable physical quantity for a comparison between backscatter lidar measurement and aerosol model using a forward operator as long as no ACL measurements of extinction and backscatter cross section profiles are available for this purpose.

2.1 PRINCIPLE OF THE BACKSCATTER LIDAR FORWARD OPERATOR

According to Eq. (2.2), the basic functionality of the forward operator is the calculation of extinction coefficient $\alpha_\lambda(z)$ and backscatter coefficient $\beta_\lambda(z)$ based on a given atmospheric state and, finally, to determine the attenuated backscatter coefficient $\gamma_\lambda(z)$.

2.2 SCATTERING OF LASER RADIATION BY ARBITRARY OBJECTS

The total extinction coefficient $\alpha_\lambda(z)$ and the total backscatter coefficient $\beta_\lambda(z)$ of an illuminated volume with q_s different types of scatterers are calculated by

$$\alpha_\lambda(z) = \sum_{i=1}^{q_s} \alpha_{i,\lambda}(z) = \sum_{i=1}^{q_s} \int_0^\infty n_i(R, z) \, \sigma_{ext,i,\lambda}(R) \, dR, \tag{2.3}$$

$$\beta_\lambda(z) = \sum_{i=1}^{q_s} \beta_{i,\lambda}(z) = \sum_{i=1}^{q_s} \int_0^\infty n_i(R, z) \left(\frac{d\sigma_{sca,i,\lambda}(R)}{d\Omega}\right)_\pi \, dR, \tag{2.4}$$

where $n_i(R, z)$ is the number-size distribution of scatterer type i at range z given in units of m^{-3}, $\sigma_{ext,i,\lambda}$ is the extinction cross-section of scatterer type i given in units of m^2 with radius R, and $\left(\frac{d\sigma_{sca,i,\lambda}}{d\Omega}\right)_\pi$ is the differential backscatter cross section given in units of $m^2 \, sr^{-1}$.

For isotropic scattering, the differential backscatter cross section is derived from the scattering cross-section $\sigma_{sca,i,\lambda}(R)$ via

$$\left(\frac{d\sigma_{sca,i,\lambda}(R)}{d\Omega}\right)_\pi = \frac{\sigma_{sca,i,\lambda}(R)}{4\pi \, sr}. \tag{2.5}$$

For non-isotropic scattering, a phase function $\phi_{i,\lambda}(\theta, R)$ is used to describe the relative scattering intensity into angle θ which is π for monostatic systems:

$$\left(\frac{d\sigma_{sca,i,\lambda}(R)}{d\Omega}\right)_\pi = \frac{\sigma_{sca,i,\lambda}(R)}{4\pi \text{ sr}} \, \phi_{i,\lambda}(\pi, R). \tag{2.6}$$

Molecule scattering and particle scattering are differentiated here, as the respective calculations depend on suitable physical theories and algorithms.

2.3 SCATTERING BY MOLECULES

For a model which is capable to distinguish atmospheric gases such as nitrogen, oxygen, argon, and water vapor, the molecule scattering calculation could be performed for each individual gas type and molecule size using the Rayleigh theory (Young, 1981). For ACL systems, provided that a wavelength is used, which is well outside of molecular absorption lines, the individual gas contribution to the signal does not need to be distinguished.

Consequently, the molecule extinction coefficient $\alpha_{mol,\lambda}(z)$ and the molecule backscatter coefficient $\beta_{mol,\lambda}(z)$ can be calculated with

$$\alpha_{mol,\lambda}(z) = N_{mol,\lambda}(z) \, \sigma_{sca,mol,\lambda}, \tag{2.7}$$

$$\beta_{mol,\lambda}(z) = N_{mol,\lambda}(z) \left(\frac{d\sigma_{sca,mol,\lambda}}{d\Omega}\right)_\pi, \tag{2.8}$$

where the molecule number density $N_{mol}(z)$ is related to the ideal gas law

$$N_{mol}(z) = \frac{p(z)}{k \, T(z)}, \tag{2.9}$$

with p as atmospheric pressure given in Pascal (Pa), T as temperature given in Kelvin (K), and k as Boltzmann constant which has a value of 1.381×10^{-23} J K^{-1}.

To calculate the scattering cross-section $\sigma_{mol,\lambda}$ and the scattering phase function $\phi_{i,\lambda}(\pi)$ of air, the formulas given by Buchholtz (1995) were used. He suggests

$$\sigma_{mol,\lambda} = \frac{20 \, \pi^3 (n_{a,\lambda}^2 - 1)^2}{\lambda^4 \, N_{a,\lambda}^2 \, (n_s^2 + 2)^2} \frac{6 + 3p_{n,\lambda}}{6 - 7p_{n,\lambda}}, \tag{2.10}$$

where the wavelength λ is given in units of μm, $n_{a,\lambda}$ is the refractive index of air and $p_{n,\lambda}$ is the depolarization factor. For air, the molecule number density of $N_{a,\lambda}$

is $2.547\,43 \times 10^{19}\,\text{cm}^{-3}$. For the depolarization factor $p_{n,\lambda}$ the given look-up table is ranging from 4.545 ($\lambda = 200\,\text{nm}$) to 2.730 ($\lambda = 1000\,\text{nm}$). Due to this limitation of the look-up table, the depolarization factor for the ACLs wavelength in the case study (1064 nm) was simply extrapolated.

The index of refraction for $\lambda > 230\,\text{nm}$ can be calculated with

$$(n_{a,\lambda} - 1) \cdot 10^8 = \frac{5791817}{238.0185 - \left(\frac{-m}{\lambda}\right)^2} + \frac{167909}{57.362 - \left(\frac{-m}{\lambda}\right)^2}, \tag{2.11}$$

where the wavelength λ is given again in units of micrometers.
Furthermore, the Rayleigh phase function $\phi_{a,\lambda}(\pi)(\theta)$ is

$$\phi_{a,\lambda}(\psi) = \frac{3}{4(1 + 2\psi_{a,\lambda})} \left((1 + 3\psi_{a,\lambda}) + (1 - \psi_{a,\lambda})\cos^2\theta\right), \tag{2.12}$$

with θ as scattering angle and $\psi_{a,\lambda}$ defined as

$$\psi_{a,\lambda} = \frac{p_{a,\lambda}}{2 - p_{a,\lambda}}. \tag{2.13}$$

Using these empirical equations and look-up tables, the scattering properties of air molecules $\sigma_{mol,\lambda}$ and $\left(\frac{d\sigma_{mol,i,\lambda}}{d\Omega}\right)_\pi$ can be determined by only knowing the ACL laser wavelength λ.

2.4 SCATTERING BY PARTICLES

The scattering characteristics of larger particles are described by Mie's solution of the Maxwell equations (Mie, 1908; Wiscombe, 1980). The T-matrix method (Mishchenko, Travis, and Lacis, 2002) or the Discrete Dipole Approximation (DDA, Draine and Flatau (1994)) allow for calculating the scattering properties of non-spherical objects with sizes not much smaller or larger than the wavelength. T-matrix is a tool for computing scattering by single and compounded particles (Mishchenko, Travis, and Lacis, 2002). It is faster than Discrete Dipole Approximation (DDA) but limited to rotationally-symmetric objects such as ellipsoids, cylinders, or Chebyshev polynomials. DDA, however, has the flexibility to represent arbitrarily shaped objects at the cost of high computational efforts.

As a rough estimate, the computational time increases by about one order of magnitude when using T-matrix instead of Mie scattering calculation routines and by another two orders of magnitude when using DDA instead of T-matrix. Another increase in computational time is resulting from larger scatterers, i. e., an increase of the particle size results in an exponential increase of computing time. In this study, Mie scattering

algorithms are therefore used to perform fast calculations. The effect of scattering by non-spherical particles is analyzed in a second step by T-matrix scattering calculations for several non-spherical particle shapes in the frame of sensitivity studies. This approach is required because the COSMO-ART volcanic ash dispersion simulation does not output any information about the particle shape distribution.

Mie scattering-related computations were performed using the Interactive Data Language (IDL) procedure called "mie_single", provided by the Department of Atmospheric, Oceanic and Planetary Physics (AOPP), University of Oxford. Input parameters of the procedure are the real part m and imaginary part m' of the refractive index as well as the so-called size parameter $X_\lambda(R)$:

$$X_\lambda(R) = \frac{2\pi R}{\lambda},$$
(2.14)

where R is the radius of a single particle. The relevant output parameters are the extinction efficiency $Q_{ext,p,\lambda}(R)$, the scattering efficiency $Q_{sca,p,\lambda}(R)$, and the backscatter efficiency $Q_{bsc,p,\lambda}(R)$. These optical efficiencies are defined as ratio between the optical cross section and the physical cross section:

$$Q_{ext,p,\lambda}(R) = \frac{\sigma_{ext,p,\lambda}(R)}{\pi R^2},$$
(2.15)

$$Q_{sca,p,\lambda}(R) = \frac{\sigma_{sca,p,\lambda}(R)}{\pi R^2},$$
(2.16)

$$Q_{bsc,p,\lambda}(R) = \frac{\left(\frac{d\sigma_{sca,p,\lambda}(R)}{d\Omega}\right)_\pi}{\pi R^2}.$$
(2.17)

In the following, the symbol $\sigma_{bsc,p,\lambda}$ is used for the differential backscatter coefficient. $\sigma_{bsc,p,\lambda}$ looks similar to the extinction and scattering cross section but is given in units of $m^2\, sr^{-1}$ while $\sigma_{ext,p,\lambda}(R)$ and $\sigma_{sca,p,\lambda}(R)$ are in units of m^2. Consequently, the optical cross sections are calculated from:

$$\sigma_{ext,p,\lambda}(R) = Q_{ext,p,\lambda}(R)\pi R^2,$$
(2.18)

$$\sigma_{sca,p,\lambda}(R) = Q_{sca,p,\lambda}(R)\pi R^2,$$
(2.19)

$$\sigma_{bsc,p,\lambda}(R) = Q_{bsc,p,\lambda}(R)\pi R^2.$$
(2.20)

The scattering cross section is a representative for the overall scattering intensity of light by a single scatterer. The extinction cross section is a description for the signal weakening due to scattering and absorption by the scatterer and the backscatter cross section describes the scattering intensity of light into backwards direction. While air molecules were assumed to be non-absorbing, the signal weakening by aerosols depends on both their scattering as well as their absorption properties. Regarding the optical efficiencies Q_{ext}, Q_{sca}, and Q_{bsc}, these are the normalized optical cross sections by their physical cross section which is an expression for the relative change of the scattering properties depending on the relative change of the scatterer size. While for example the extinction cross section increases exponentially due to its dependency on R^2, the extinction efficiency is independent of this size relationship.

It should be mentioned that the definition of the backscatter efficiency changed between two releases of procedure mie_single: The current (2012) release of mie_single returns the so-called radar backscatter efficiency which is 4π times the backscatter efficiency as required within the forward operator. Furthermore, the procedure expects the imaginary part of the refractive index given as negative number. If positive imaginary part values are used, the procedure runs without showing an error but returns wrong values.

2.5 REPRESENTATION OF DISCRETE AEROSOL NUMBER-SIZE DISTRIBUTIONS

A major problem of discrete size distributions is the high sensitivity of the optical cross sections to the particle size: A slightly different particle radius may lead to quite a large change of the scattering properties. Due to the fact that naturally occurring particle size distributions are not discrete, averaging the optical cross sections over certain size-intervals seems straightforward. This approach indeed reduces the problematic and unrealistic sensitivity significantly (see Chapter 4). If the model represents only one type of particle, i. e. with a constant refractive index but with variable radius R_d, the effective extinction cross section and the effective backscatter cross sections can be defined as

$$\overline{\sigma_{ext,R_d,m,m',\lambda}} = \frac{1}{R_{d_b} - R_{d_a}} \int_{R_{d_a}}^{R_{d_b}} Q_{ext}(X_\lambda(R_d), m, m') \, \pi R_d^2 \, dR_d, \tag{2.21}$$

$$\overline{\sigma_{bsc,R_d,m,m',\lambda}} = \frac{1}{R_{d_b} - R_{d_a}} \int_{R_{d_a}}^{R_{d_b}} Q_{bsc}(X_\lambda(R_d), m, m') \, \pi R_d^2 \, dR_d, \tag{2.22}$$

where R_{d_a} and R_{d_b} are size margins for each particle size class d. These integrals are then exchanged by sums in the numerical computation routines.

The calculation of the effective values is performed for every discrete size class d and - if represented by the model - also for every particle type k. Consequently, the

total particle extinction coefficient $\alpha_{\text{par},\lambda}(z)$ and the total particle backscatter coefficient $\beta_{\text{par},\lambda}(z)$ are calculated from:

$$\alpha_{\text{par},\lambda}(z) = \sum_k \sum_d N_{d,k}(z)\, \overline{\sigma_{\text{ext},R_d,m_k,m'_k,\lambda}}, \tag{2.23}$$

$$\beta_{\text{par},\lambda}(z) = \sum_k \sum_d N_{d,k}(z)\, \overline{\sigma_{\text{bsc},R_d,m_k,m'_k,\lambda}}. \tag{2.24}$$

Here, $N_{d,k}$ is the particle number per volume given by the model, $\overline{\sigma_{\text{ext},R_d,m_k,m'_k,\lambda}}$ and $\overline{\sigma_{\text{bsc},R_d,m_k,m'_k,\lambda}}$ are the effective optical cross sections of particle size class d and particle type class k with the respective real part m_k and imaginary part m'_k of the refractive index.

This simple solution allows for the calculation of $\alpha_{\text{par},\lambda}(z)$ and $\beta_{\text{par},\lambda}(z)$ by just solving few multiplications and summations resulting in a minimal demand of computing time.

2.6 CALCULATION OF TOTAL EXTINCTION AND TOTAL BACKSCATTER COEFFICIENT

The forward modeled total extinction coefficient and total backscatter coefficient are the sum of the molecule and the particle extinction and backscatter coefficients:

$$\alpha_\lambda(z) = \alpha_{\text{mol},\lambda}(z) + \alpha_{\text{par},\lambda}(z), \tag{2.25}$$

$$\beta_\lambda(z) = \beta_{\text{mol},\lambda}(z) + \beta_{\text{par},\lambda}(z), \tag{2.26}$$

equivalent to Eq. (2.3) and (2.4).

2.7 CALCULATION OF THE TWO-WAY TRANSMISSION INTEGRAL

The two-way transmission T_λ is calculated by

$$T_\lambda(z) = \exp\left(-2 \int_0^z \alpha_\lambda(z')\, dz'\right). \tag{2.27}$$

Thus, T_λ at height z depends on the extinction of transmitted signals on the travel from instrument $z = 0$ to height z, both on the forward and returning path. Within

the forward operator, the two-way transmission is discretized into the models' vertical layers by height increment and vertical resolution:

$$T_\lambda(z) = \exp\left(-2 \sum_{z=1}^{n_z(z)} \alpha_\lambda(z)\,\Delta h(z)\right), \tag{2.28}$$

where the number of height levels between ground and actual height is expressed by $n_z(z)$, the vertical profile of the extinction coefficient is $\alpha_\lambda(z)$ and the vertical profile of the layer thickness is $\Delta h(z)$. In the case of forward modeling a vertically-pointing measurement, the vertical column of model grid margins at a specific location is required. By applying the laws of geometry, the forward operator is potentially able to simulate scanning measurements.

2.8 DEFINITION OF THE LIDAR RATIO AND THE PURE LIDAR RATIO

Even though the lidar ratio is not measured directly by current ACL systems, the capability of simulating the lidar ratio for given scatterer types and scatterer mixtures offers a great potential for sensitivity studies but also for comparison to research lidar systems such as Raman lidar. The forward modeled total lidar ratio $S_{lidar}(z)$ can be calculated from

$$S_{lidar,\lambda}(z) = \frac{\alpha_{par,\lambda}(z)}{\beta_{par,\lambda}(z)}, \tag{2.29}$$

where $\alpha_{par,\lambda}(z)$ and $\beta_{par,\lambda}(z)$ are the total particle extinction and backscatter coefficients given by Eq. (2.23) and Eq. (2.24), respectively. It depends not only on the assumed particle type and shape, but also on the particle size class configuration of the model, i.e. size class number, size class range and particle size coverage. The forward modeled lidar ratio thus becomes more representative with a wider particle size spectrum as well as more particle size, type and shape classes output by the dispersion model.

To analyze the lidar ratio sensitivity independent of a models' particle size class and type class configuration, the pure lidar ratio $S_{lidar,pure}$ was introduced here. In a molecule-free volume with monodisperse particles, the particle number per volume $N_{R,p}$ is a factor with R as particle radius, giving

$$S_{lidar,pure,R,p,\lambda} = \frac{\sigma_{ext,R,p,\lambda}}{\sigma_{bsc,R,p,\lambda}}. \tag{2.30}$$

The pure lidar ratio $S_{lidar,pure,R,p,\lambda}$ allows for performing sensitivity studies to analyze influences of the particle shape on the expected lidar ratio values (which will be shown later in Chapter 4).

Conclusively, this implementation of a backscatter lidar forward operator allows for an efficient calculation of ACL profiles based on the output of atmospheric chemistry models. The biggest challenge for setting up the forward operator in a given scenario are scattering calculations, namely the calculation of the effective extinction cross section $\overline{\sigma_{\text{ext},R_d,m_k,m_k',\lambda}}$ and the effective differential backscatter cross section $\overline{\sigma_{\text{bsc},R_d,m_k,m_k',\lambda}}$ of all represented aerosol classes and types. Due to its importance, a complete section is dedicated to sensitivity studies of the optical cross sections regarding the particle size, refractive index and shape (Chapter 4). This section will follow the introduction to the case study for which the forward operator was applied and compared to ACL measurements.

3 CASE STUDY: VOLCANIC ASH EVENT DURING THE EYJAFJALLAJÖKULL (ICELAND) ERUPTION IN 2010

3.1 INTRODUCTION TO THE CASE STUDY

In spring 2010, an eruption of the volcano Eyjafjallajökull in Iceland (see Fig. 3.1) lead to a closure of the European air space for several days (Sandrini et al., 2014). This event was extensively analyzed by scientists from many fields of research, resulting in a substantial knowledge base (see Atmospheric Chemistry and Physics Journal (ACP) special issue *Atmospheric implications of the volcanic eruptions of Eyjafjallajökull, Iceland 2010*). Ash layers were observed from a large set of measurement instruments, allowing for tracking the volcanic ash plume over Europe (Gasteiger et al., 2011a; Zakšek et al., 2013; Mona et al., 2012; Dacre, Grant, and Johnson, 2013; Waquet et al., 2014). Using images from the geostationary Spinning Enhanced Visible and Infrared Imager (SEVIRI), the spatial extent of the ash plumes and their movements could be tracked and compared to the measurement of ground-based instruments (Strohbach (2015), see Fig. 3.1). From the synergy of the two measurement systems, layers with strong backscattering could be related to clouds or volcanic ash layers, respectively.

Such a volcanic eruption case has a well-known aerosol source location which renders the Eyjafjallajökull eruption an important case study for aerosol dispersion simulation models and respective validation methods (Matthias et al., 2012).

3.2 DESCRIPTION OF THE DWD CEILOMETER NETWORK

ACL networks are a valuable data source for analyzing the vertical structure of aerosols. A qualitative analysis of the Eyjafjallajökull ash plume over Germany using observations from 36 ACL systems CHM15k manufactured by Jenoptik now Lufft was made by Flentje et al. (2010b). These ACL systems operate at a wavelength of 1064 nm. Other device-specific properties are listed in Table 3.1. A qualitative analysis of the ash plume over Germany with this data set was made by (Flentje et al., 2010b).

From an analysis of the ACL measurements between 14 April 2010 and 16 April 2010, only 6 stations have been identified where the volcanic ash plume is visible without being tainted by other clouds or hidden by near-ground fog layers (Strohbach, 2015). In contrast to precipitation radars, full-range vision is not guaranteed for lidar systems and important features may not be observable depending on the atmospheric condition. This indicates the demand for lidar networks in terms of lidar data assimilation. Accessing data of only few high-performance lidar systems such as Raman

Figure 3.1: Eyjafjalla ash plume satellite image recorded by the MODIS instrument mounted at NASA's Aqua satellite during the 17 April 2010. Source: http://earthobservatory.nasa.gov.
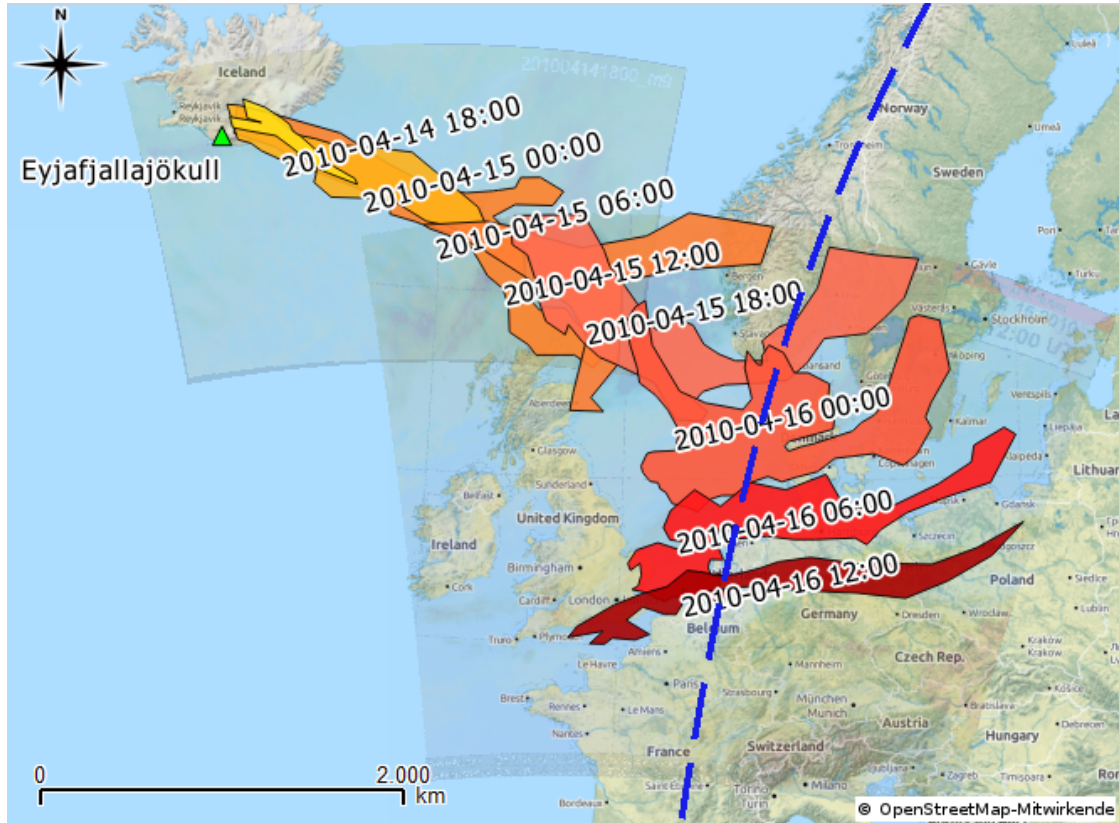
Figure 3.2: Distribution and transport of volcanic ash over northwest Europe sketched using georeferenced satellite images (Meteosat-9, Dust). After georeferencing, the ash layers were retraced as colored polygons, where the color of the polygons (yellow to red) represent consecutive time steps (Strohbach, 2015). The blue dashed line indicates the flight track of CALIPSO during 17 April 2010 (measurement shown in Fig. 3.5)

Table 3.1: Assumed lidar constants of the CHM15k ceilometers taken or derived from the manufacturer's data sheet http://www.lufft.com/

Name	Symbol	Value
Energy per pulse	E_{p_0}	$8\,\mu J$
Pulse repetition frequency	f_{rep}	$5\,kHz$
Vertical resolution	Δh	$15\,m$
Area of the receiving telescope	A_{tel}	$78.54\,cm^2$
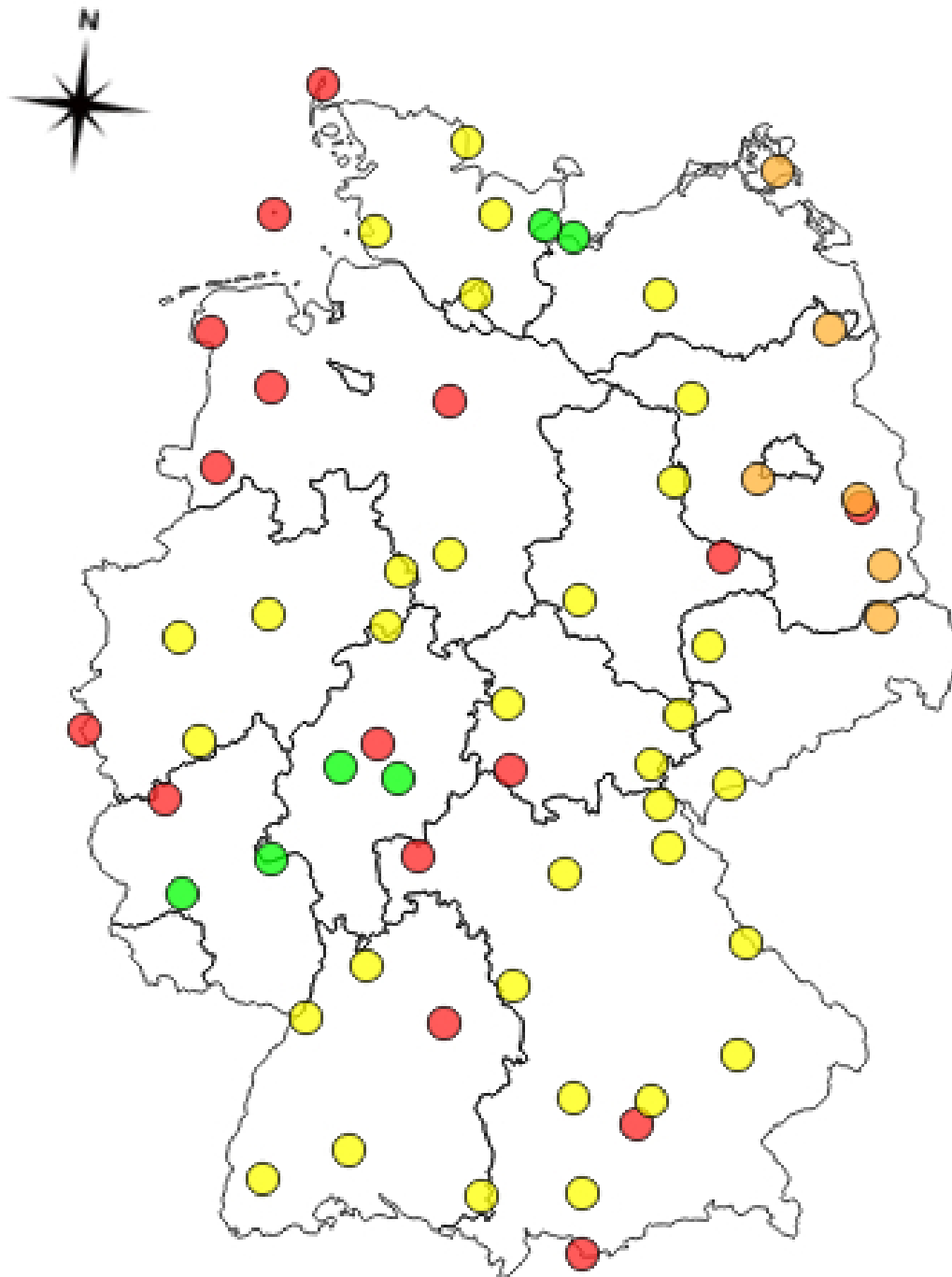
Geoinformation © Bundesamt für Kartographie und Geodäsie (www.bkg.bund.de)

Figure 3.3: The DWD Ceilometer Network in 2010. Each dot represents a ceilometer station. Green dots: stations which were fully operating during the Eyjafjallajökull eruption in 2010. Yellow dots: Stations deliver data but ash plume is not fully visible. Orange and red dots: Data not available or no ash layers visible. Taken from (Strohbach, 2015)

lidar or HSRL may lead to numerous situations where features in the atmosphere are not observable at all due to low-level fog or other clouds.

The Network Common Data Form (NetCDF) files with ACL raw data contain the 24 hour measurement of one ACL station. The received photon number per shot is calculated from

$$N_{rec}(z, t) = \text{beta\_raw}(z, t) \cdot \text{stddev}(t) + \text{base}(t), \tag{3.1}$$

where beta_raw are the offset corrected measurement profiles, normalized by the noise standard deviation stddev, and base is the daylight correction factor (negative value of received photon number from the last few range bins). A plot of the received photon number and the range-corrected received photon number is Fig. 3.4. ACL data in its original resolution show thin ash layers and their internal structure but noise is also strongly present and gets even amplified by applying the range correction.

The equation for calculating the attenuated backscatter coefficient from ACL measured photon counts per shot reads:

$$\gamma_\lambda^*(z) = \frac{N_{rec,\lambda}(z, t)\, z^2}{N_{tr,\lambda}\, \eta_\lambda\, A_{tel}\, O(z)\, \Delta z}. \tag{3.2}$$

The pulse energy of the diode-pumped laser is $8\,\mu J$ (Flentje et al., 2010a), resulting in an emitted photon number per pulse of about 4.28×10^{13}. The diameter of the receiving telescope is $100\,mm$ (Flentje et al., 2010a) which results in $A_{tel} = 78.54\,cm^2$. The vertical resolution Δz is $15\,m$ for the complete profile. The overlap function $O(z)$ was set to 1 which implies that ranges below about $1500\,m$ cannot be used reliably for comparisons with the forward operator.

Unfortunately, the instruments provided no calibrated measurement data at that time, so a linear calibration factor η^* is used as replacement for the system efficiency η_λ. From a comparison with calibrated attenuated backscatter measurements of CALIOP at $\lambda = 1064\,nm$ (Fig. 3.5), a calibration factor of $\eta^* = 0.003$ could be determined: Therefore, the CALIOP value of the $1064\,nm$ calibrated attenuated backscatter coefficient was used at $50.15°$ lat / $4.81°$ lon in a height of $2\,km$. As a validation step, the resulting attenuated backscatter coefficient values were compared to Raman lidar measurements of the volcanic ash plume at Munich and Leipzig (Ansmann et al., 2010). The maximum Raman lidar measured backscatter coefficient at $\lambda = 1064\,nm$ was $8 \times 10^{-6}\,m^{-1}\,sr^{-1}$ for both Munich and Leipzig and the maximum calculated attenuated backscatter coefficient of the ACL measurement at Deuselbach after calibration is in the same order of magnitude. As most present ACL networks have been extended by automatic calibration capabilities, such pragmatic calibration approaches will not be required in future forward operator studies. It should be noted that not
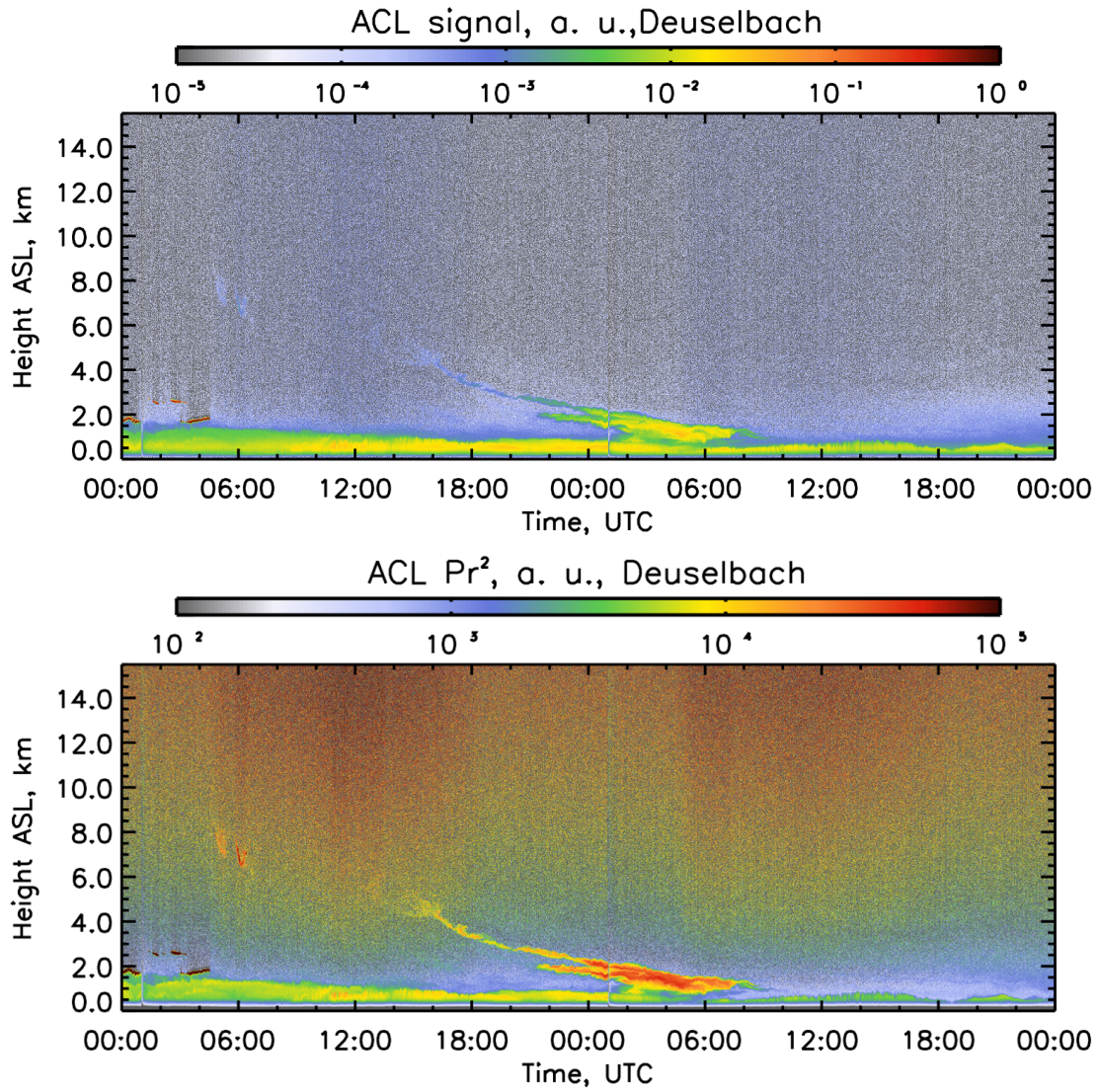
Figure 3.4: 48 h time-height cross section of ACL measurement at the station Deuselbach in West-Germany from 16 April 2010, 00:00 UTC, to 17 April 2010, 23:59 UTC. Top: ACL signal calculated using Eq.(3.1); Bottom: The same data after range-correction.
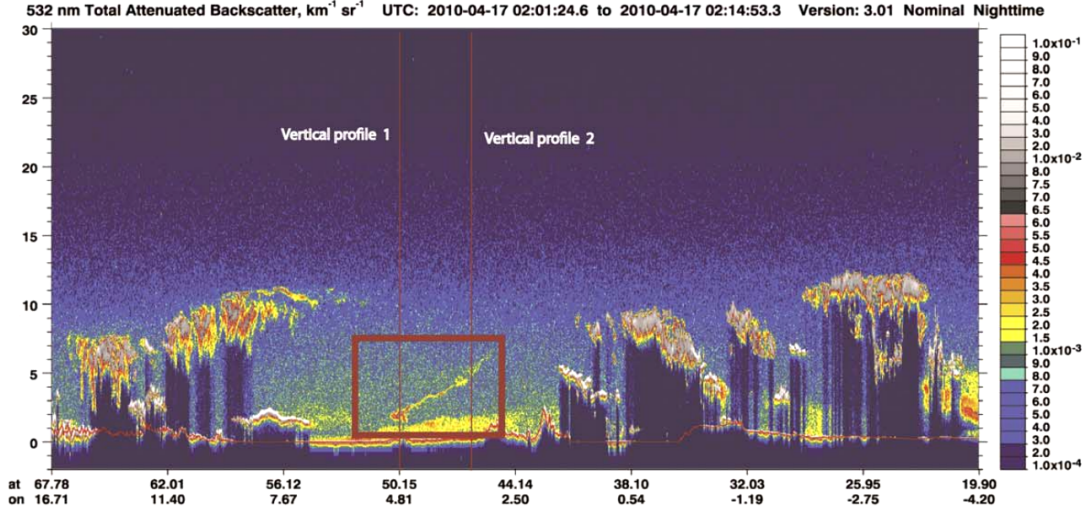
Figure 3.5: Attenuated backscatter coefficient measurement taken by the CALIOP instrument which was used to calibrate ACL measurement during the Eyjafjallajökull eruption phase. The volcanic ash plume is visible around 50.15° lat and 4.81° lon. As the instrument measures from space, the attenuated backscatter coefficient inside the ash plume is not affected by attenuation due to aerosols in the planetary boundary layer. Source: http://www-calipso.larc.nasa.gov/

only the absolute calibration is important. Even if the calibration is not perfect, a comparison of lidar and model data permits a thorough comparison of vertical structures such as the thickness and heights of aerosol layers.

The high-resolution ACL data furthermore had to be gridded to the model's temporal and vertical resolution for quantitative comparisons between forward modeled atmospheric simulations and ACL data. This gridding improves the signal-to-noise ratio which is proportional to the averaging sample number $N_{samples}$:

$$ \text{SNR} \propto \frac{N_{samples}}{\sqrt{N_{samples}}} = \sqrt{N_{samples}}. \tag{3.3} $$

If the ACL data has a vertical resolution of 15 m and a temporal resolution of 15 s, averaging over a 15 min time and 200 m height interval increases the Signal-To-Noise-Ratio (SNR) by:

$$ \sqrt{\frac{200\,\text{m}}{15\,\text{m}}\frac{1800\,\text{s}}{15\,\text{s}}} = 40. \tag{3.4} $$

Due to the variable layer thickness of COSMO-ART, this SNR improvement ranges from a factor of 10.9 at the bottom levels and to a factor of 126 at the highest levels - assuming a temporal resolution of 15 min.

3.3 SET-UP OF COSMO-ART FOR THE EYJAFJALLAJÖKULL ASH TRANSPORT SIM-ULATION

COSMO-ART was set up by DWD in collaboration with Karlsruhe Institute of Technology (KIT) for an ash-dispersion simulation of the volcanic emissions during the eruptive phase of Eyjafjallajökull in Spring 2010 (Vogel et al., 2014). The model domain was configured to a horizontal grid size of 7 km and 40 height layers. The height layer thickness was variable, ranging from several meters near ground to a layer thickness of about 3 km in 22 km height above ground. A more general description of the model run is given by Vogel et al. (2014).

For this study, the 78-hour forecast was used, beginning at 15 April 2010, 00:00 UTC, which includes volcanic ash emission data since 14 April 2010, 06:00 UTC. Volcanic ash was represented by six discrete size classes with aerodynamic diameters of 1 μm, 3 μm, 5 μm, 10 μm, 15 μm and 30 μm. For each class, a number concentration was predicted by the model. Particles within a class were treated as being identical, i. e., having the same size, shape, and complex index of refraction (monodisperse distribution), so the calculation of effective optical cross sections follows Section 2.5. The lower and upper size margins R_{d_a} and R_{d_b} were defined as arithmetic averages of two subsequent size classes. The lower margin of the smallest size class was half its nominal diameter; the upper margin of the largest size class was 1.5 times its nominal diameter. The resulting class ranges are shown in Fig. 3.6. A list of model variables used for the forward operator is given by Table 3.2.

A list of model variables used for the forward operator is Table 3.2. While the aerosol number density is taken directly from model output, the molecule number density of standard air was calculated from temperature and pressure according to equation (2.9).

The model output data was available as American Standard Code for Information Interchange (ASCII) text fragments which had to be collected, sorted and stored as NetCDF binary data. As the complete prediction time interval is available in such post-processing studies, the forward operator applied on the full time series of vertical profiles which results in a time-height cross section similar to the ACL measurements. As a consequence, the time-height cross sections of both ACL and COSMO-ART with an applied forward operator contain no spatial information of an objects except the vertical extend.

3.4 PHYSICAL PROPERTIES OF EYJAFJALLAJÖKULL ASH PARTICLES

A detailed analysis of the emitted ash was performed by Schumann et al. (2011) who compared measurements from Falcon 20 aircraft of the German Aerospace Center (DLR) with data of research lidar systems in Germany. Eyjafjallajökull ash samples were taken in-situ, analyzed using a scanning electron microscope, and assigned to
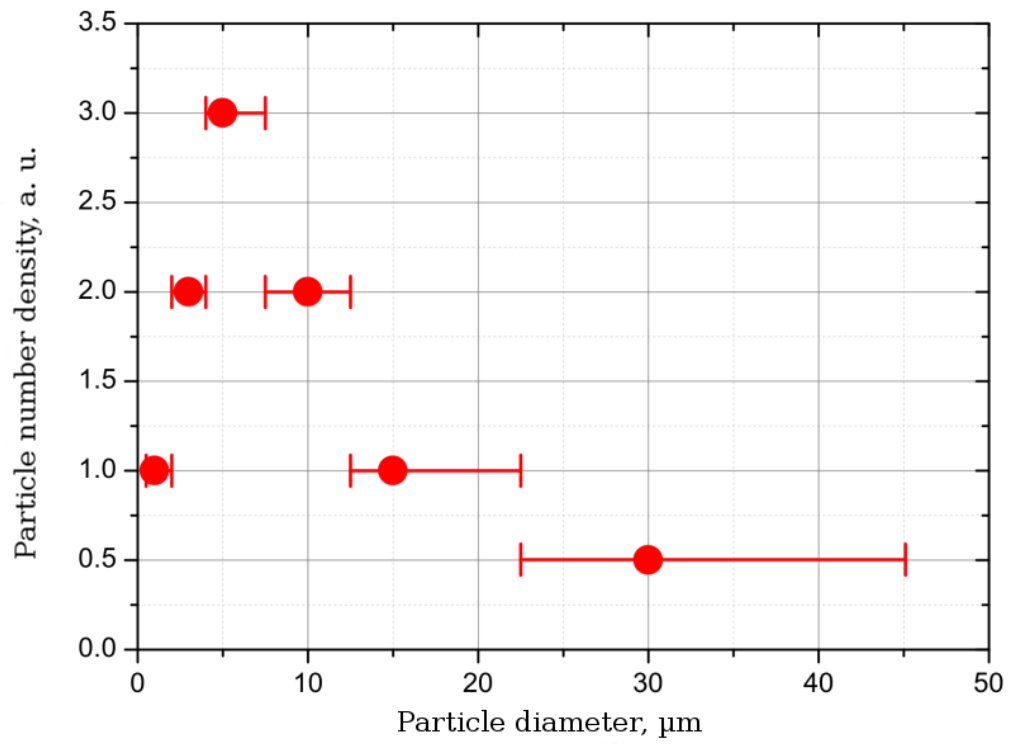
Figure 3.6: Sketch of the particle size distribution represented by COSMO-ART for the Eyjafjalla-
jökull dispersion simulation (red dots). The red lines with bars indicate the averag-
ing margins that were defined for the calculation of effective optical cross sections.

Table 3.2: Model output variables of COSMO-ART used by the forward operator for the selected case study.

Variable	Symbol	Description	Unit
ASH1	N_1	Ash number density of class 1 (1 µm)	m^{-3}
ASH2	N_2	Ash number density of class 2 (3 µm)	m^{-3}
ASH3	N_3	Ash number density of class 3 (5 µm)	m^{-3}
ASH4	N_4	Ash number density of class 4 (10 µm)	m^{-3}
ASH5	N_5	Ash number density of class 5 (15 µm)	m^{-3}
ASH6	N_6	Ash number density of class 6 (30 µm)	m^{-3}
Pmain	p	Atmospheric pressure	hPa
T	T	Atmospheric temperature	°C

matter groups. From the matter components, the complex index of refraction was calculated.

According to Schumann et al. (2011), the real part of the refractive index was between 1.53 and 1.60 at a wavelength of $\lambda = 630\,nm$ and between 1.50 and 1.56 at a wavelength of $\lambda = 2000\,nm$. The respective imaginary part was ranging from $-0.001\,i$ to $-0.004\,i$ at a wavelength of $\lambda = 630\,nm$ and from $-2.0 \times 10^{-6}\,i$ to $-40.0 \times 10^{-6}\,i$ at a wavelength of $\lambda = 2000\,nm$.

Electron microscope images from the same study revealed that the volcanic ash particles were sharp-edged with a complex and asymmetric shape, see Fig. 3.7. The average asymmetry factor was 1.8 for small particles ($<0.5\,\mu m$) and 2.0 of larger particles (Schumann et al., 2011). Electron microscope measurements of Rocha-Lima et al. (2014) showed that the asymmetry factor of the volcanic ash fine fraction was between 1.2 and 1.8.

The particle growth due to hygroscopic water coating was quantified to about 2 to 5 % at a relative humidity of 90 % (Lathem et al., 2011). A growth of 5 % does not change the scattering properties significantly in relation to the size averaging which is performed for monodisperse size classes in the forward operator. But even perfectly known volcanic ash particles will change their constitution while traveling through the atmosphere. It is therefore essential to analyze the maximum uncertainty for applying the forward operator on volcanic ash particles with variable properties, namely the particle size, refractive index, and shape.
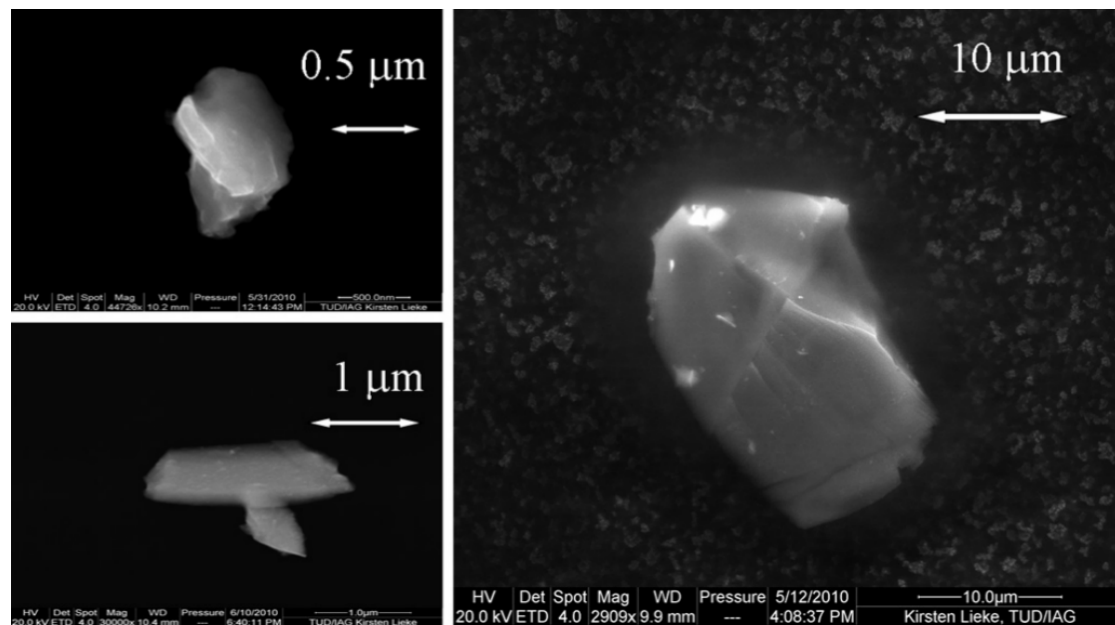
Figure 3.7: Microscope image of an Eyjafjallajökull ash particle taken by (Schumann et al., 2011). Ash particles are sharp edged and irregularly shaped which render a classification of particle shapes impractical.

4 SENSITIVITY STUDIES OF THE FORWARD OPERATORS' INPUT PARAMETERS

The representation of the particles by the model is clearly simplified, so the effect of these simplifications on the scattering of laser light must be determined when applying the forward operator. For a lidar forward model, sensitivities of the backscatter cross section are critical because the received signal intensity is linearly coupled to the backscatter cross section and, consequently, to the attenuated backscatter coefficient.

Prior studies already showed the complexity of non-spherical scattering calculations but there is no universal solution for the problem available. Gasteiger et al. (2011b) use DDA to calculate the scattering properties of complex shaped particles but the analysis was limited to size-parameters up to 20.8 due to the increasing computational time per iteration for increasing particle sizes. The equivalent radius of this size parameter at a wavelength of 1064 nm would be 3.5 µm. The computation of a high-resolution multi-dimensional Look-Up Table (LUT) for up to 10 times larger particles would require an unfeasible long time. The study of Kemppinen et al. (2015) focused on individual ellipsoids but assuming an ellipsoidal distribution to represent fractional and sharp edged particles may lead to less realistic scattering calculation results than assuming spherical scatterers. Consequently, there is no scattering description for Eyjafjallajökull ash predictions of COSMO-ART available. It is important to treat the volcanic ash as spherical objects with given optical properties (see 3.4) but analyze and discuss the effect of variable volcanic ash properties in the following.

It must be noted that these studies are required for most aerosol types as most naturally-occurring aerosols are not perfectly spherical and even slightly non spherical ellipsoids may have very different scattering characteristics compared to ideal spheres.

4.1 PREREQUISITES FOR THE SENSITIVITY STUDIES

Look-Up Tables of Mie efficiencies and optical cross sections have been created to reduce the effort on time-consuming scattering calculations. The look up tables have three dimensions: size parameter $X_\lambda(R_p)$, real part of the refractive index m and imaginary part of the refractive index m'.

The reasonable range of size parameters depends on the wavelength of the lidar transmitters and the radius of occurring particles R_p. For the ACL systems operating at $\lambda = 1064$ nm, the relevant size-parameter ranges from 1.2 ($R_p = 0.2$ µm) to 142.9 ($R = 24.2$ µm); see Eq. (2.14).

As explained in section 3.4, the refractive index measurements by Schumann et al. (2011) were not performed for the exact wavelength of the ACL systems. Therefore, the reference refractive index and the interval of uncertainty had to be estimated. Schumann et al. (2011) take a refractive index of 1.59 - 0.004i for their medium "M" case study and therefore this value is also used as reference for the sensitivity study. The uncertainty intervals of real and imaginary parts were chosen according to the range of measured values at 630 nm and 2000 nm, namely a real part range of 1.54 to 1.64 and an imaginary part range of -0.006 to -0.002. To get an estimate of the overall refractive index sensitivity for such particles, the range of analyzed refractive indices was extended to real parts between 1.49 and 1.69 using increments of 0.001 and to imaginary parts between -0.011 and -0.001 using increments of 0.00005. Using a radius increment of $0.024\,\mu m$, the total element number of one LUT is 4.0×10^7 and these look-up tables were the base for the refractive index sensitivity study.

4.2 SENSITIVITY TO THE LASER WAVELENGTH

The CHM15-k devices are equipped with a diode-pumped Nd:YAG laser (Flentje et al., 2010b) and are temperature stabilized. For such devices, variations of the laser wavelength are expected to be within $\pm 1\,nm$. Instruments without such features may emit laser light with wavelength variations exceeding $\pm 10\,nm$. This affects the calculated size parameter X_λ significantly (see Eq. (2.14)) and therefore all subsequent scattering calculations. The sensitivity of the extinction efficiency and the backscatter efficiency for wavelength variations of $\pm 20\,nm$ are shown in Fig. 4.1. It becomes evident that even for such unrealistically high variations of the laser wavelength, the effect on the extinction and backscatter efficiency spectrum is negligible - especially in relation to the coarse monodisperse size classes used by the COSMO-ART within the case study.

4.3 SENSITIVITY TO THE COMPLEX INDEX OF REFRACTION

The extinction cross section σ_{ext}, backscatter cross section σ_{bsc}, effective extinction cross section $\overline{\sigma_{ext}}$, and effective backscatter cross section $\overline{\sigma_{bsc}}$ plotted over real and imaginary parts of the complex index of refraction are shown in Figures 4.2, 4.3, 4.4, 4.5, 4.6, 4.7, 4.8, 4.9, 4.10, 4.11, 4.12, and 4.13. While the extinction cross section σ_{ext} is more sensitive to the real part than to the imaginary part of the refractive index, the backscatter cross section σ_{bsc} is strongly sensitive to both. These sensitivities are reduced for the effective extinction cross section $\overline{\sigma_{ext}}$ and the effective backscatter cross section $\overline{\sigma_{bsc}}$. Using effective cross sections includes the averaging over a wider range of particle sizes which sometimes yields in generally higher values. For example the effective extinction cross section of particle class 6 ($15\,\mu m$ in radius) is always higher than the extinction cross section without averaging. This is due to the wide range of particle radii which are covered by this size class (a factor of 1.5 times the referenced particle
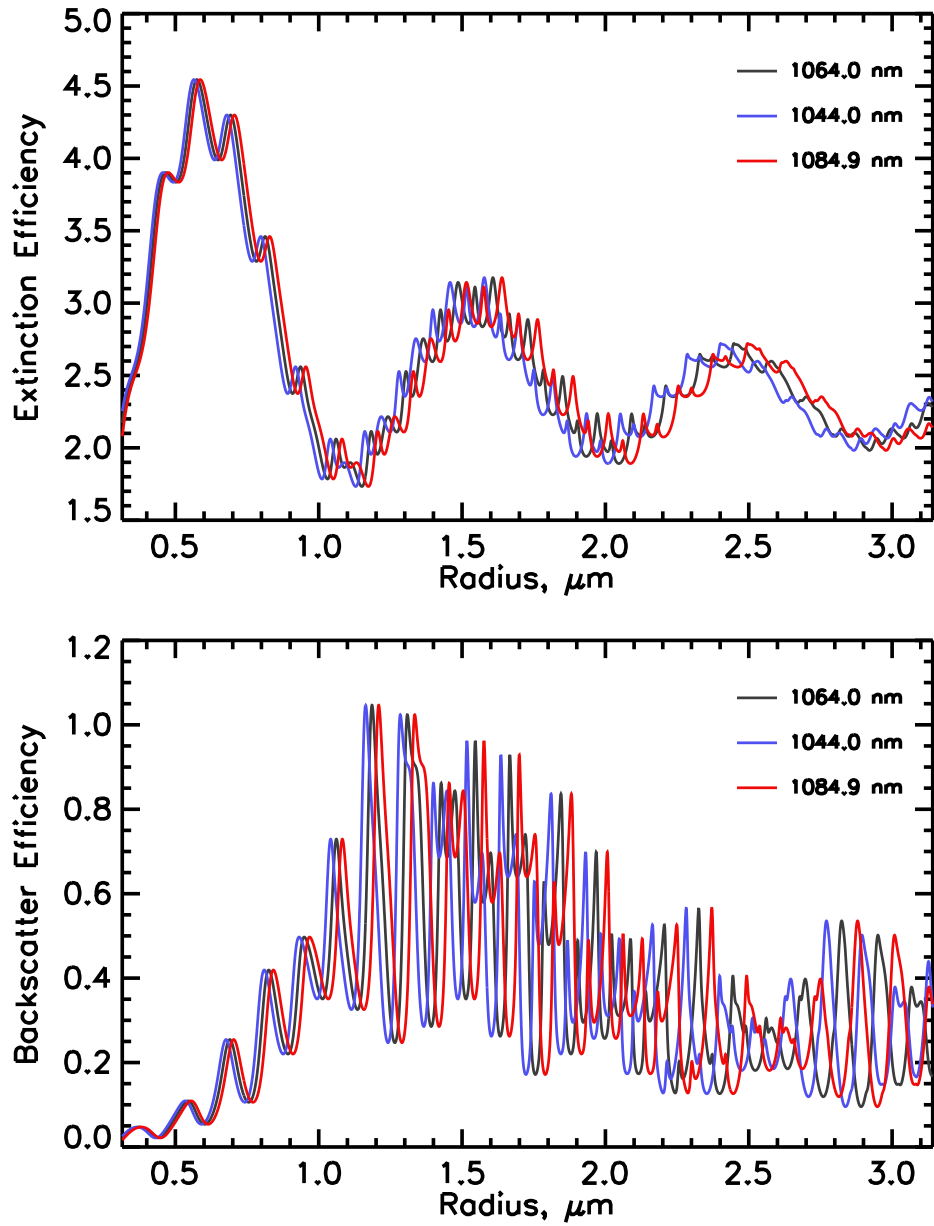
Figure 4.1: Extinction efficiency spectrum (top) and backscatter efficiency spectrum (bottom) for variable wavelengths and a fixed complex index of refraction, namely 1.59-0.004i. The wavelength variations namely are: 1064 nm (black line), 1044 nm (blue line), and 1084 nm (red line).

size). The particle size effect is especially pronounced for the extinction as within the analyzed range of size parameters, the extinction cross section is exponentially proportional to the particle radius. On the one hand, this effect may be reduced by selecting symmetric particle size boundaries for the averaging interval, i. e. $\pm 5\,\mu m$ for the $15\,\mu m$ size class. On the other hand, this attempt could become problematic for certain size class definitions. Assuming a size class definition of $2\,\mu m$, $3\,\mu m$ and $9\,\mu m$, the averaging intervals cannot be symmetrically selected such that there are neither gaps between the size class definitions nor some classes are covered completely by the next larger one(s). It is therefore preferable to use the initial definition of the size class margins which guarantee a continuous coverage of particle sizes for the given range of particle size classes. In contrast to the extinction cross section, the backscatter cross section after averaging becomes less sensitive to the refractive index without being generally increased due to a wide averaging window. In the given range of size parameters, a proportionality to R^2 cannot be observed from these plots. A major issue for the backscatter cross section is its sensitivity at the far end of the given interval of real and imaginary parts of the refractive index. While the effective extinction cross section is non-sensitive to the refractive index, a high sensitivity can be observed for the effective backscatter cross section. For each size class in this study, the effective backscatter cross section reaches its maximum value at the highest real part and highest imaginary part which is considered for the Eyjafjallajökull ash. A further reduction of the effective backscatter cross section uncertainty can thus only be achieved by a smaller uncertainty interval of the complex index of refraction.

A measure for the refractive index sensitivity of the effective optical cross sections is given by Fig. 4.14 and 4.15 which shows the relative errors

$$\sigma_{\text{ext,err,p}}(m, m') = \frac{\overline{\sigma_{\text{ext,p}}(m, m')} - \overline{\sigma_{\text{ext,p}}(m^*, m'^*)}}{\overline{\sigma_{\text{ext,p}}(m^*, m'^*)}} \cdot 100\%, \tag{4.1}$$

and

$$\sigma_{\text{bsc,err,p}}(m, m') = \frac{\overline{\sigma_{\text{bsc,p}}(m, m')} - \overline{\sigma_{\text{bsc,p}}(m^*, m'^*)}}{\overline{\sigma_{\text{bsc,p}}(m^*, m'^*)}} \cdot 100\%. \tag{4.2}$$

It is defined as the error of the optical cross sections if the reference refractive index (m^* and m'^*) was assumed to be true but the real particles have a refractive index of m and m'. It can be concluded from this analysis that the maximum relative error for the given range of refractive indices is less than 10 % for the extinction cross section but ranges up to 230% for the backscatter cross section at the outer extremes of the uncertainty range.

The results are shown in Fig. 4.14 and 4.15 where the relative error is plotted for variable real parts and for variable imaginary parts compared to the reference values. As a conclusion from this analysis, the maximum relative error for the given range of
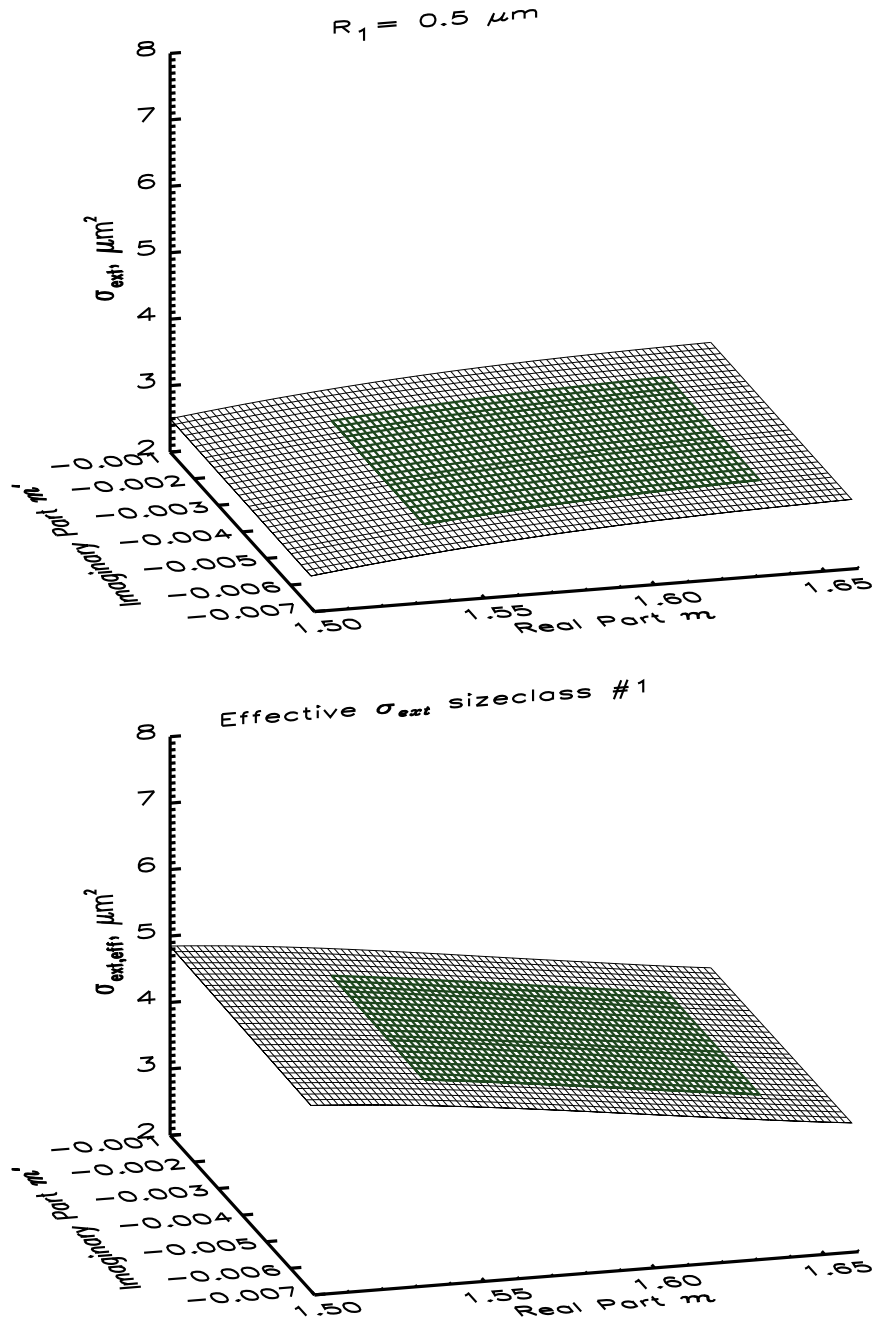
Figure 4.2: Sensitivity of σ_{ext} to the real and imaginary part of the refractive index for a single particle radius R_p (top) and after calculating the effective extinction cross section $\overline{\sigma_{ext}}$ (bottom) for particle size class 1. The green shaded area is the considered range of real part m and imaginary part m' for the uncertainty estimation as explained in section 4.1.
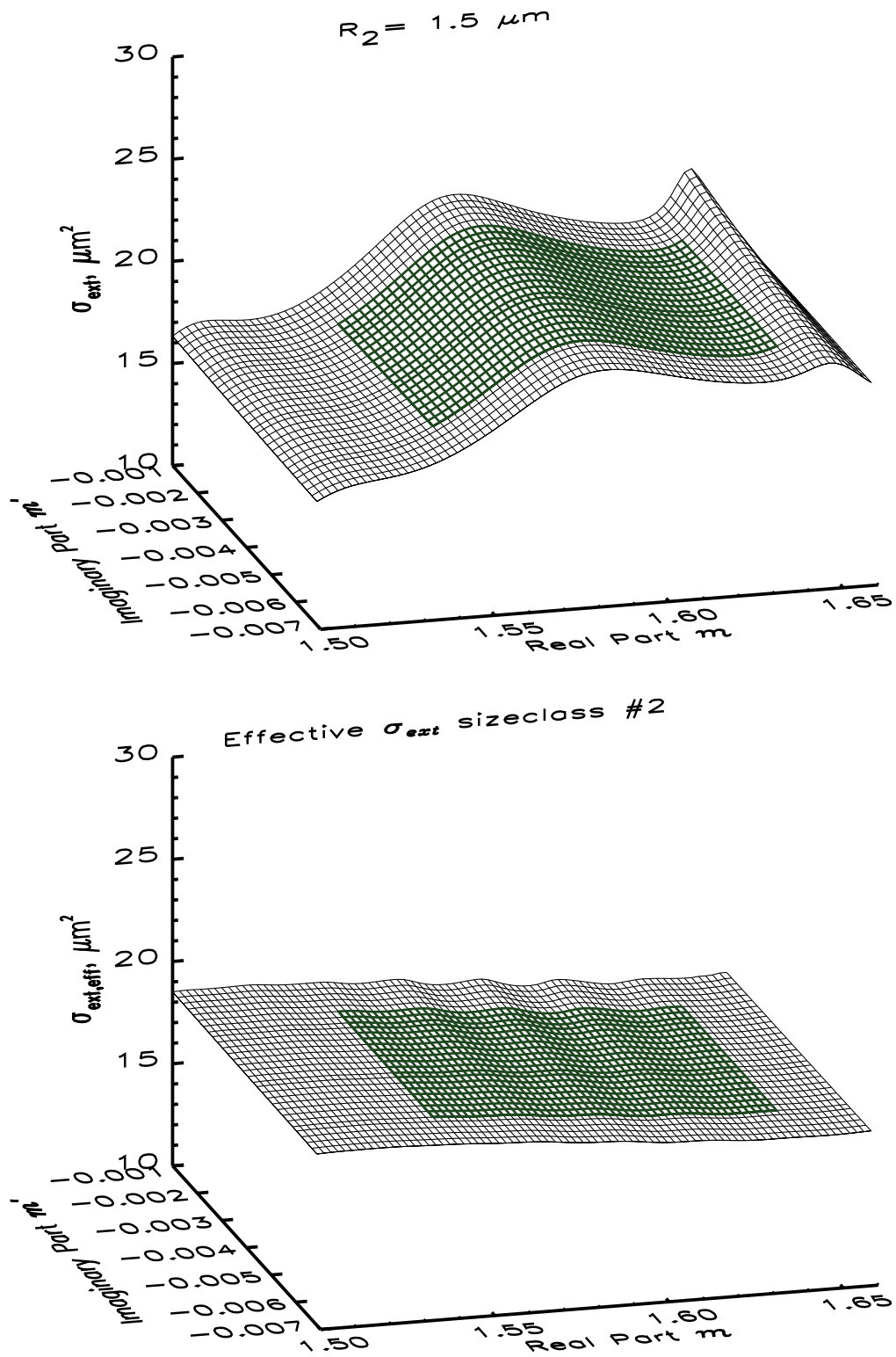
Figure 4.3: The same as 4.2 but for size class 2
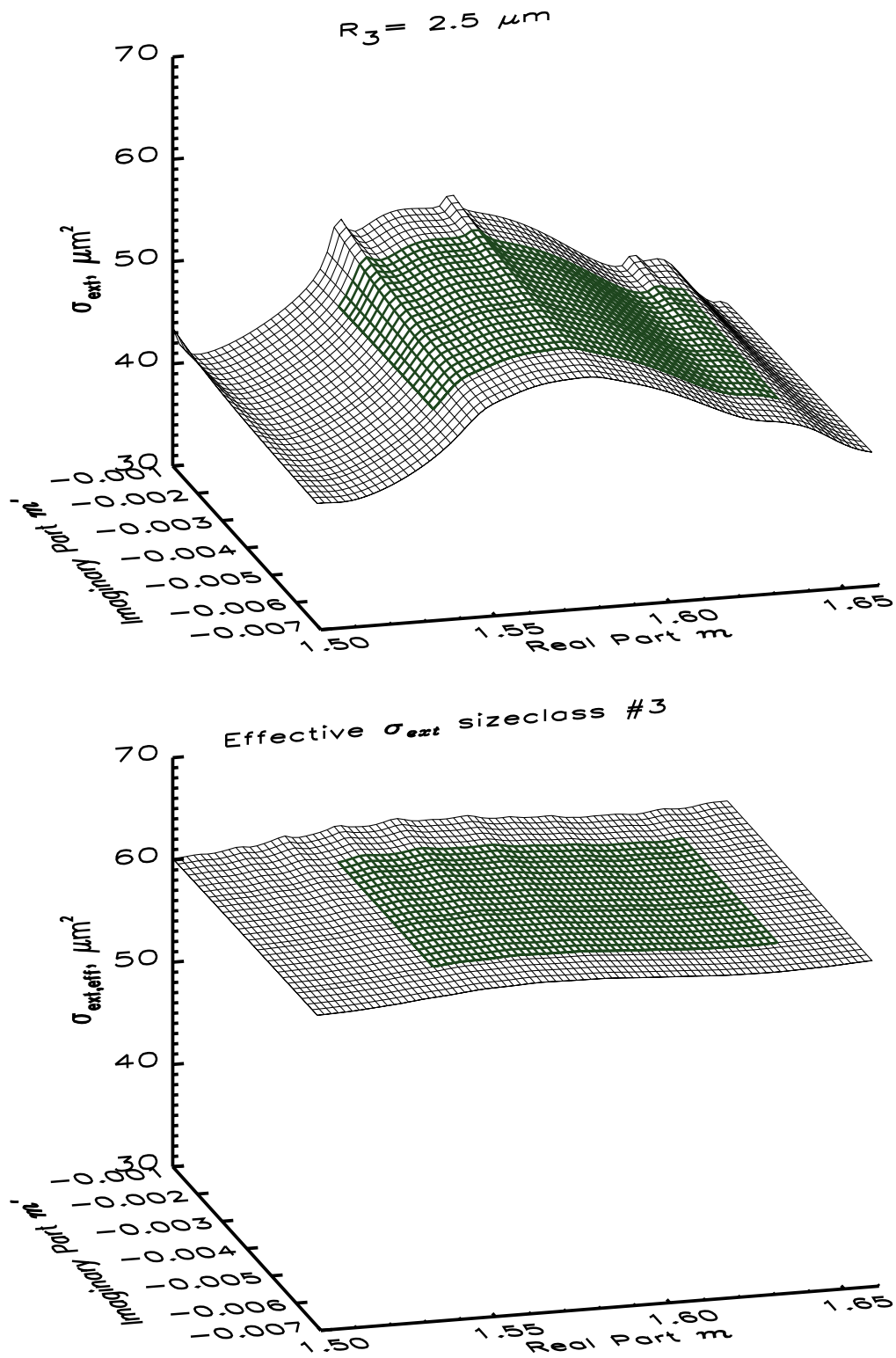
Figure 4.4: The same as 4.2 but for size class 3
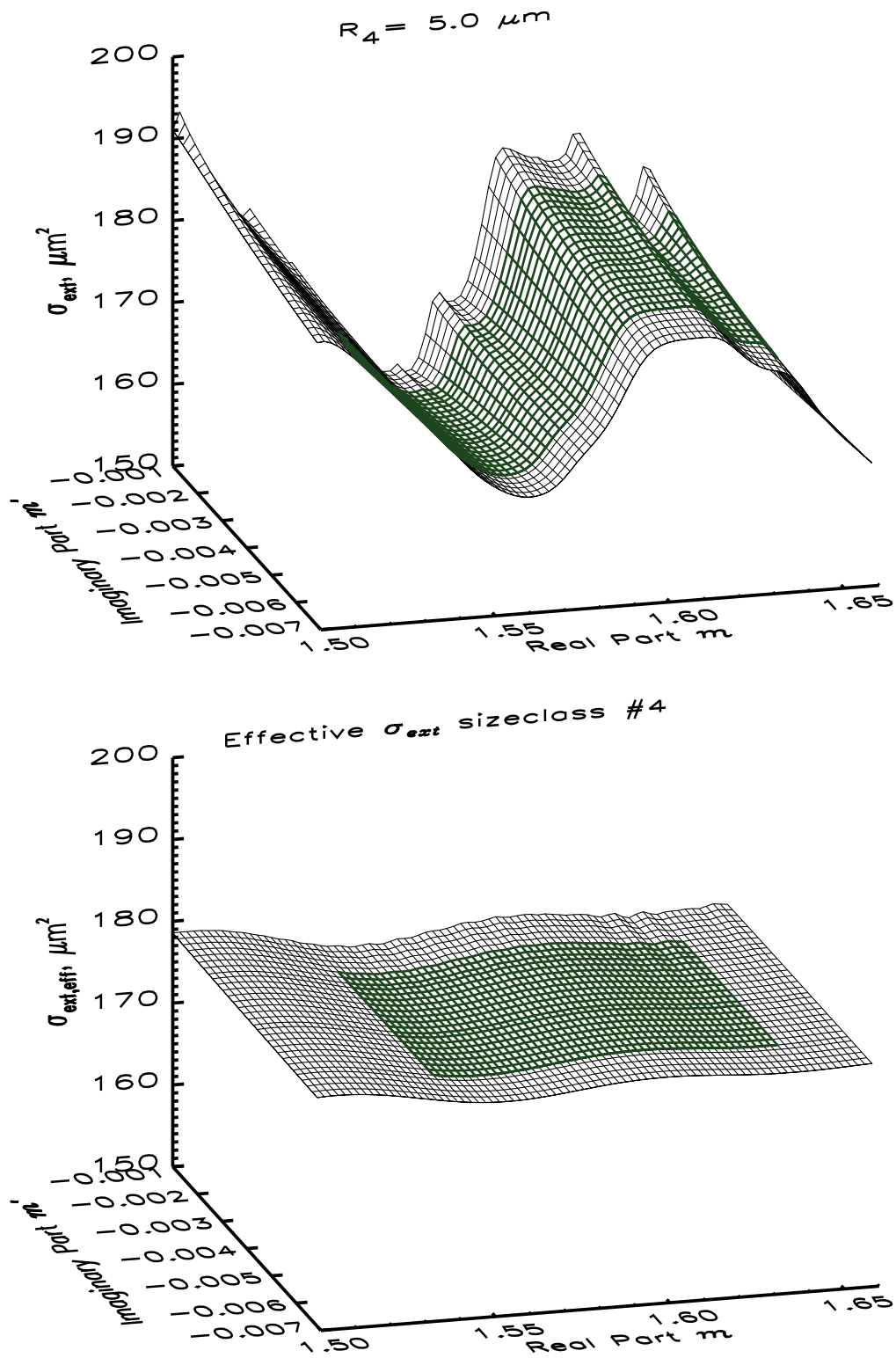
Figure 4.5: The same as 4.2 but for size class 4
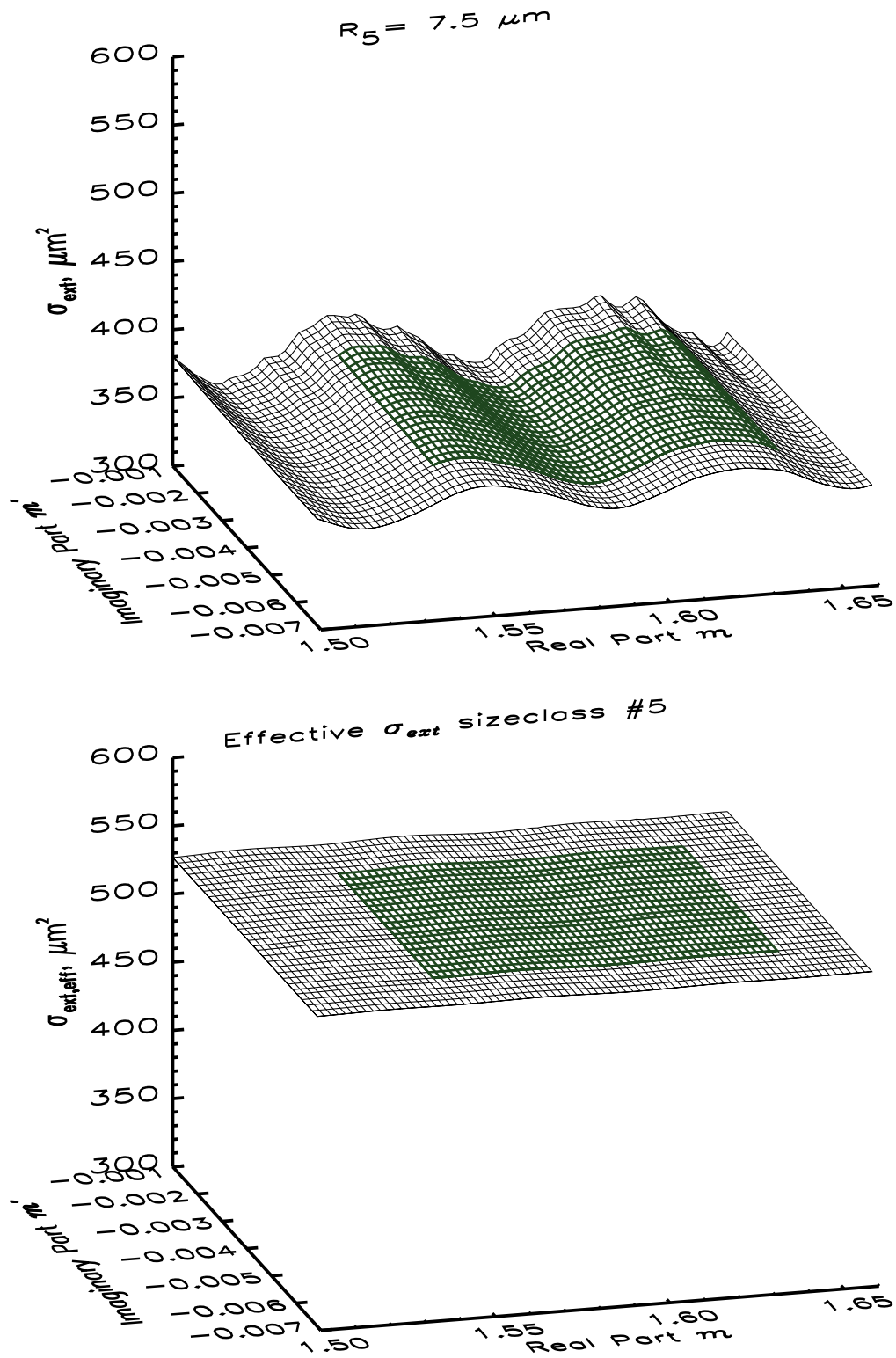
Figure 4.6: The same as 4.2 but for size class 5
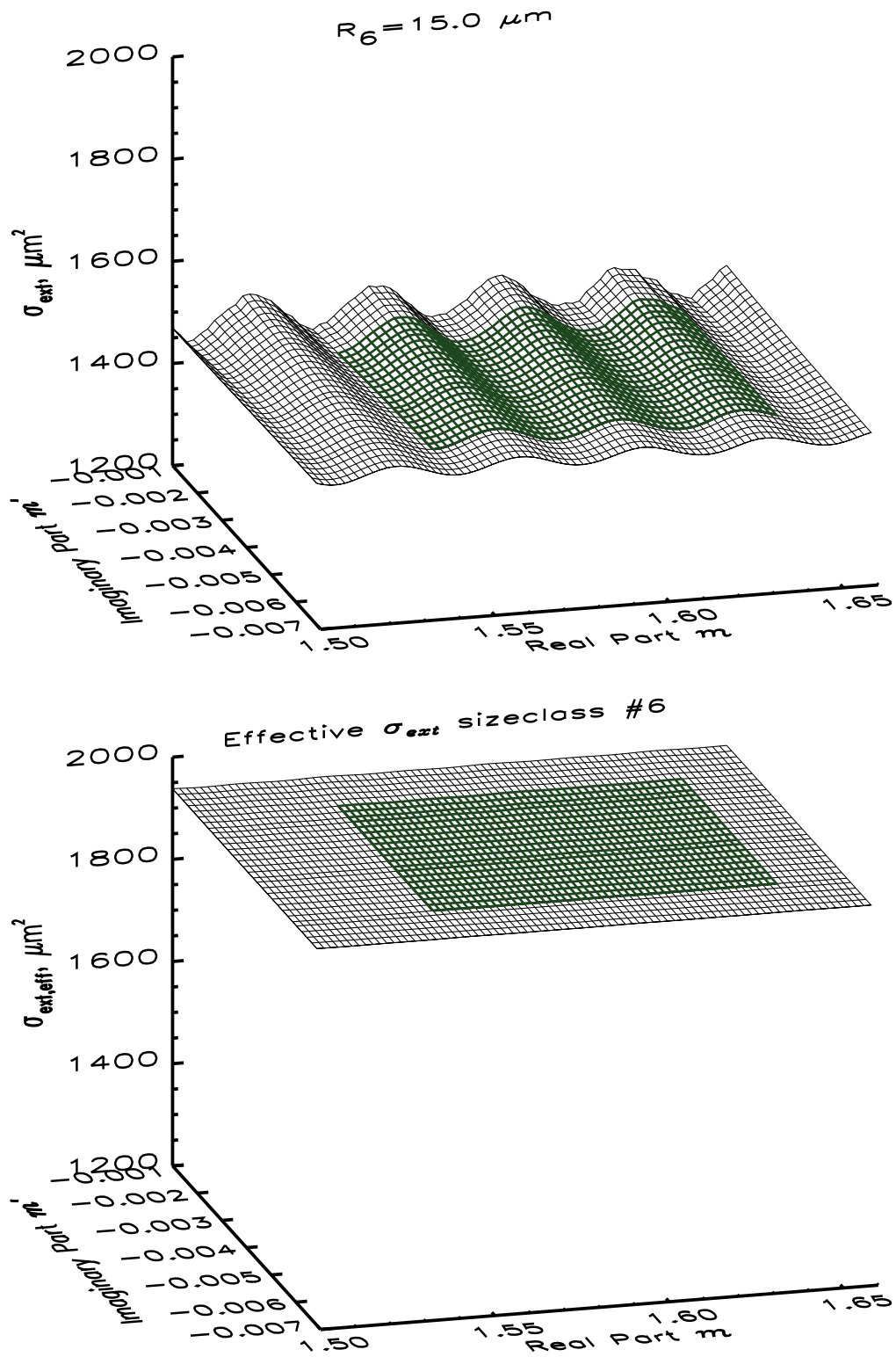
Figure 4.7: The same as 4.2 but for size class 6
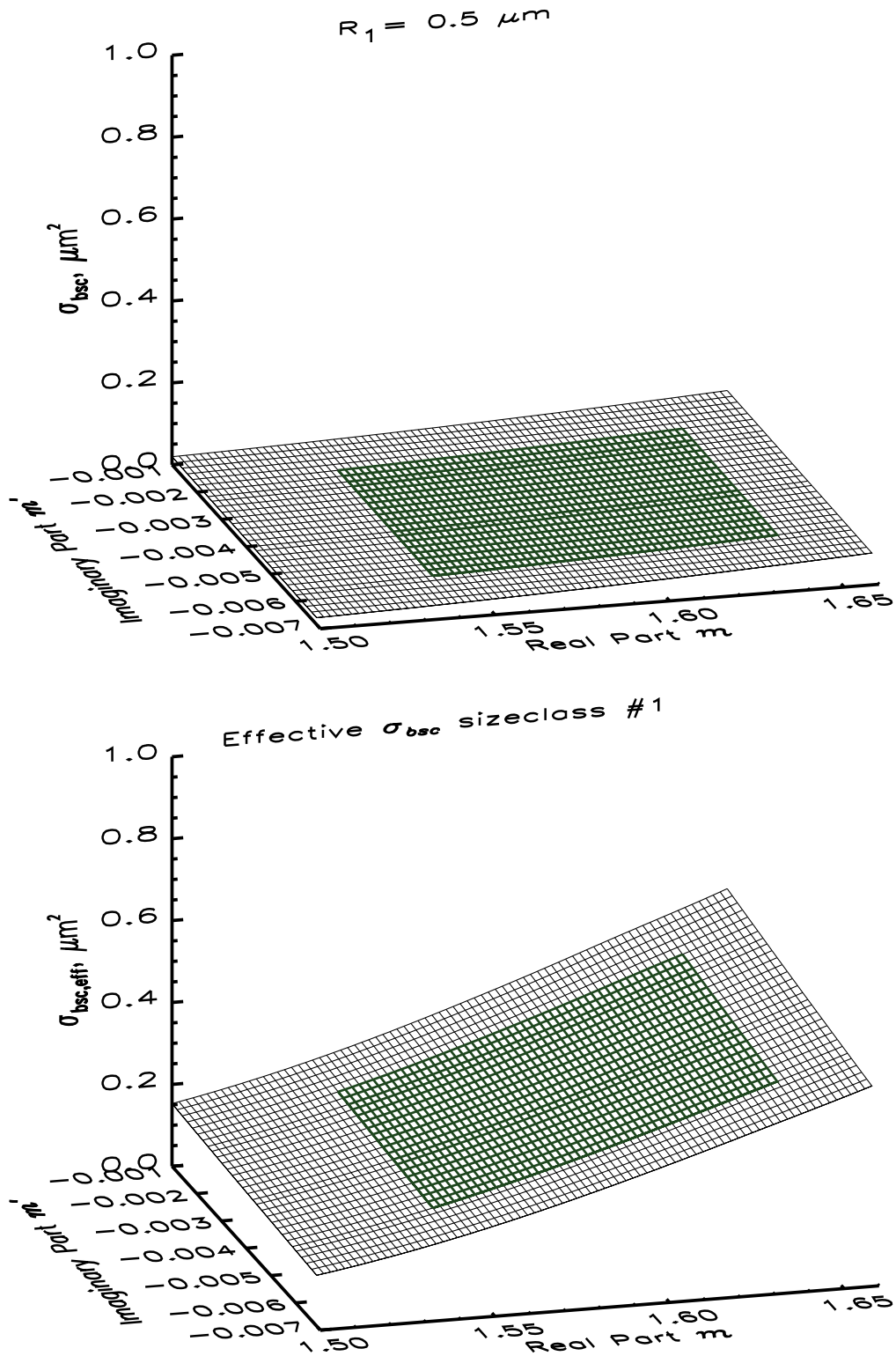
Figure 4.8: The same as Fig. 4.2 but for the backscatter cross section σ_{bsc} (top) and the effective backscatter cross section $\overline{\sigma_{bsc}}$ (bottom).
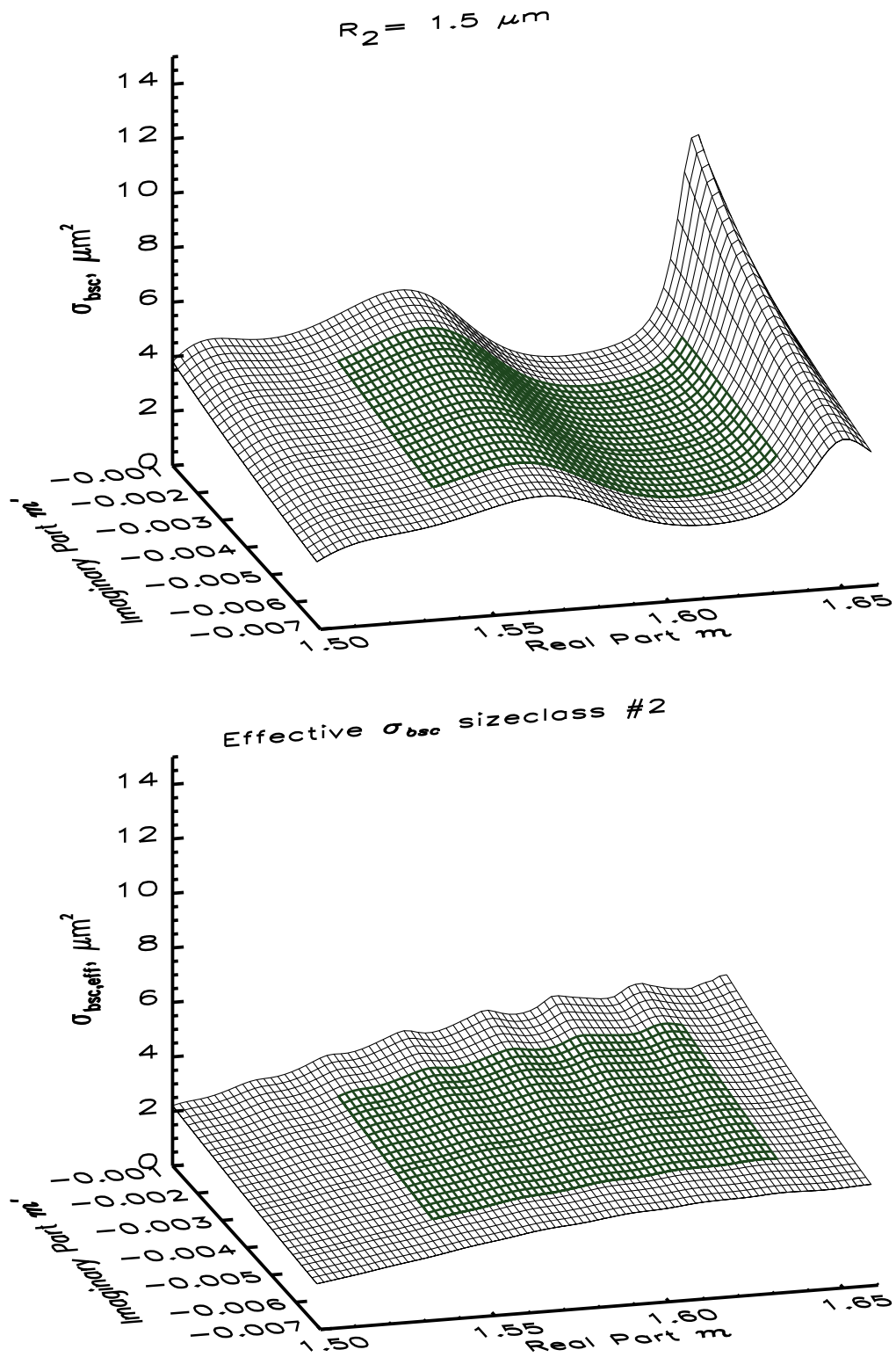
Figure 4.9: The same as 4.8 but for size class 2
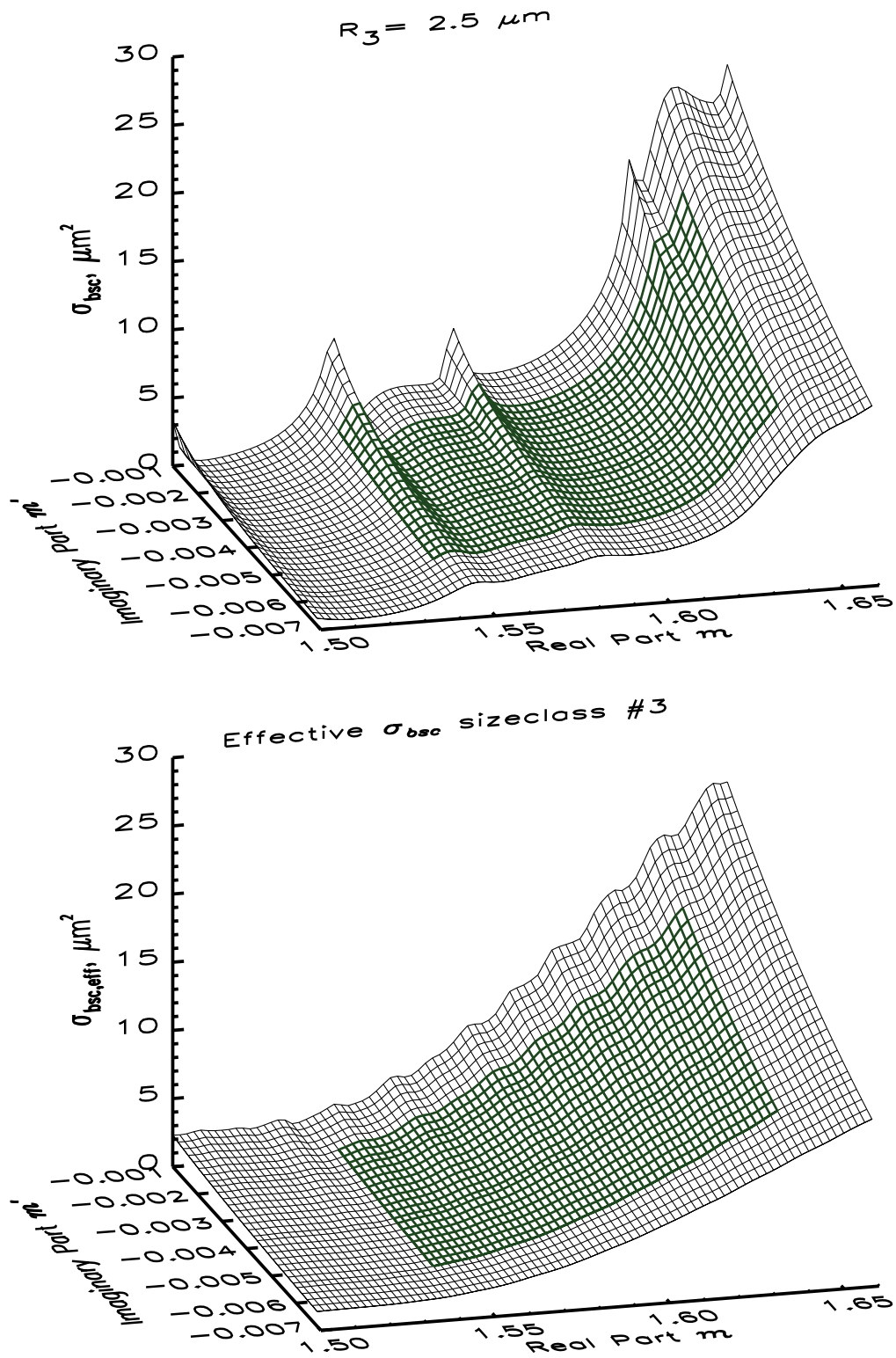
Figure 4.10: The same as 4.8 but for size class 3
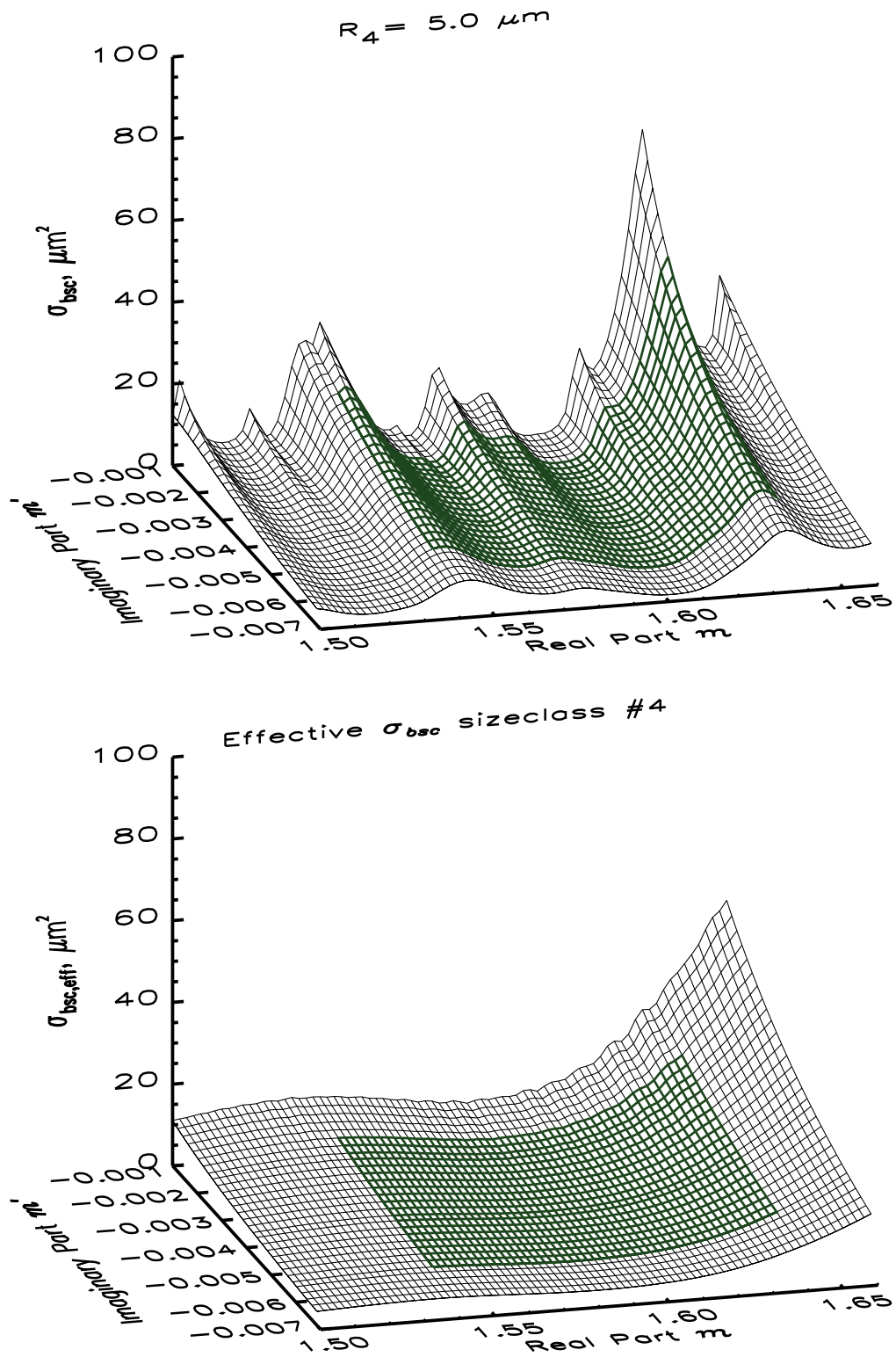
Figure 4.11: The same as 4.8 but for size class 4
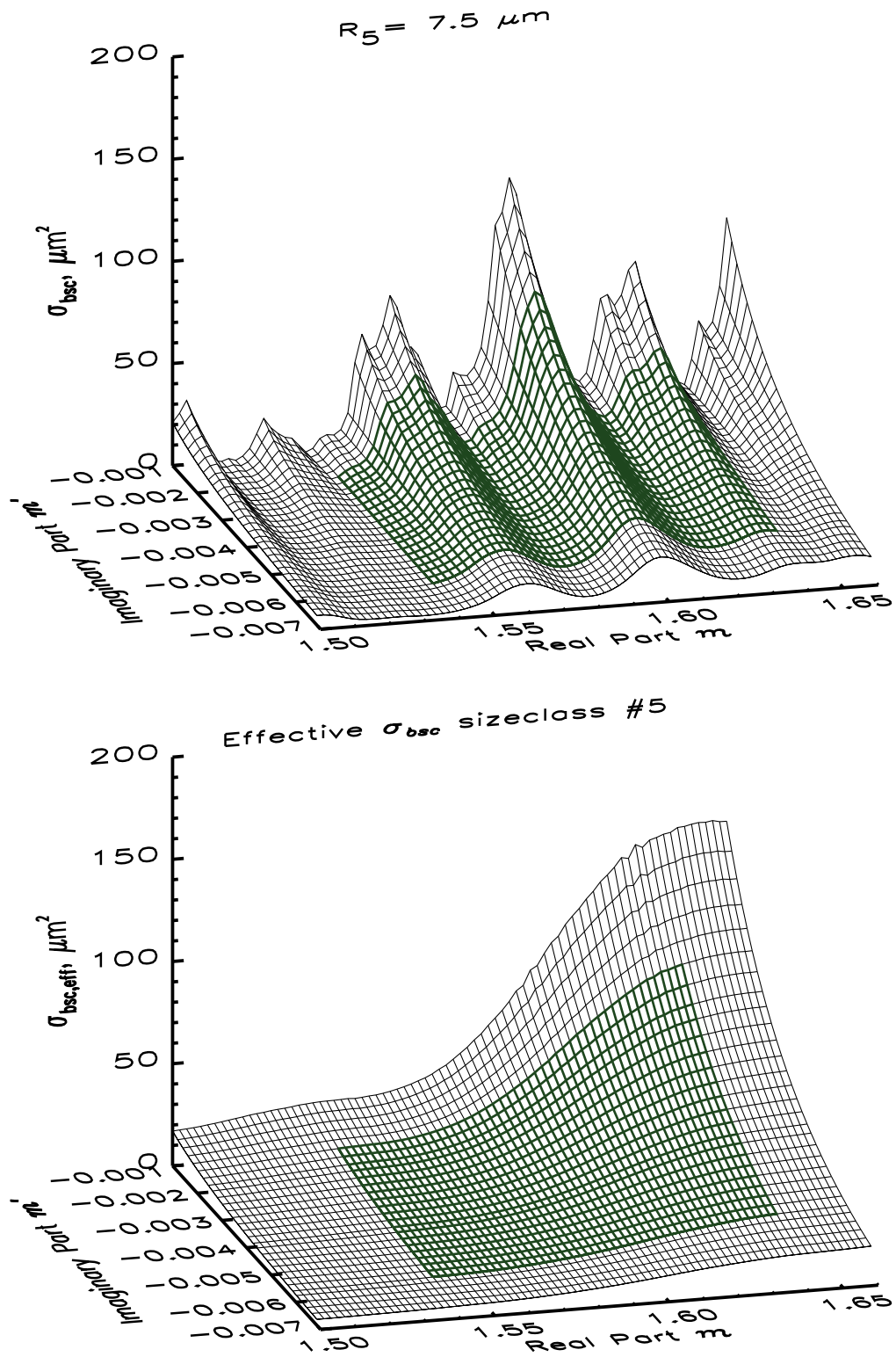
Figure 4.12: The same as 4.8 but for size class 5
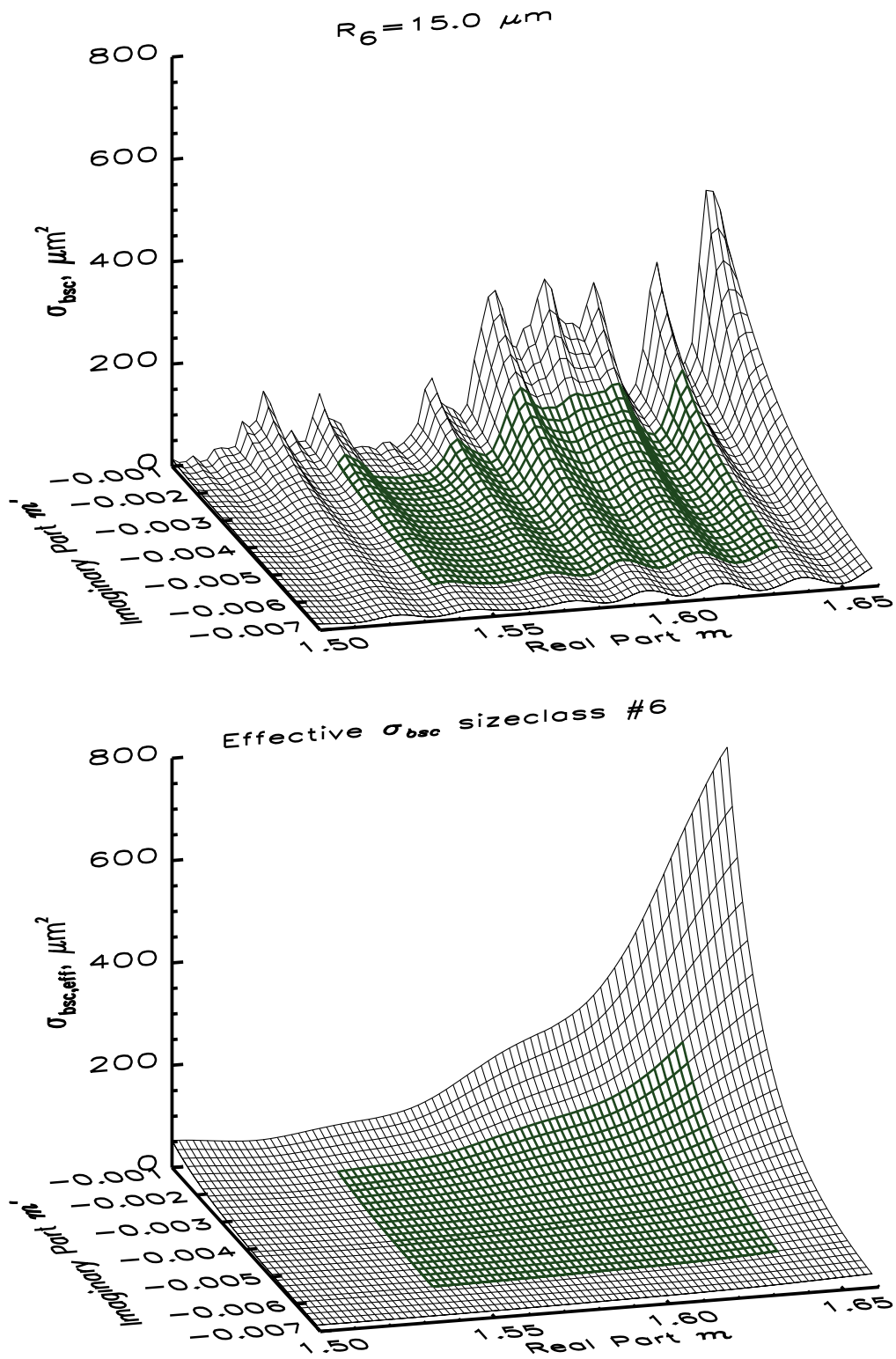
Figure 4.13: The same as 4.8 but for size class 6

refractive indices is less than 10 % for the extinction cross section but ranges up to 230% for the backscatter cross section.
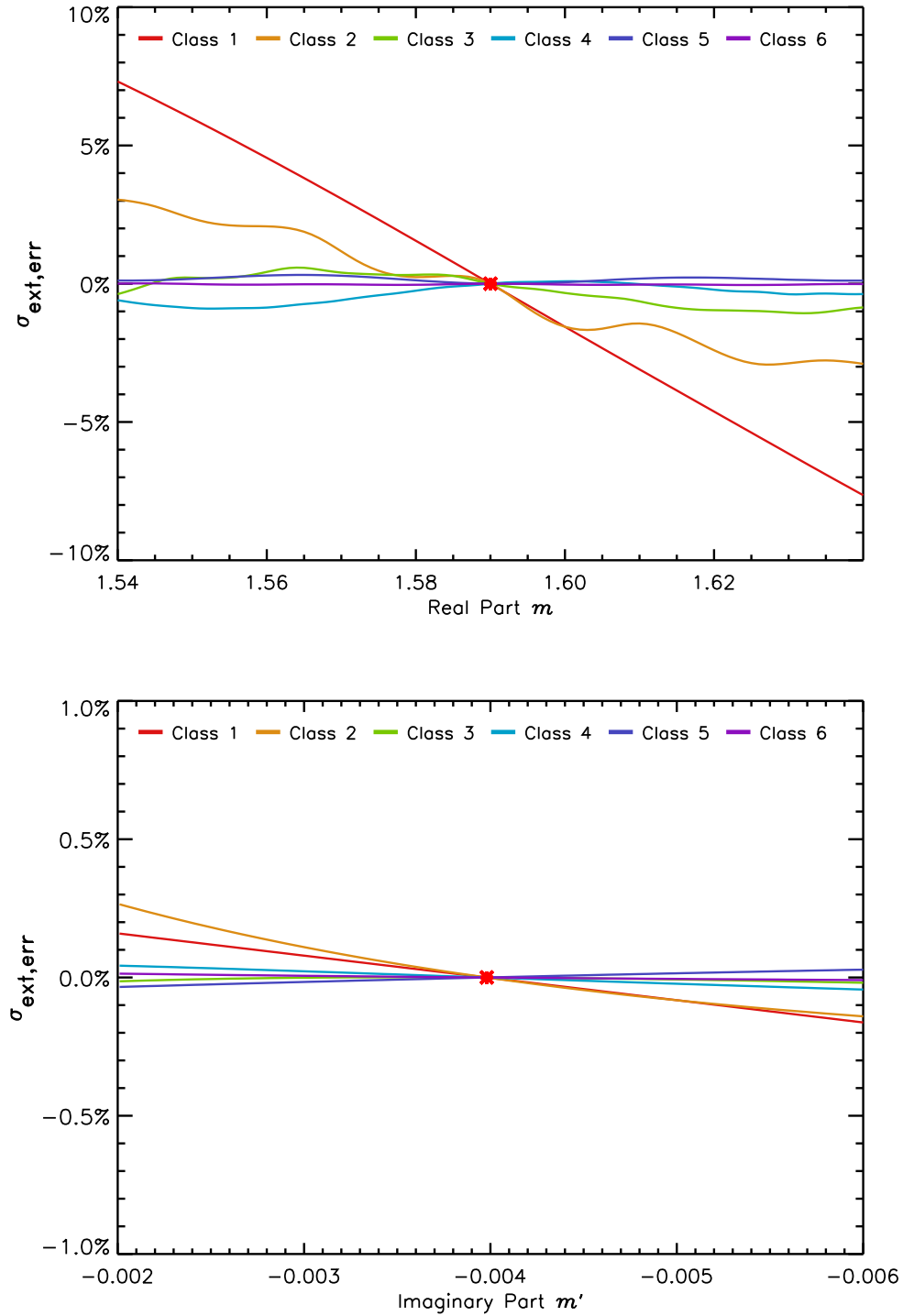
Figure 4.14: Relative errors of the effective extinction cross section if the assumed reference refractive index (1.59 - 0.004i) varies to the true refractive index. Uncertain real parts of the refractive index (top) may lead to errors of 7% for the effective extinction cross section. Uncertain imaginary parts of the refractive index (right column) may lead to a maximum error of 0.5% for the effective extinction cross section.
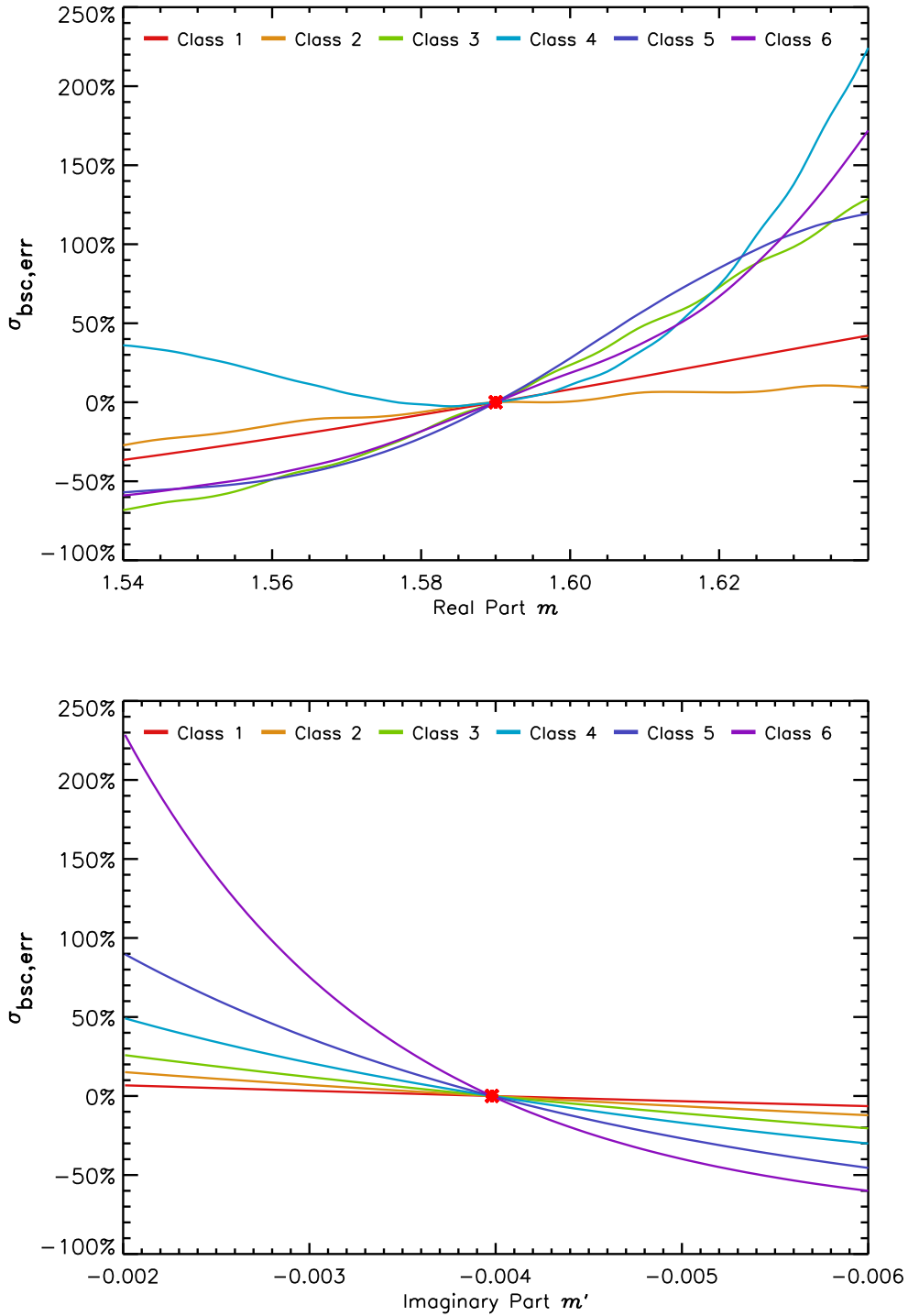
Figure 4.15: The sames as Fig. 4.14 but for the backscatter cross section. Uncertain real parts of the refractive index (top) may lead to errors of 225% for the effective backscatter cross section. Uncertain imaginary parts of the refractive index (bottom) may lead to a maximum error of 230% for the effective backscatter cross section. The maximum error was observed at the outer range of considered refractive indices. So reducing the considered range of refractive indices reduces the maximum error of the effective extinction and backscatter cross section.

Table 4.1: Settings of the T-matrix procedure for the particle shape sensitivity study. The parameters were kept constant during the study except the particle shape parameters (EPS and NP)

Variable	Value	Description
RAT	1	Radius is given as equal-sphere-volume radius
NPNAX	1	Setting for monodisperse distributions
AXMAX	1	Setting for monodisperse distributions
B	1D-1	Setting for monodisperse distribution
NKMAX	-1	Setting for monodisperse distributions
NDISTR	4	Setting for monodisperse distributions
EPS	0.5 ... 2.0	Aspect ratio of the scatterer
NP	-1 or -2	Selects the particle type (spheres NP=-1 or cylinders NP=-2)
LAM	1064.e-9	Wavelength of incoming light
MRR	1.59	Real part of the refractive index
MRI	-0.004	Imaginary part of the refractive index
NPNA	19	Number of random angles

4.4 SENSITIVITY TO THE PARTICLE SHAPE (BASED ON T-MATRIX ALGORITHMS)

T-matrix calculations performed in this study are based on the FORTRAN code for randomly oriented particles, written and provided by Mishchenko and Travis (1998). A detailed description of the method can be found in Mishchenko, Travis, and Lacis (2002).

The double-precision version of the T-matrix procedure was modified to perform scattering calculations of multiple particle sizes automatically. In addition to that, the procedure was extended by calculating and returning the backscatter cross section σ_{bsc} according to Mishchenko, Travis, and Lacis (2002), Eq. (9.10). These modifications were tested by comparing the scattering calculation results of the modified code and mie_single for spherical particles and the results were identical.

A list of T-matrix options which were used for the particle shape sensitivity study is Table 4.1. The most important particle properties are defined by the variables NP and EPS. NP is the particle type descriptor and has a value of -1 for spheres as well as for ellipsoids. A NP value of -2 is used for cylinders. The variable EPS is an expression for the objects' diameter to length ratio: An ellipsoid with EPS=1 is a sphere, prolate objects have EPS<1 and oblate objects have EPS>1, see Fig. 4.16.
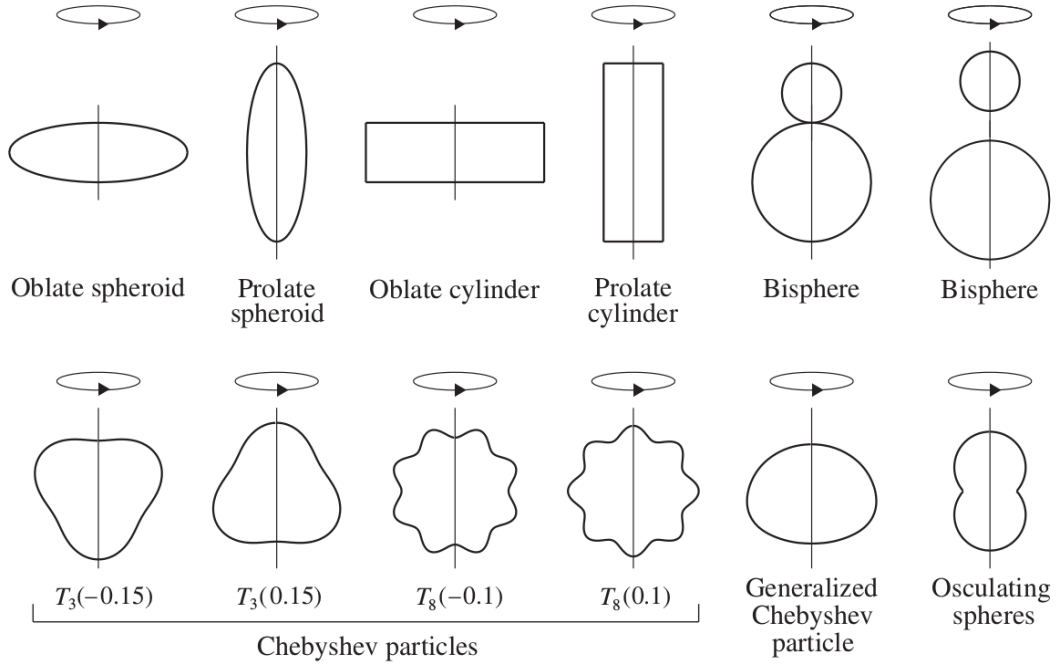
Figure 4.16: Particle shapes and particle shape definitions available at the T-matrix code provided by Mishchenko, Travis, and Lacis (2002). The shape types are rotationally-symmetric with variable shape properties, such as variable aspect ratio or Chebyshev polynomials. For the sensitivity studies presented in this study, the spherical, ellipsoidal and cylindric particle types were analyzed due to their alikeness to the particle shape of volcanic ash. An equivalent particle shape for irregularly and not rotationally-symmetric shaped volcanic ash particles, however, cannot be provided by the T-matrix method.

In Figs 4.17, 4.18, and 4.19, the optical cross sections and the pure lidar ratio of spheres and several aspherical particles are plotted against the equal-volume radius. The aspherical scatterers are 6 ellipsoids with a diameter-to-length-ratio of 0.50, 0.67, 0.75, 1.25, 1.50 and 2.00 as well as 5 types of cylindric particles with a diameter-to-length-ratio of 0.50, 0.80, 1.00, 1.25 and 2.00. Unfortunately, the scattering properties of a highly asymmetric ellipsoid (EPS: 0.50) is only available up to an equal-volume radius of 3.75 µm. For future research activities in this topic, the quadruple precision version of the t-matrix code could be used to extend the upper size range of highly asymmetric particles.

No significant differences between the extinction cross section of spheres and these ellipsoids were observable. By trend, however, cylindric shaped particles have a higher extinction cross section compared to ellipsoids. Spheres have the lowest extinction cross section values over the whole spectrum. Up to a volume equivalent radius of 0.7 µm, the shape effect is not noticeable.

Regarding the backscatter cross section, there are significant differences between the backscatter cross section of spheres and other shaped particles. Obviously, spheres are affected by interference effects which lead to both fluctuating and oscillating values of the backscatter cross section while the backscatter cross section spectrum of other shapes is only weakly fluctuating. As observed for the extinction cross section, the shape effect becomes pronounced beginning at an equal-volume radius greater than $0.7\,\mu m$. Spherical scatterers have a higher value of the backscatter cross section compared to ellipsoids except for one type of ellipsoid (EPS = 1.25). For cylinders, the backscatter cross section of the analyzed aspect ratios increases monotonically with size. As a result, the backscatter cross section of spheres is lower than of cylindric particles with the same size if their equal-volume radius is greater than $3.75\,\mu m$ (for the given wavelength of $\lambda = 1064\,nm$).

The particle shape effect on the pure lidar ratio is weakly pronounced for small particle sizes (less than $0.75\,\mu m$). For larger particles, the pure lidar ratio of spheres is generally lower than of the other considered shapes which is in agreement to the higher values of the backscatter cross section observed before. For the fourth size class (equal-volume radii around $5\,\mu m$), the previously observed interference effects of the spheres' backscatter cross section leads to extreme values of the pure lidar ratio (exceeding a value of $200\,sr$). For the size classes 2, 3 and 5, however, the pure lidar ratio of spheres is lower than of all other considered particle shapes except for cylinders. This indicates that the assumption of spherical scatterers results in an underestimation of the total lidar ratio if the considered particles are not spherical and size classes 2, 3, and 5 contribute predominately to the total volcanic ash number density.

A summary of the particle shape sensitivity study is shown in Figs 4.20 and 4.21, giving the relative differences of the effective optical cross sections for different particle shapes. The definition of the relative differences follows Eq. (4.1) and Eq. (4.2).

The effective extinction cross section of spheres is smaller than the effective extinction cross section of other analyzed asymmetric particles. Regarding the effective backscatter cross section, however, the maximum relative differences are 300% and -80%. While small aspherical particles have a lower value of the effective backscatter cross section compared to spheres, the effective values of the fourth size class are higher compared to almost all considered aspherical particles. From this analysis, it can be concluded that due to the assumption of sphericity, the backscatter cross section of size classes 1, 2 and 3 are overestimated by about factor 1.5 to 5 while the backscatter cross section of the fourth size class is underestimated by factor 2. This allows for quantifying the over- and underestimation of the results for each size class individually which is not possible for forward operators based on assuming a fixed lidar ratio.
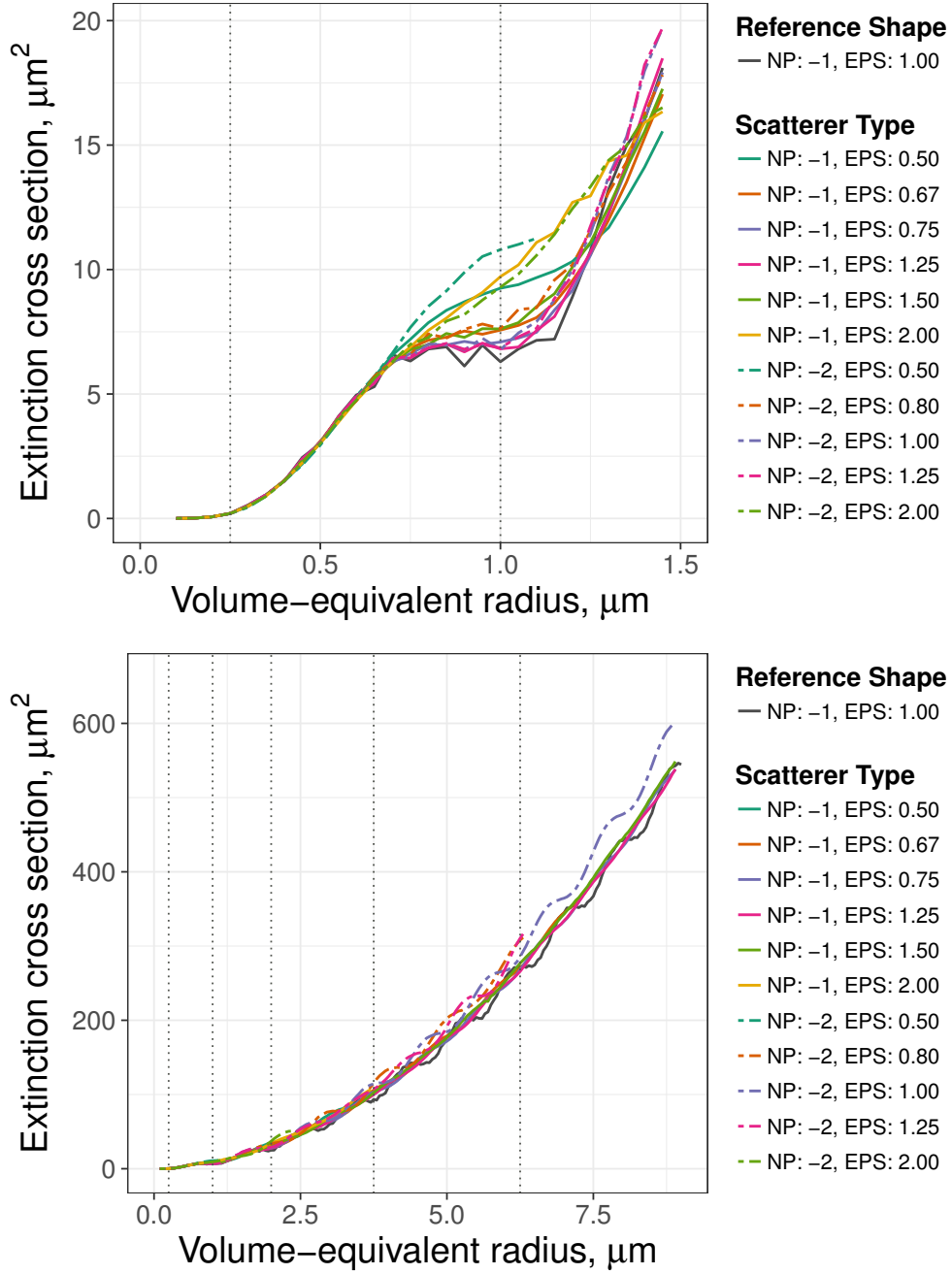
Figure 4.17: Extinction cross section spectrum for the reference particle (sphere: dark grey line), six types of ellipsoids (EPS:1: solid lines), and 5 types of cylinders (EPS:-2: dashed lines) against the particles' equal-volume radius R_p at $\lambda = 1064\,\text{nm}$. Vertical dotted lines indicate the size-margins of each class. The particle shape effect is negligible for particles with a radius much smaller than the wavelength. Particles which have a radius equal to the wavelength show differences of the extinction cross section depending on their shape. With larger particle sizes, the particle shape effect is negligible for the considered shapes and aspect ratios.
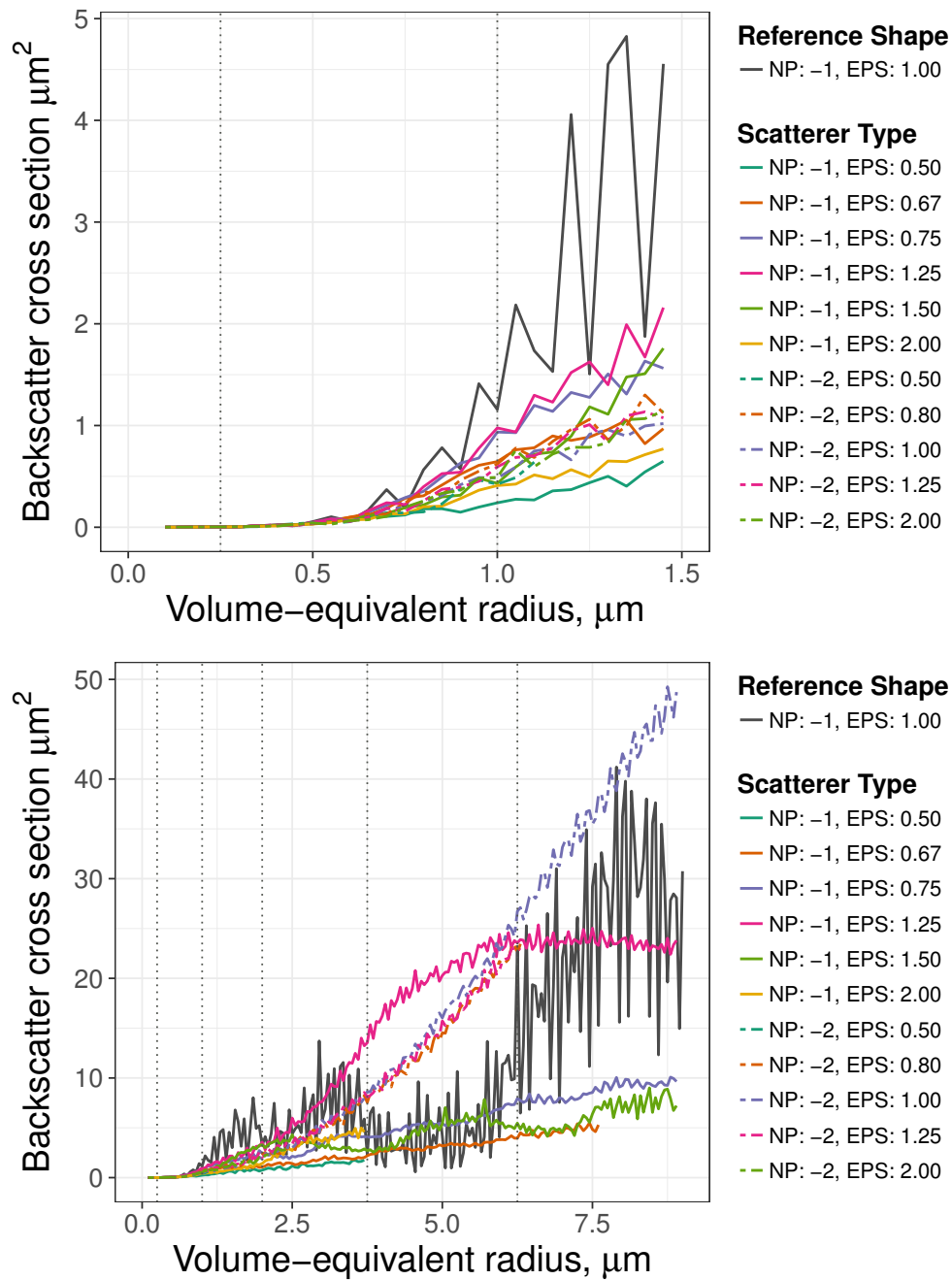
Figure 4.18: The same as Fig. 4.17 but for the backscatter cross section. A high particle shape sensitivity of the backscatter cross section can be observed which becomes pronounced for particles with radius greater than 0.5λ. While the backscatter cross section of ellipsoids increases only weakly with particle size, the backscatter cross section of cylinders increases nearby exponentially with size. The backscatter cross section spectrum of spheres has larger-scale fluctuations which are due to interference effects. For particle size classes 4 and 5, the backscatter cross section of spheres is between the values of ellipsoids and cylinders which indicates that a spherical shape is a valid representative for large volcanic ash size classes
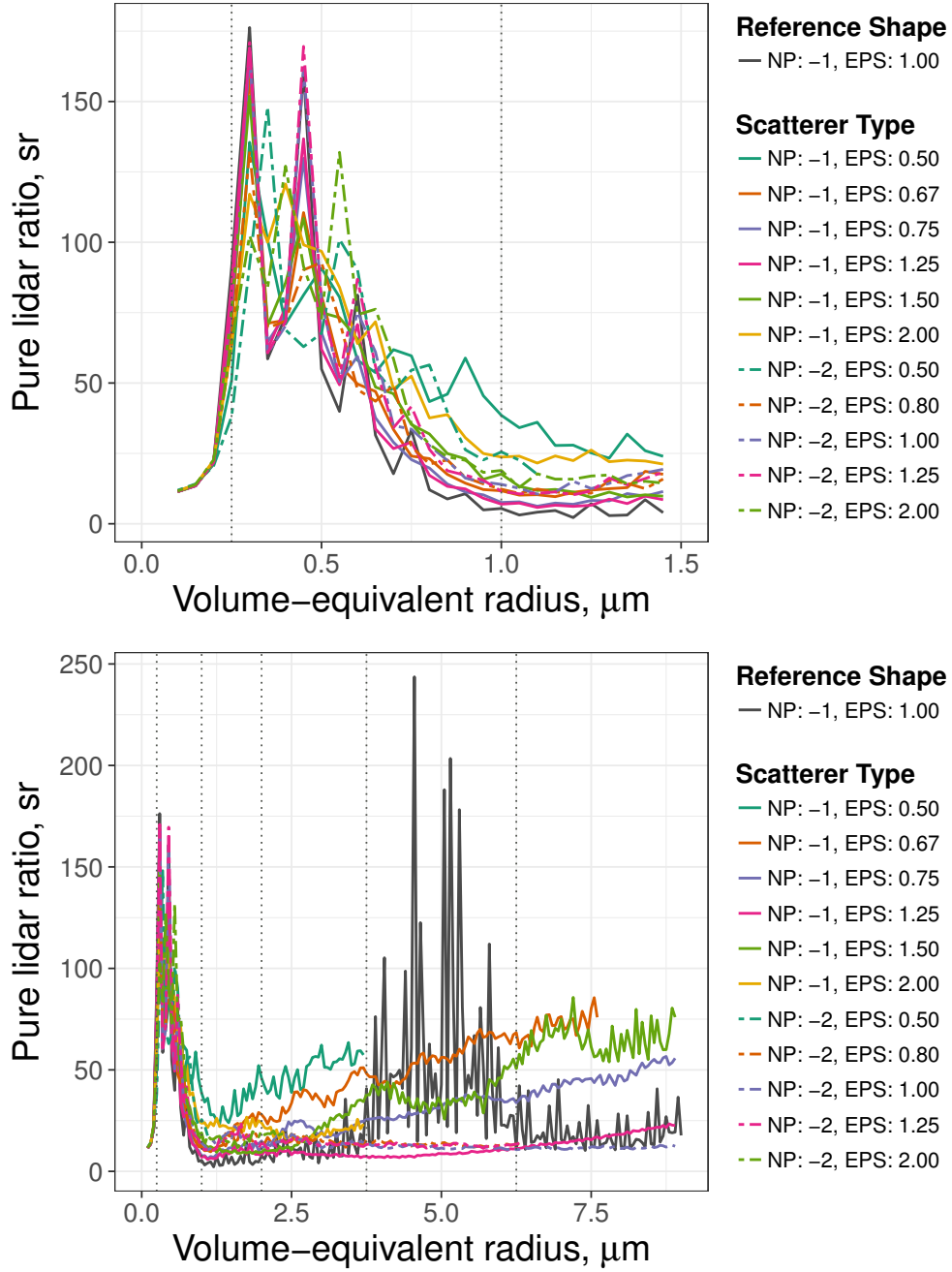
Figure 4.19: The same as Fig. 4.17 but for the pure lidar ratio. Similar to the observations for the backscatter cross section (see Fig. 4.18), the particle shape sensitivity of the pure lidar ratio is negligible for particles smaller than 0.5λ. For larger particles, the spherical shape tends to have the lowest pure lidar ratio value of all particle shapes (namely for a particle radius between 0.5 μm and 3.5 μm. Peaks of the pure lidar ratio are observed for spheres with a radius between 4 μm and 6 μm which are due to interference effects. Large ellipsoids tend to have the highest pure lidar ratio values in comparison with other particle shapes; large cylinders have an almost constant value of the pure lidar ratio of about 15 sr.
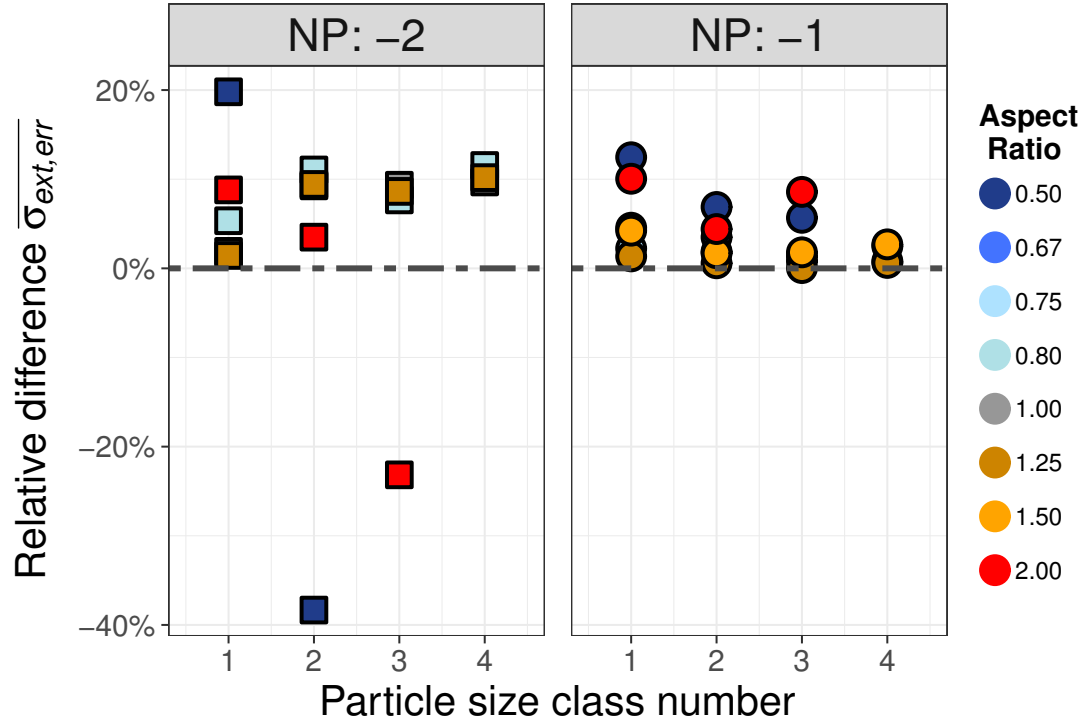
Figure 4.20: Relative errors of the effective extinction cross section if spherical particles are assumed but the real particles are of elliptical (NP: -1) or cylindrical shape (NP: -2). Negative values indicate that spherical particles have a larger effective extinction cross section than equal-sized non-spherical particles and vice versa. The maximum relative differences are 11 % and −35 %.
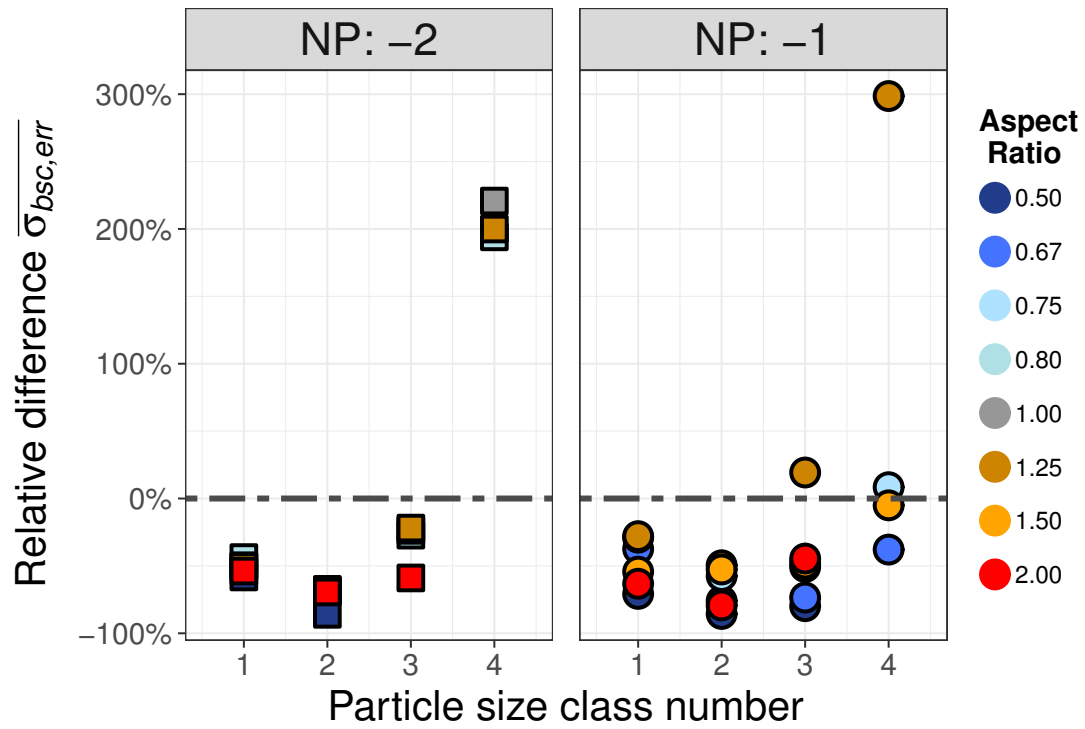
Figure 4.21: The same as Fig. 4.20 but for the effective backscatter cross section. The maximum relative difference between the effective backscatter cross section of spherical and non-spherical particles are observed for size class 2 with a relative difference of up to $-80\,\%$ (resulting in a difference factor of 5). But also for other size classes, the relative difference is about factor 2 when assuming spherical shape for the considered non-spherical particle shapes.

5 RESULTS

5.1 SCATTERING PROPERTIES OF VOLCANIC ASH USED WITHIN THE FORWARD OPERATOR

A list of effective extinction cross section and effective backscatter cross section values for atmospheric gas molecules and for the six volcanic ash size classes is shown in Table 5.1.

5.2 OUTPUT VARIABLES OF THE FORWARD OPERATOR

Using the forward operator allows for plotting each variable of the lidar simulation for analytic purposes (see Fig. 5.1). These plots of forward operator output variables are representing the major characteristics of the variables: strong extinction and strong backscattering are usually related. Time and height intervals where only molecules exist lead to low values of the extinction coefficient and backscatter coefficient. Due to a decrease of the atmospheric gas number density with height, both extinction and backscatter coefficient decrease with height in an aerosol-free atmosphere. The two-way transmission decreases with height (see Eq. (2.27)).

In comparison with Raman lidar measurements, both the maximum measured extinction coefficient ($4.0 \times 10^{-4}\,\mathrm{m}^{-1}$) and backscatter coefficient ($8.0 \times 10^{-6}\,\mathrm{m}^{-1}\,\mathrm{sr}^{-1}$) inside the volcanic ash plume (Ansmann et al., 2010) are nearby equal to the respective maximum values output by the forward operator at the station Deuselbach: The Raman lidar measured values are slightly lower than the values output by the forward operator which could be due to assumptions related to the forward operator or due to an over-estimation of the COSMO-ART predicted aerosol number density.

From output of the forward operator, the relative contribution to the total signal and to the total mass density can be analyzed for each size class of COSMO-ART and also the total lidar ratio can be calculated. This was done exemplary for two time-height coordinates: The first coordinate points to model output from a coordinate inside the volcanic ash layer (Table 5.2). Coordinate 2 points to a coordinate where the major fraction of the particle mass is contributed by size classes 4 and 6 (see Table 5.3).

Regarding coordinate 1, the total backscatter coefficient is dominated by ash size classes 1, 2 and 3 while the signal contribution of classes 4 to 6 is less than 5 % in total. The mass contribution is dominated by classes 3 and 4 while classes 2, 5 and 6 are contributing by 10 % each to the total mass density. The total lidar ratio is 9.63 sr. Regarding coordinate 2, the total backscatter coefficient depends by about 68 % from

Table 5.1: Effective optical cross sections of atmospheric gas molecules and six volcanic ash size classes calculated for the ACL wavelength ($\lambda = 1064\,\text{nm}$). While the effective extinction cross section increases nearby exponentially with the particle class size, the effective backscatter cross section does not even scale linearly. In consequence, the ACL measured attenuated backscatter coefficient is less sensitive to size class 6 than to size class 3 etc.

Scatterer Class	$\overline{\sigma}_{\text{ext}}$ (m^2)	$\overline{\sigma}_{\text{bsc}}$ (m^2 sr^{-1})
Atmospheric Gas	3.125×10^{-32}	3.680×10^{-33}
Ash 1 (1 µm)	4.324×10^{-12}	0.328×10^{-12}
Ash 2 (3 µm)	17.821×10^{-12}	3.843×10^{-12}
Ash 3 (5 µm)	61.672×10^{-12}	6.200×10^{-12}
Ash 4 (10 µm)	177.045×10^{-12}	5.365×10^{-12}
Ash 5 (15 µm)	526.967×10^{-12}	20.442×10^{-12}
Ash 6 (30 µm)	1937.387×10^{-12}	23.781×10^{-12}

class 4 and by 30 % from class 6. The mass contribution at coordinate 2 is also dominated by the classes 4 and 6. But in contrast to the backscatter coefficient, class 6 has a higher contribution to the total mass density than class 4. The total lidar ratio at this coordinate with predominately large particles is 46.53 sr.

General conclusions from this analysis require further investigation. For an application of the forward operator in this study, however, there are two aspects to be mentioned: First, the backscattering intensity inside the volcanic ash layer (coordinate 1) is predominantly dependent on classes 1, 2 and 3 whose backscatter cross sections are also overestimated by the forward operator due to the assumption of sphericity (see Fig. 4.21). The real values of the total lidar ratio may be by factor 2-3 higher in certain cases (see Sect. 4.4). Second, the larger particles of classes 4, 5 and 6 carry a large portion of the mass but contribute only weakly to the total backscattered signal. This may be relevant for the selection and composition of future ACL networks. Prior studies confirm that even the systems operating at a relatively long wavelength of 1064 nm have a reduced sensitivity for giant and ultra giant particles (Madonna et al., 2013).

5.3 QUALITATIVE COMPARISON OF MEASURED AND FORWARD MODELED PROFILES

A qualitative comparison allows for the identification of common and different structures between the measured and simulated lidar profiles. Different ash layer structures

Table 5.2: Point-data extraction of COSMO-ART output at ACL station Deuselbach; coordinate 1 is at 16 April 2010, 18:00 UTC, in a height of 1.9 km ASL. Using the number density N_d of volcanic ash class d, the individual backscatter coefficient $\beta_{par,d,\lambda}$, the contribution to the total backscatter coefficient $\sum \beta_{par,d,\lambda}$, the individual mass density ρ_d, and the contribution to the total mass density $\sum \rho_d$ were calculated. Ash particles were calculated using a volumetric mass density of 2500 kg m^{-3}. A non-linear relationship between the relative contribution to the total backscatter coefficient and the relative contribution to the transported mass of an ash size class can be observed: While the first three classes contribute by 95 % to the total backscatter coefficient, they carry only 78 % of the volcanic ash mass. This dependency to the laser wavelength can be used as advantage for multi-wavelength lidar systems.

d	N_d	$\beta_{par,d,\lambda}$	$\frac{\beta_{par,d,\lambda}}{\sum \beta_{par,d,\lambda}}$	ρ_d	$\frac{\rho_d}{\sum \rho_d}$
-	m^{-3}	m^{-1} sr^{-1}	-	kg m^{-3}	-
1	43 653 522	1.4×10^{-5}	22.3 %	0.57×10^{-7}	3.3 %
2	7 044 794	2.7×10^{-5}	41.9 %	2.49×10^{-7}	14.2 %
3	3 194 338	2.0×10^{-6}	30.7 %	5.23×10^{-7}	29.8 %
4	462 402	2.5×10^{-6}	3.8 %	6.05×10^{-7}	34.5 %
5	37 161	7.6×10^{-7}	1.2 %	1.64×10^{-7}	9.3 %
6	4474	1.1×10^{-7}	0.2 %	1.58×10^{-7}	9.0 %

can hint, e.g., to errors in the model dynamics, in the source description, or in the sedimentation parametrization. If ash structures are found only in the measured profiles, either the model prediction is wrong or it misses an important aerosol type which is not present in the model. If structures are visible in the forward modeled profiles but missing in the measured profiles, either the ACL signal is too weak because of high extinction in lower heights or the model performed a wrong ash prediction. But it is also possible that the model overestimates the ash concentration so the structures are below the detection limit of the ACL measurements.

For a qualitative comparison between measurement and simulation, the ACL station Deuselbach in West Germany and a time interval from 16 to 17 April 2010 was chosen. Here, the ash layer was clearly visible in the measured profiles without being affected by low-level or high-level clouds. After calculating the attenuated backscatter coefficient from the ACL measurement according to Eq. (3.2) and extracting the common time and height intervals, the ACL data was finally re-sampled to the model resolution to get comparable datasets.

A comparison of ACL measurement and COSMO-ART simulation with an applied forward operator at the ACL station Deuselbach in West Germany is shown in Fig. 5.2. Ash layers are clearly visible in the measured profiles without being affected by

Table 5.3: The same as Table 5.2 but for coordinate 2 at 16 April 2010, 09:00 UTC, in a height of 1.5 km ASL. Even if class 4 carries only 27 % of the mass, it contributes by 67 % to the total backscatter coefficient. The inverse situation can be observed for size class 6 which holds 73 % of the mass but contributes by 30 % to the backscatter coefficient.

d	N_d	$\beta_{\text{par},d,\lambda}$	$\frac{\beta_{\text{par},d,\lambda}}{\sum \beta_{\text{par},d,\lambda}}$	ρ_d	$\frac{\rho_d}{\sum \rho_d}$
-	m^{-3}	$\text{m}^{-1}\,\text{sr}^{-1}$	-	$\text{kg}\,\text{m}^{-3}$	-
1	93.0	30.7×10^{-12}	0.2 %	0.01×10^{-9}	0.1 %
2	97.0	372.5×10^{-12}	2.8 %	0.01×10^{-9}	0.1 %
3	1.0	6.2×10^{-12}	0.1 %	0.01×10^{-9}	0.1 %
4	1700.0	9129.0×10^{-12}	67.3 %	2.23×10^{-9}	27.1 %
5	0.5	10.2×10^{-12}	0.1 %	0.01×10^{-9}	0.1 %
6	169.0	4018.8×10^{-12}	29.6 %	5.97×10^{-9}	72.8 %

low-level or high-level clouds. Due to the inevitable instrumental noise, the automatic calibration of ACL system and subsequent background subtraction, some data points are negative which is just a statistical effect but causes missing data in the log-scale plots. Volcanic ash plumes are clearly visible on both plots. Looking at the forward operator result, the ash layer crosses the ACL station between 06:00 UTC and 12:00 UTC at 16 April 2010. The layer height decreases with time and partially entrains into the planetary boundary layer where it persists even at the end of 17 April 2010. As both model and forward operator only represent volcanic ash and air molecules, the ash layers can be tracked within the planetary boundary layer. This is not possible using ACL measurements alone as the volcanic ash signal is tainted by other aerosol types. It is, however, difficult to determine unambiguously which ash layer structure observed by the ACL instrument can be related to the appropriate structures simulated by the model. Regarding the thin volcanic ash layer which is measured by the ACL instrument in a height between 7 and 9 km ASL at 16 April 2010, 06:00 UTC, this feature could be equivalent to the model prediction of ash layers in a height of 6 km ASL at 7:00 UTC. In this case, the model would have performed a rather precise prediction with only one hour time lag and a two km vertical shift. But it is also possible that the predicted ash entrainment over the ACL station is equivalent to the ash-indicating ACL signals at around 12:00 UTC. In the latter case, the model prediction would be wrong by a time lag of about 6 hours which is insufficient for time-critical applications.

The qualitative comparison is currently limited to coordinates where the major fraction of scatterers is represented by both model and forward operator. There are, however, some scatterer fractions still missing on the present model runs for a comprehensive comparison: Other aerosol types than volcanic ash like anthropogenic emissions,

mineral dust, soot, pollen, etc., are not included which leads to differences especially in the planetary boundary layer. It is hard to predict yet whether the strong ACL signal in the planetary boundary layer is related to background aerosol extinction or errors of the COSMO-ART prediction. To further investigate this problem, future studies with additional types of aerosols incorporated into the model are required.

5.4 COMPARISON OF MEASURED AND FORWARD MODELED PROFILES

A comparison of ACL measured and BaLiFOp forward modeled vertical attenuated back-scatter coefficient profiles allows for detailed comparison of the vertical structure and the absolute values of the attenuated backscatter coefficient. Two example profile comparisons are shown in Fig. 5.3, namely profiles at 16 April 2010, 18:00 UTC and 17 April 2010, 04:40 UTC. The first profile is from the same time coordinate as sample coordinate 1 in section 5.2. Before plotting, the ACL profiles were gridded again to the model's vertical and temporal resolution, i.e. variable vertical resolution and a time resolution of 15 minutes.

Regarding the first profile at 16 April 2010, 18:00 UTC, the vertical profiles of ACL and forward modeled attenuated backscatter coefficient are only weakly correlated. While the BaLiFOp output profile exceeds attenuated backscatter coefficient values of $1.0 \times 10^{-5}\,\mathrm{m^{-1}\,sr^{-1}}$, the ACL attenuated backscatter coefficient at the same height is limited to $1.0 \times 10^{-6}\,\mathrm{m^{-1}\,sr^{-1}}$. Also, the ACL profile has only two peaks at 1.8 and 4.0 km while the BaLiFOp profile exceeds these values constantly in heights from near ground to 4.0 km. This discrepancy could be due to errors of the model prediction or due to clipping effects of the ACLs photon receiving system. In principle, however, the profile comparison at this time step only offers slight validation or falsification potential of the model prediction for an observer or data assimilation system.

In contrary, the profile comparison at 17 April 2010, 04:30 UTC results in near-overlapping vertical profiles of the ACL and BaLiFOp attenuated backscatter coefficient. Both profiles show peaks at the same height (2.1 km) and show similar absolute values of the attenuated backscatter coefficient, namely $5.0 \times 10^{-6}\,\mathrm{m^{-1}\,sr^{-1}}$ (ACL), and $1.0 \times 10^{-5}\,\mathrm{m^{-1}\,sr^{-1}}$ (BaLiFOp), respectively. The model-predicted ash number density at this specific location can be regarded as validated within the range of uncertainties of the forward operator (see section 4) and the ACL system (see section 3).

The full time series of profile-based comparison is shown in Appendix a. Based on the time series, the volcanic ash clouds are observable from the ACL profiles beginning at 16 April, 13:00 UTC in 6 km ASL with increasing visibility from 20:00 UTC until the volcanic ash layers become visible at the profiles from 17 April 2010, 01:00 to 07:00 UTC. Major differences between the measured and forward modeled profiles are due to missing background aerosol types in the model prediction, missing aerosol types in forward operator and other natural and physical effects which are not represented yet by model and forward operator but can have a huge impact on the ACL profiles.

The profile-based comparison, however, offers a relatively precise validation of both the forward operator and the ACL measurement data calibration (see Section 3): The vertical profiles of ACL and the molecule-only vertical profile output by BaLiFOp in near clean-air situations differ by less than 20 %.

5.5 QUANTITATIVE TIME-HEIGHT COMPARISON

A major purpose of the backscatter lidar forward operator is the capability to perform also quantitative comparison of measurement and model output data. Unfortunately, such comparison is of limited validity in this case study due to the unknown ACL calibration as noted in Section 3.2.

Outside the volcanic ash layer, the forward operator returns attenuated backscatter coefficient values of $1 \times 10^{-7} \, m^{-1} \, sr^{-1}$ which is equal to the values of the ACL instrument after calibration. This would be expected as both temperature and pressure are rather precisely determinable and the scattering properties of air are represented by the empirical equations which are used for the forward operator. Thus, the selected calibration factor seems to be valid for this scenario.

Regarding the attenuated backscatter coefficient inside the ash layer, however, the forward operator returns stronger signals as well as a lower transmission behind the ash plume compared to the ACL measurement. The maximum value of the attenuated backscatter coefficient returned by the forward operator (about $6.0 \times 10^{-4} \, m^{-1} \, sr^{-1}$) is 20 times higher than the maximum value reported by the ACL (about $3.0 \times 10^{-5} \, m^{-1} \, sr^{-1}$). Also, the forward modeled attenuated backscatter coefficient shows strong attenuation due to the volcanic ash layer in about 12 km ASL: the attenuated backscatter coefficient is by about factor 10-15 lower than in same heights above clean-air situations. Both findings indicate an over-estimation of the model-predicted volcanic ash number-density. In the case of determining the hazardousness of volcanic ash particles using ash dispersion models, however, an over-estimation of the ash concentration and preferring false alarms over misses are reasonable strategies.

As a demonstration of a simple data assimilation increment, the effect on the attenuated backscatter coefficient was analyzed if the model-predicted ash number densities are being reduced by factors of 10, 20 and 30. Reducing the ash number density by factor 20 (Fig. 5.4), similar maximum values of the attenuated backscatter coefficient are observed inside the ash layer for both the forward operator and the ACL ($5.0 \times 10^{-5} \, m^{-1} \, sr^{-1}$). This reduction of the number density also results in less extinction, and the two-way transmission has a minimum value of 70 % (plot not shown here) which is more realistic than the minimum value observed for the original dataset (8 %, see Fig. 5.1).
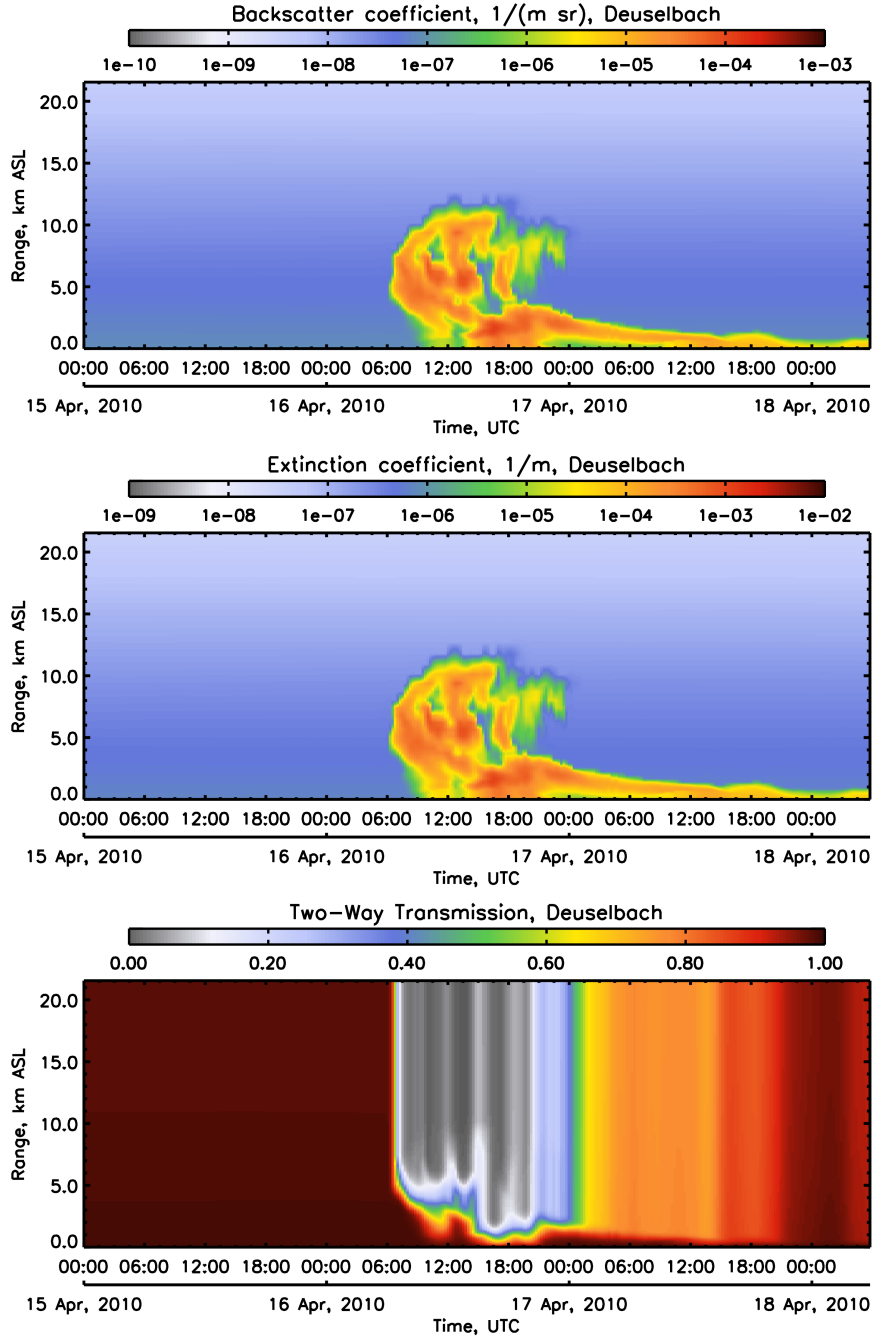
Figure 5.1: Time-height cross section of total backscatter coefficient, extinction coefficient, and two-way transmission, calculated by the forward model based on COSMO-ART output at the station Deuselbach (West Germany). The vertical coordinates are given in km ASL. The forward model used temperature, pressure, and volcanic ash particle data (no clouds, rain, fog, background aerosol or other scattering objects). The backscatter coefficient is by about one order of magnitude lower than the extinction coefficient. The two-way transmission is nearby 1 over clean-air situations. Above ash layers, however, the two-way transmission has a value of only 5 %.
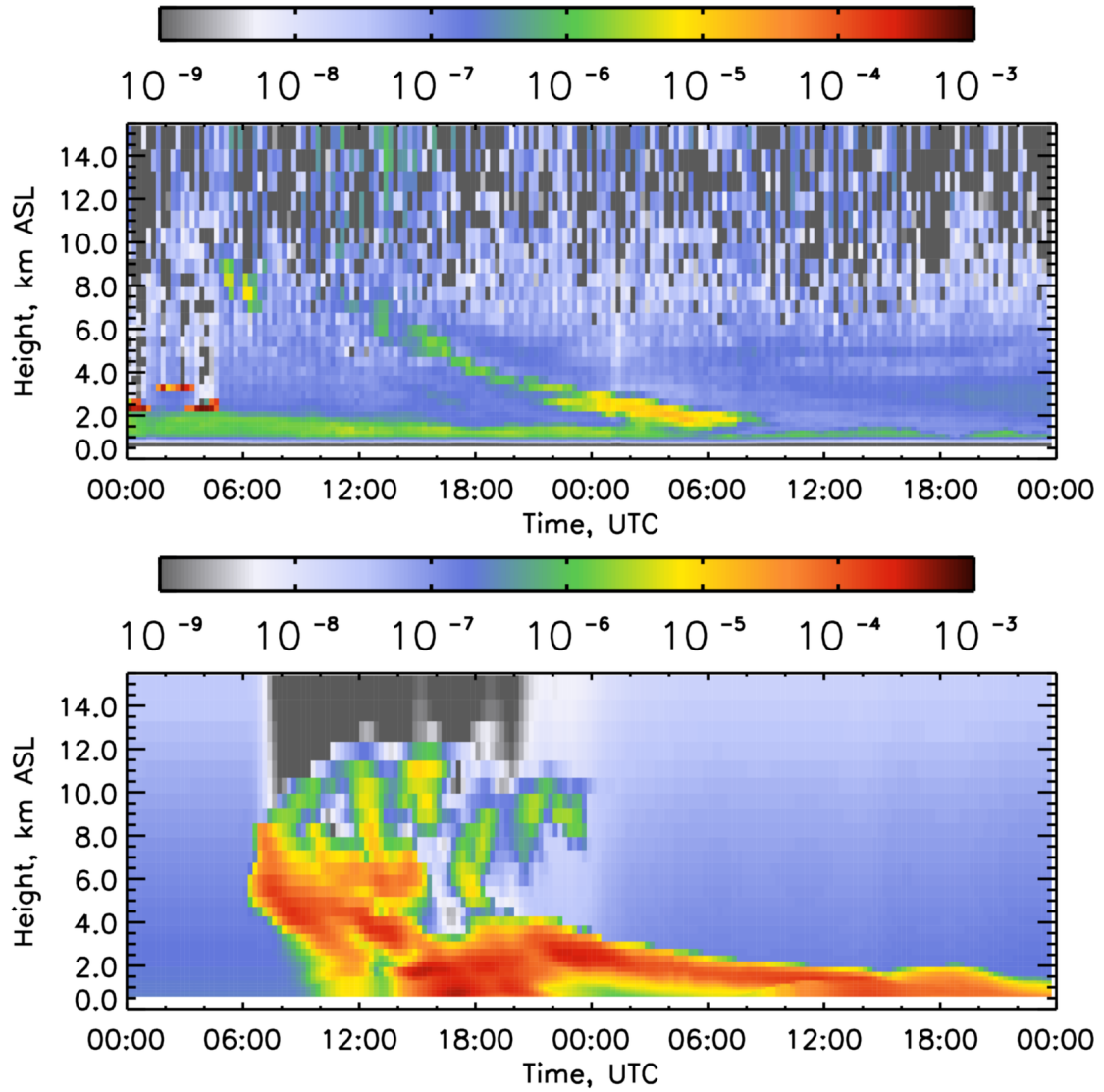
Figure 5.2: Attenuated backscatter coefficient of ceilometer (top) and forward model (bottom) at the station Deuselbach in Germany from 16 April 2010, 00:00 UTC to 17 April 2010, 24:00 UTC. The ACL measurements in heights above 8 km ASL are strongly affected by noise which limits the comparability of both datasets. A comparison of samples near ground is limited by missing overlap correction of ACL data and the lack of background aerosol prediction data. The ash layers in heights between 2 km and 8 km ASL allow for identifying similar and non-similar structures of measurement and forward modeled COSMO-ART predictions of the Eyjafjallajökull ash. The maximum value of the (non-calibrated) ACL measured attenuated backscatter coefficient is by about 1 orders of magnitude lower than the attenuated backscatter coefficient from COSMO-ART prediction with BaLiFOp applied.
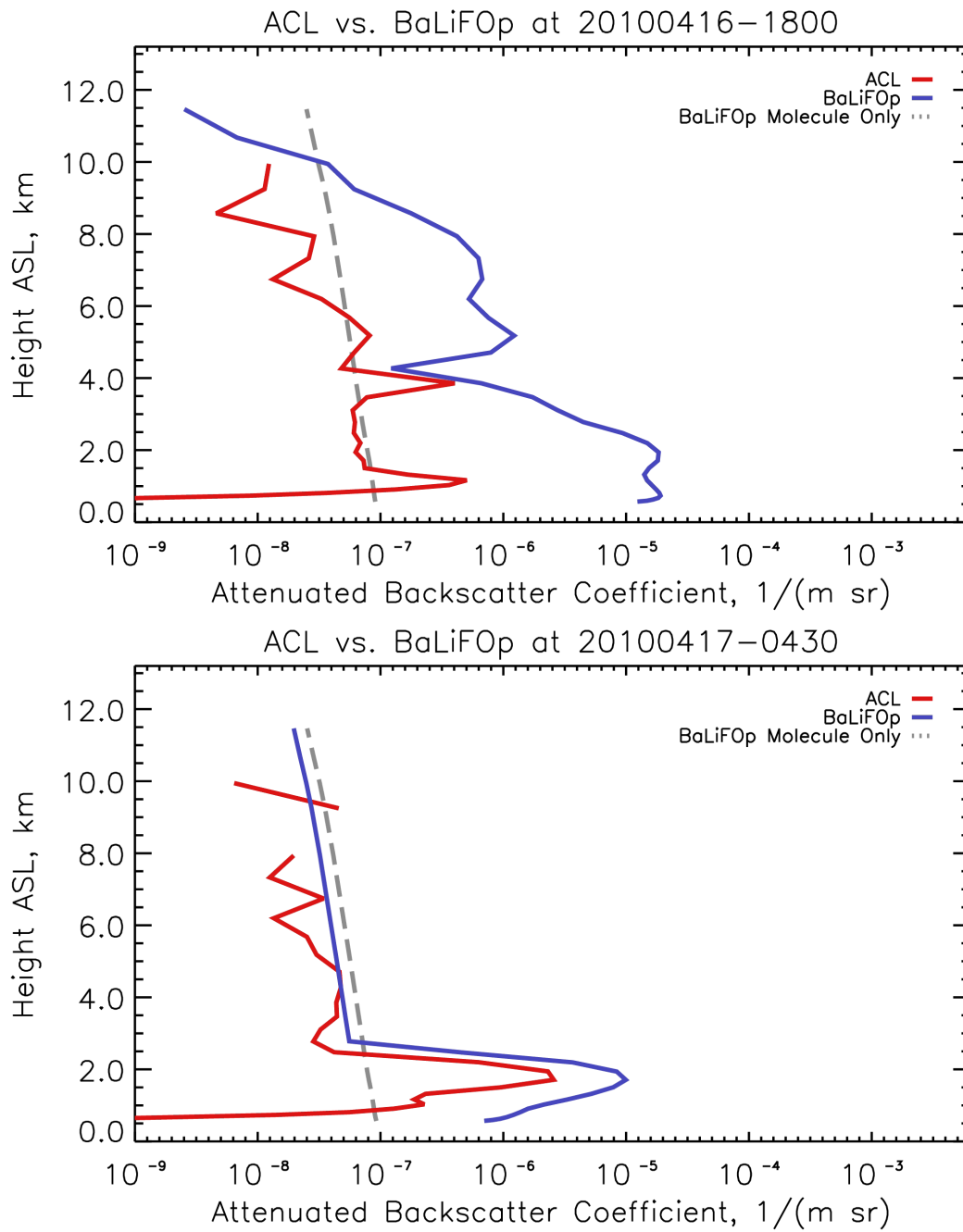
Figure 5.3: Profile based comparison of ACL measured attenuated backscatter coefficient (red line), BaLiFOp total attenuated backscatter coefficient (blue line), and BaLiFOp molecule-only attenuated backscatter coefficient (dashed line) at ACL station Deuselbach, 16 April 2010, 18:00 UTC (top), and 17 April 2010, 04:30 UTC (bottom), respectively.
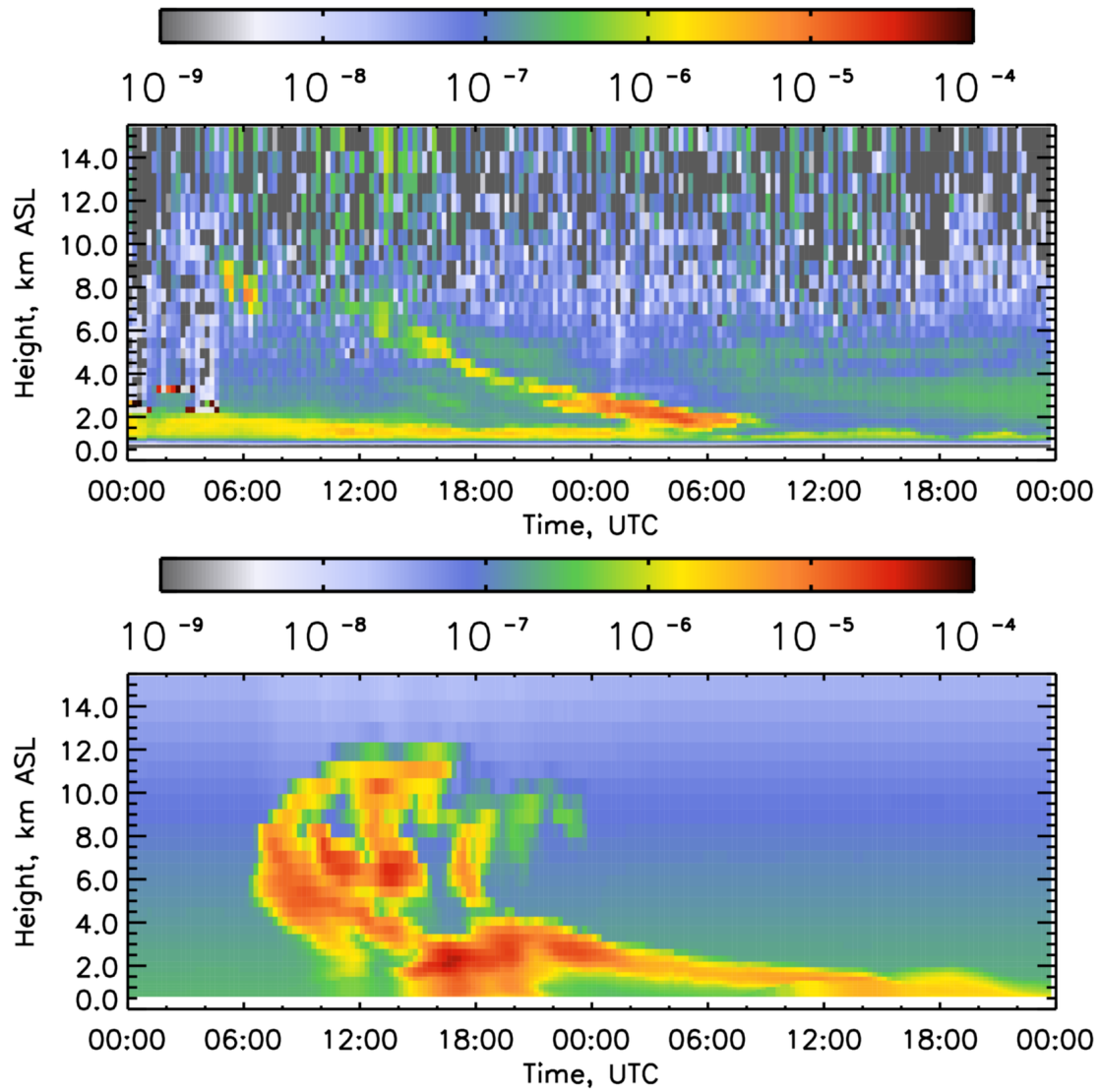
Figure 5.4: The same as Fig. 5.2 with a decreased volcanic ash number density. For this purpose, the ash number density predicted by COSMO-ART was reduced by factor 20 before applying the forward operator.

6 CONCLUSIONS AND SUMMARY

A backscatter lidar model capable of calculating both the extinction and backscatter coefficients was introduced. Detailed studies concerning the scattering properties of particles and molecules were performed. Instead of assuming a lidar ratio for given particles, this forward operator allows for calculating the scattering properties even for mixtures of different particle types. Data of a COSMO-ART ash-dispersion simulation for the Eyjafjallajökull eruption in 2010 was used to run the forward operator and perform both qualitative and quantitative comparison between output of the forward operator and measurement data of an ACL system. A major challenge for setting up the forward operator for a given scenario are scattering calculations, namely the calculation of the effective extinction cross section $\overline{\sigma_{\mathrm{ext},R_d,k,\lambda}}$ and the effective differential backscatter cross section $\overline{\sigma_{\mathrm{bsc},R_d,k,\lambda}}$ of all model-represented particle size and type classes.

The atmospheric gas mixture was treated as a uniform mixture of *atmospheric gas* and empirical scattering formulas were used to calculate its optical cross sections for the ACL laser wavelength. From the model-predicted values of temperature and pressure, the molecule number-density and finally the molecule extinction and backscatter coefficients were calculated.

For particle scattering, the range of particle sizes was selected according to the volcanic ash classes used by COSMO-ART (six monodisperse classes with diameters of 1 µm, 3 µm, 5 µm, 10 µm, 15 µm and 30 µm). The range of considered refractive indices were adapted according to in-situ measurements of Schumann et al. (2011).

Due to uncertain refractive indices and shapes of the volcanic ash, sensitivity studies have been performed to analyze the impact of different particle types and shapes on the effective extinction and backscatter cross section, and the pure lidar ratio. While the extinction cross section was only weakly sensitive to variable refractive indices and particle shapes, the backscatter cross section was strongly sensitive to both. However, the sensitivities reduce significantly, when applying size-averaging algorithms. After averaging, the relative uncertainty of the effective backscatter cross section is up to 280% within the defined range of refractive indices. This study also indicates the dependency of the forward operator on precise information about the particle's refractive index.

From the findings of Rocha-Lima et al. (2014), the average aspect ratio of volcanic ash is known but there is no information about a distribution function of particle shapes and real volcanic ash particles have an infinite variety of particle shapes. In consequence, the spherical shape was used as reference even if the real volcanic ash particles are known to be fractal and complex shaped. Within a particle shape sensitivity study, the impact of the particle shape on extinction and backscatter cross sections

was analyzed for 11 particle shapes (6 types of ellipsoids and 5 types of cylinders). The backscatter cross section spectrum of cylinders was different than the spectrum of ellipsoids and spheres. Sensitivity studies are the basis for stepwise improving the knowledge in scattering calculations related to lidar forward models. More detailed studies of scattering at non-spherical particles are thus mandatory to improve the particle shape representation for the calculation of the effective backscatter cross section.

In literature, measured lidar ratio values for volcanic ash are ranging from 40 sr to values greater than 100 sr (Kokkalis et al., 2013; Mortier et al., 2013). This range of values could be observed within sensitivity studies of the pure lidar ratio (Sect. 4.4). From the studies shown in Sect. 4, the assumption of spherical particles results in a general under-estimation of the lidar ratio except for size classes 1 and 4. Comparing the pure lidar ratio values of the first two size classes with the values reported by Gasteiger et al. (2011b), values of less than 20 sr seem to be plausible for these size parameters. The authors found even for irregularly shaped objects a pure lidar ratio between 5 sr and 20 sr at size parameters between 5 and 15 (equivalent particle diameter at $\lambda = 1064$ nm is 1.6 μm and 4.8 μm, respectively). The pure lidar ratio values output by the forward operator are thus realistic.

The total lidar ratio calculated at two sample coordinates of COSMO-ART output resulted in values of 9.63 sr and 46.53 sr, respectively, which is - for the first coordinate - lower than the lidar ratio values of the Eyjafjallajökull ash plume measured by Raman lidar at Munich and Leipzig. From an analysis of the pure lidar ratio, an under-estimation of the calculated lidar ratio for some size classes could be observed due to the assumption of spherical volcanic ash particles. However, the particle size class configuration of the model could also have a huge effect on the calculated lidar ratio values due to the ash size coverage and ash size class width configuration. Therefore, the forward modeled total lidar ratio in this scenario is not expected to match the lidar ratio derived from measurements exactly. Further investigation in this topic is required to optimize the particle size class configuration of models using monodisperse size classes and the representation of non spherical particles in the forward operator towards a better representation of the total lidar ratio.

A time-height cross section comparison of ACL measurement and forward modeled COSMO-ART output was shown. Similar structures were observed but some features were referenced to different times and heights. From the analysis at the ACL station Deuselbach, some ash layer features were predicted quite precisely by the model, for example the time of arrival of the ash plume at about 06:00 UTC, but the layer prediction was vertically shifted by about 1.5 km. The ash plume intersection with the planetary boundary layer at 17 April 2010, 03:00 UTC was simulated about 6 hours too early at 16 April 2010, 18:00 UTC. Fine structures of the ash layer were only observable in the simulation but not in the ACL data due to noise. Furthermore, the contribution of individual classes to the total backscatter coefficient and to the total mass density for two sample cases were analyzed.

The missing calibration coefficients of the ACL system required to define a calibration constant η^* and estimate its value comparing the ACL data with calibrated measurements at the same wavelength. Within quantitative comparisons between ACL measurements and the forward operator output, the molecule signal of ACL and forward operator output were in the same order of magnitude which argues that the selected calibration factor was reasonable.

A comparison of the measured and forward modeled volcanic ash attenuated backscatter coefficient inside the volcanic ash plume led to the conclusion that the model predicted ash concentration was too high which could be potentially resolved by reducing the model-predicted ash concentration manually by a given factor until the forward modeled COSMO-ART predictions and ACL measurements are quantitatively similar. Such a reduction could be part of a simple particle data assimilation system helping to calibrate particle dispersion simulations before in-situ measurements are available - assuming that the particles optical properties are known. It is therefore required to develop methods in the future which allow for a fast determination of an aerosol type's refractive index range, shape- and aspect ratio description.

As aerosol dispersion processes are directly coupled to vertical and horizontal movements in the atmosphere, a comparison of forward modeled and measured backscatter lidar profiles offers great potential for validating and improving the dynamic and thermodynamic components of an atmospheric chemistry model. For a model with variational data assimilation methods, the data assimilation system would select the prediction variation which fits best to the atmospheric state provided by lidar measurements, resulting in a continuous adaptation of the model prediction to the real world situation.

The absolute values reported by the Raman lidar systems at a wavelength of 1064 nm, however, agreed within the measurement uncertainties and expected natural differences in the sampled air mass with the results of the forward operator, see Sect. 5.5. This is quite remarkable given the large uncertainties of the ash data in the model (assumed emission rate of the volcano, atmospheric dynamics, dynamic of the modeled ash plume in the atmosphere including sedimentation), and that there is no data assimilation regarding aerosol data at all yet. Further studies could focus on comparison between forward modeled lidar profiles and measurements from Raman or multi-wavelength lidar. In this context also the upcoming European Space Agency (ESA) satellite sensor Earth Clouds, Aerosols and Radiation Explorer (EarthCARE) with its high-spectral resolution lidar is certainly of high interest.

There are, however, some error sources remaining which are: First, there are only molecules and the six volcanic ash classes represented while background aerosol is missing completely. Second, the ACL calibration is of limited precision. Third, the contribution to the attenuated backscatter coefficient of ash size classes 4, 5 and 6 is relatively low even though these classes carry a large proportion of the mass. This relationship could rely on the ACL's wavelength which probably limits its sensitivity

to particles larger than $10\,\mu m$ in diameter. Such results strengthen the importance of a joint use of observations and model output in combination with data assimilation in order to get a reliable description of the atmospheric state with respect to aerosol distributions and properties.

7 OUTLOOK

Further investigation in scattering calculations of non-spherical particles is recommended to get more realistic optical cross sections for the forward operator. A decrease of uncertainties related to the forward operator can be achieved by refractive index measurements at the exact ACL wavelength. Refractive index measurements are a basic aspect of the forward operator as the optical cross sections can only be calculated if the aerosols' refractive index is known precisely. The model - and consequently the forward operator - must represent more aerosol types, especially background aerosols, mineral dust, sea salt and soot as missing extinction near ground may cause the forward operator to overestimate the attenuated backscatter coefficient value from layers behind. But also qualitatively, more scatterer size classes are required to reliably represent the fine fraction and very large particles in the atmosphere. One approach for a better representation of the natural size-spectrum of aerosols is the use of continuous number-size distributions which are aggregated from multiple distribution functions ("modal" approach). On the one hand, this already includes the size-averaging which is necessary for monodisperse size distributions. But on the other hand, the model delivers exact information about the outer margins, i.e. the number-density of the fine and the extreme coarse fraction which is currently not reproduced by model and forward operator in the selected case study.

As many ACL devices are operating a proprietary firmware, the manufacturers have to be sensitized to data quality and reproducible measurement calibration. Therefore, it is required that calibration is performed automatically and transparent. In future lidar measurement networks, the number of HSRL systems and Raman lidar systems could potentially increase and allow for the assimilation of extinction coefficient and backscatter coefficient directly. But also for present automated lidar systems, activities are ongoing to collect, homogenize, and distribute observations in an international framework. Observation projects such as EARLINET (Pappalardo et al., 2014) and EUMETNET Profiling Programme (E-PROFILE) also focus on data quality improvements to meet the requirements of Numerical Weather Prediction (NWP). In the spirit of these international activities, the creation of a central database for aerosol scattering properties and forward operators would be desirable. Such databases could help to increase the development rate, flexibility and applicability of current and future lidar forward operator implementations. The backscatter lidar forward operator approach presented here is the basis for other, more sophisticated operators and probably the best for backscatter lidar. The methodology and analysis applied in this work will be helpful for stepwise improving our knowledge in how to deal with the the important task of aerosol monitoring, modeling, and data assimilation in the future. The

uncertainties in both modeling and measurements will require sophisticated data assimilation algorithms not only for typical atmospheric variables but also for aerosol optical properties. Also a very good first guess of model simulations with respect to aerosol particles will be necessary to include more sources, types, and sinks in the model data. DWD aims to test the assimilation of ACL data into the COSMO-ART model based on BaLiFOp.

a APPENDIX A - PROFILE-BASED COMPARISON OF ACL AND BALIFOP

In the following, the full time-series of ACL measured attenuated backscatter coefficient (red line), BaLiFOp total attenuated backscatter coefficient (blue line), and BaLiFOp molecule-only attenuated backscatter coefficient (dashed line) profiles at the ACL station Deuselbach from 16 April 2010, 12:00 UTC to 17 April 2017, 14:45 UTC are shown (6 plots per page). A description of the profile-based comparison is Sect. 5.4.
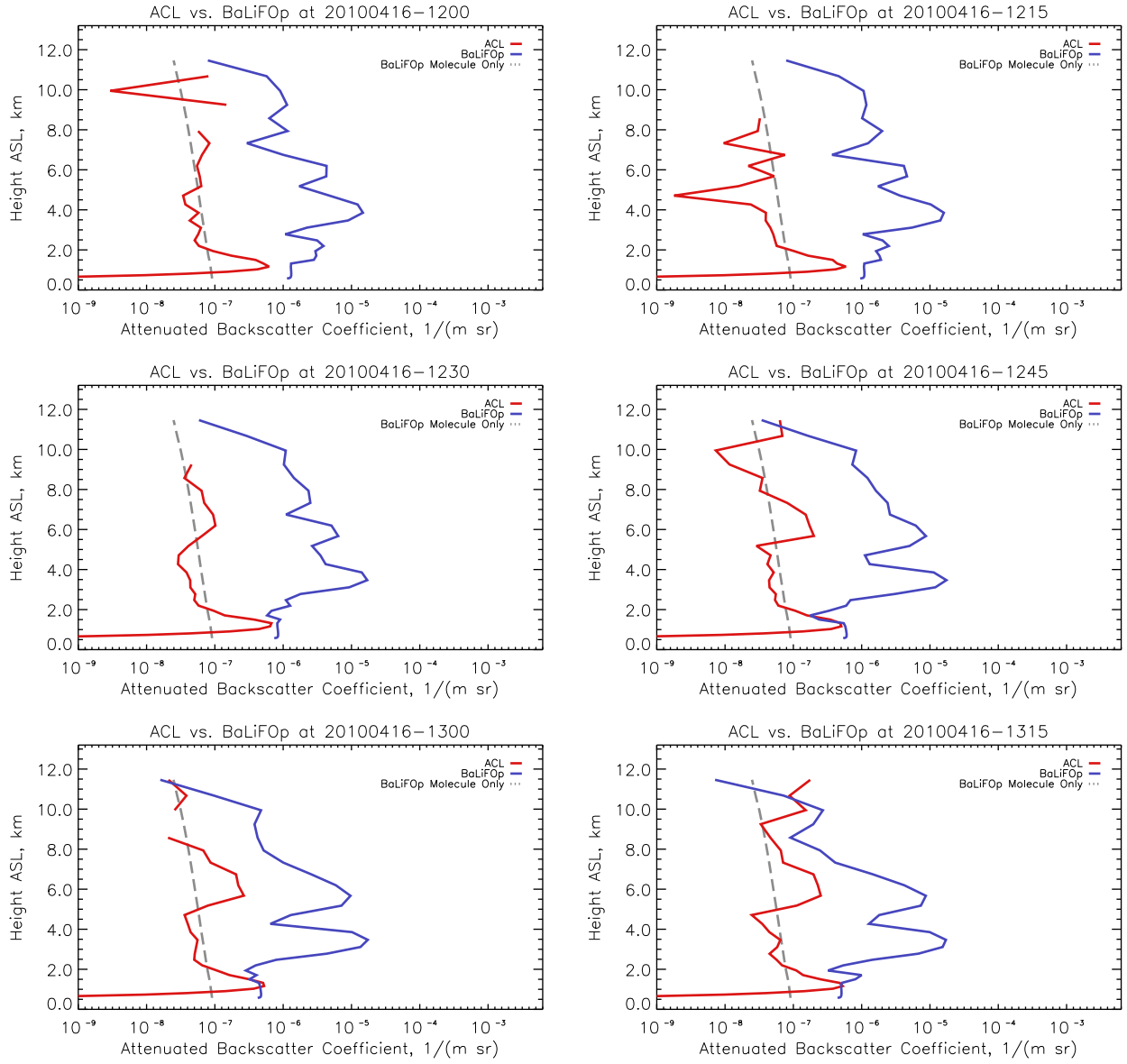
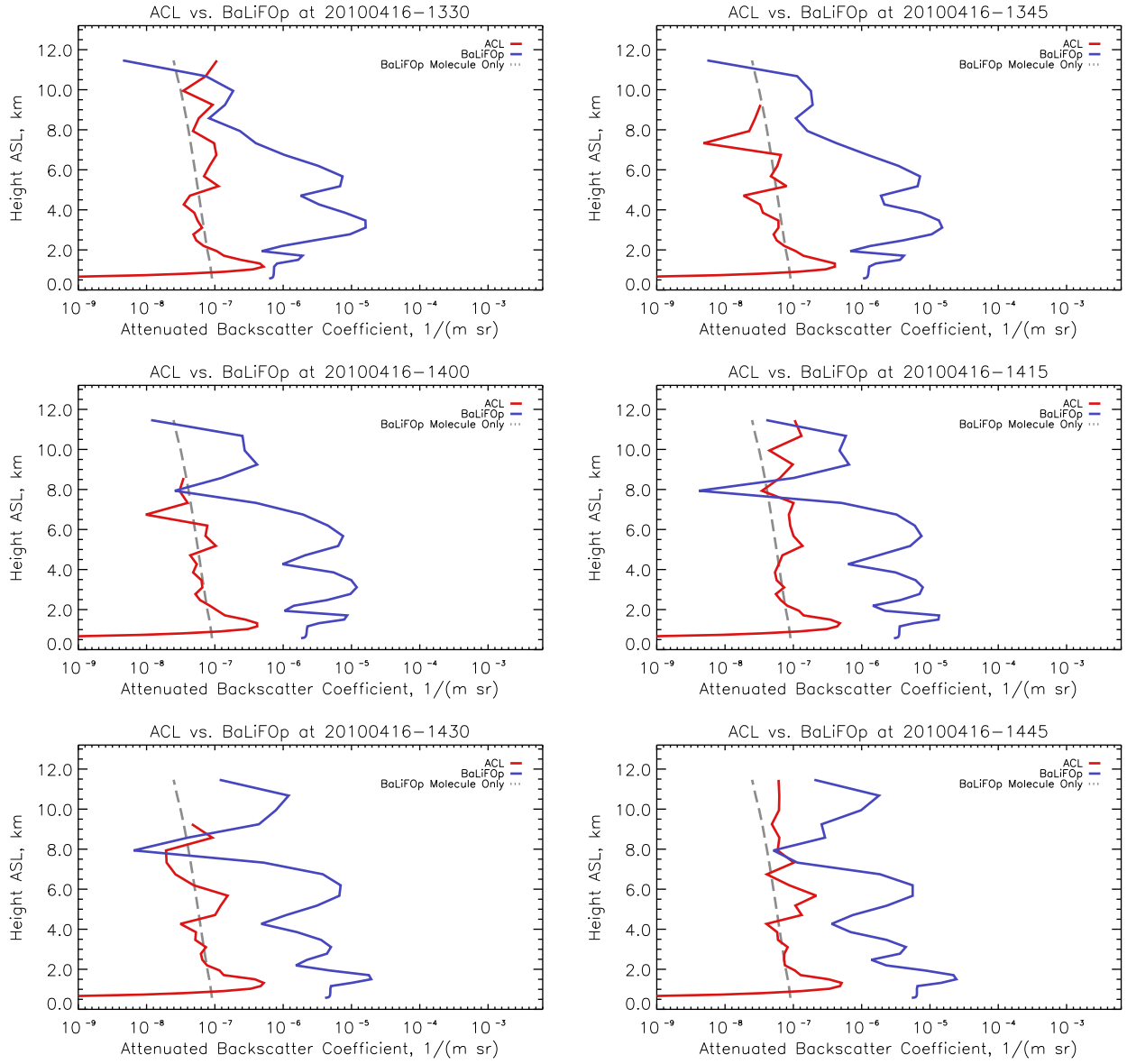Figure a.1: Vertical profiles from 16 April 2010, 12:00 UTC to 13:15 UTC.

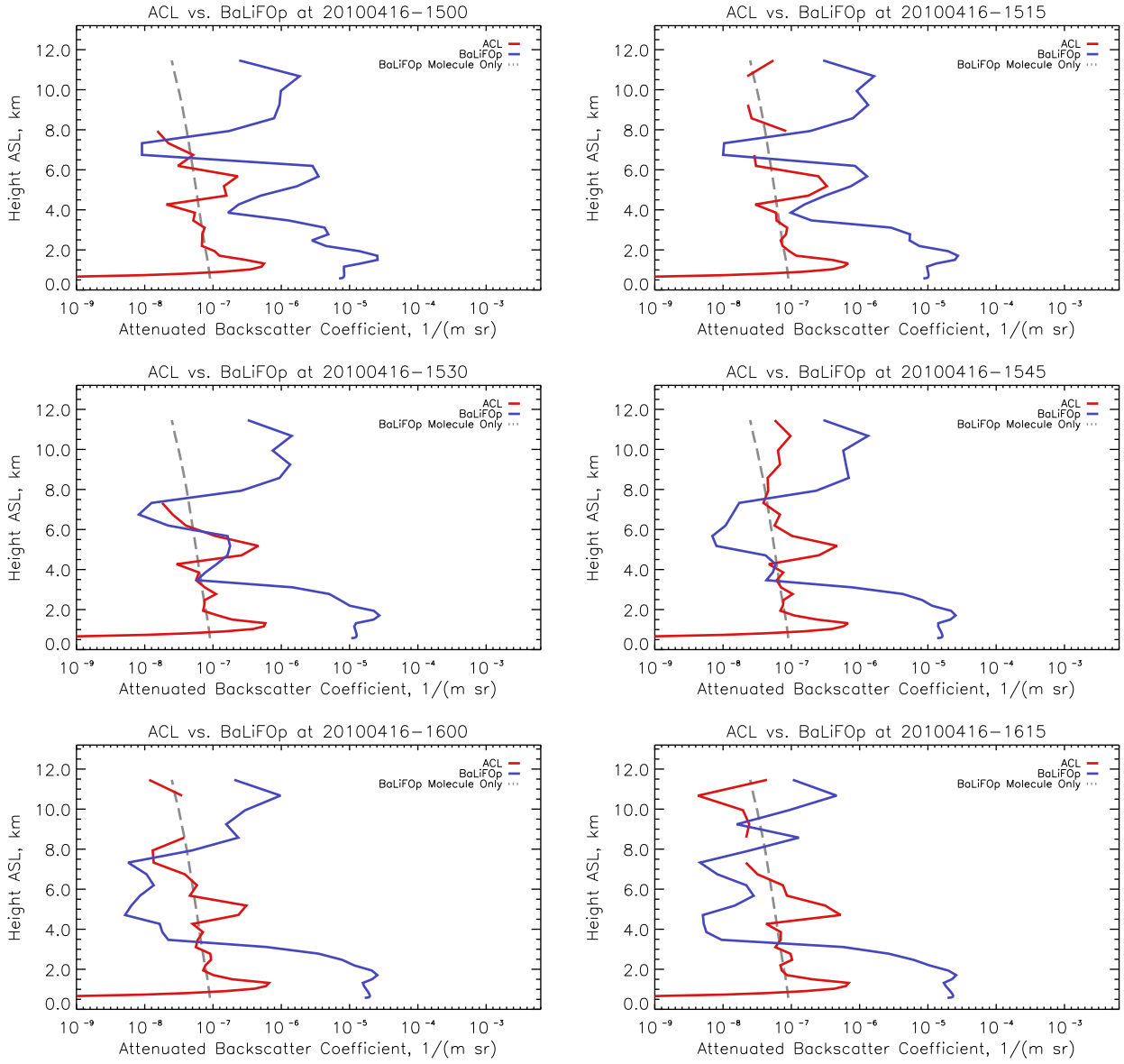Figure a.2: Vertical profiles from 16 April 2010, 13:30 to 14:45 UTC.

Figure a.3: Vertical profiles from 16 April 2010, 15:00 to 16:15 UTC.
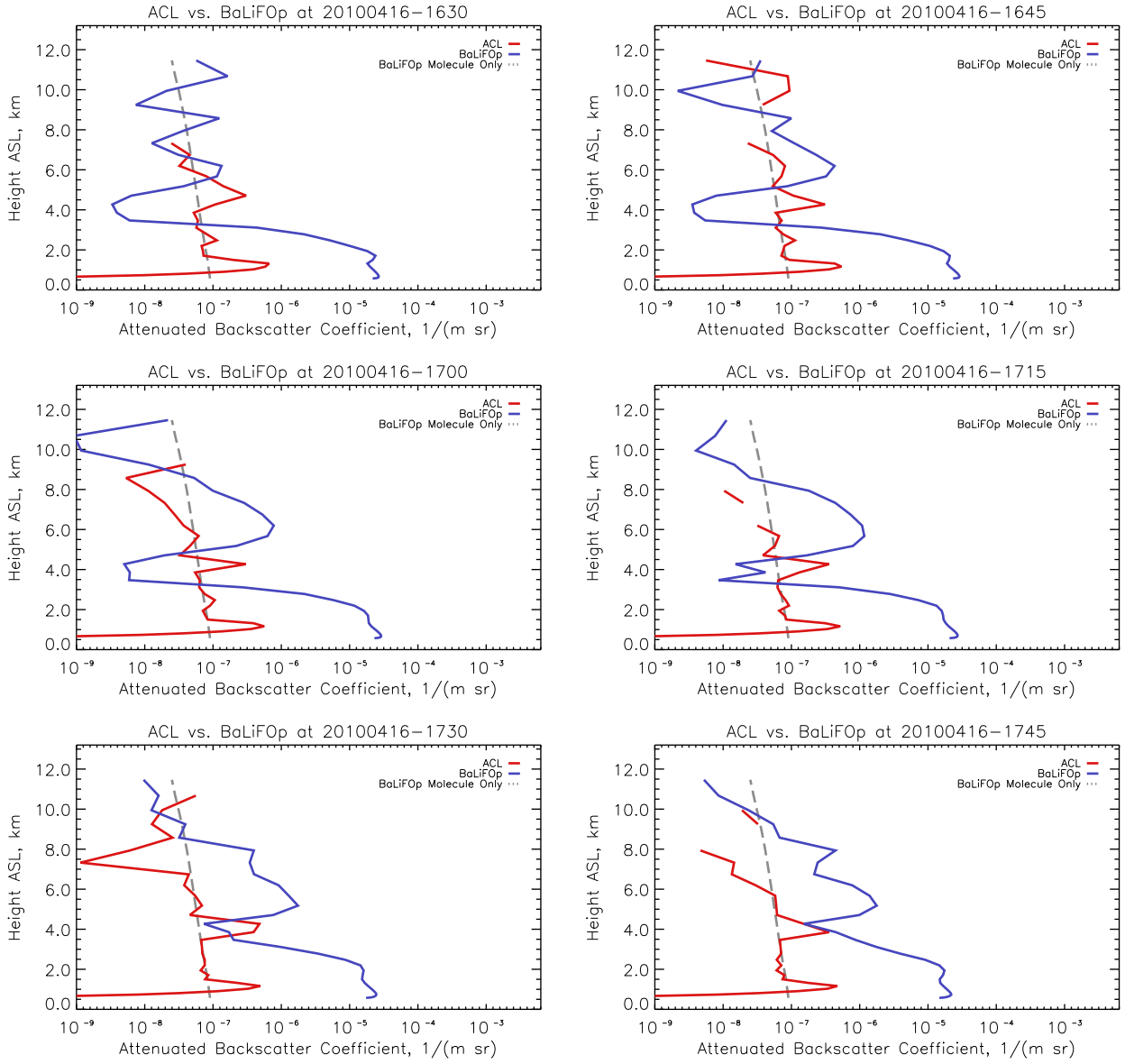
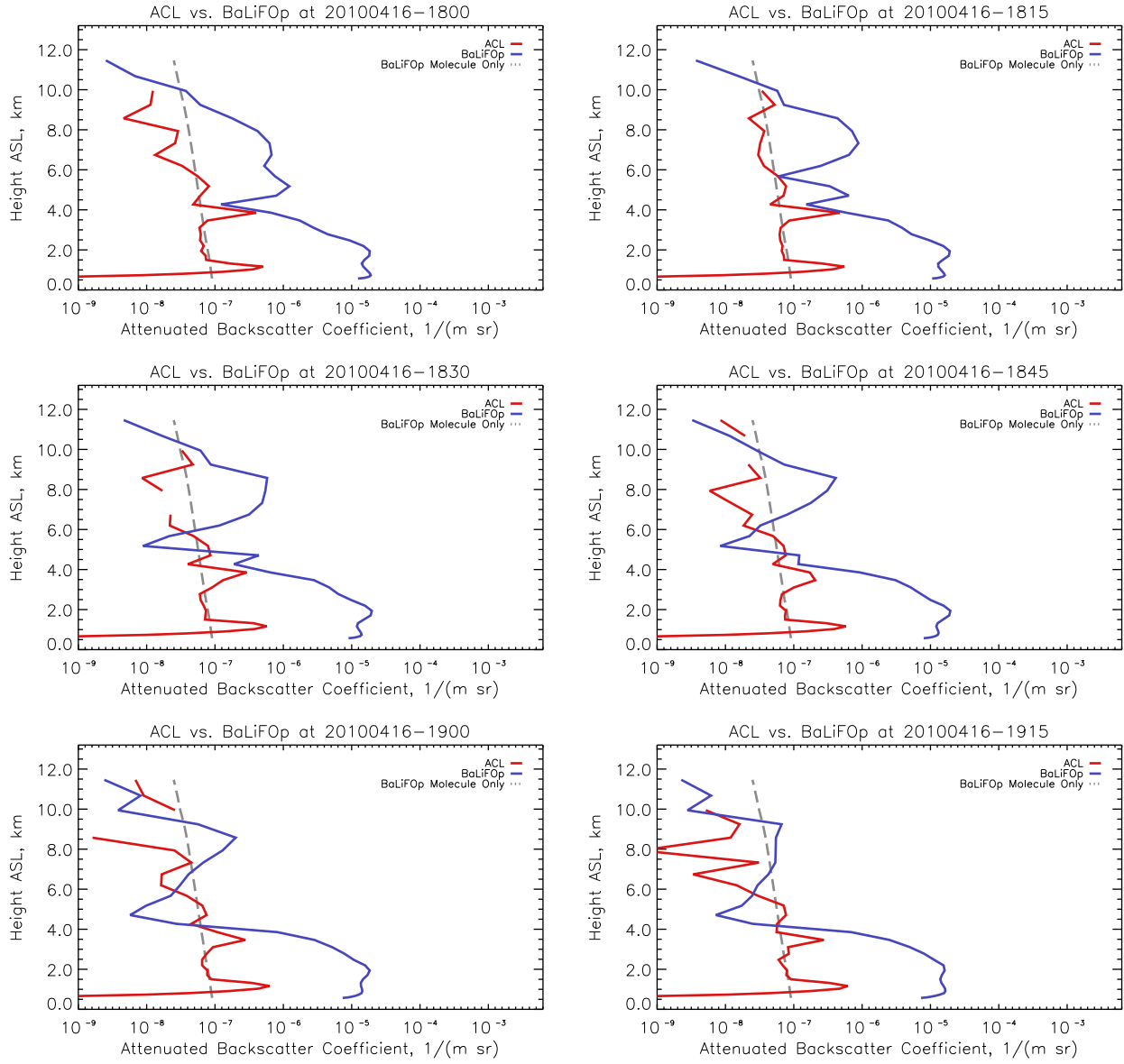Figure a.4: Vertical profiles from 16 April 2010, 16:30 to 17:45 UTC.

Figure a.5: Vertical profiles from 16 April 2010, 18:00 to 19:15 UTC.

Figure a.6: Vertical profiles from 16 April 2010, 19:30 to 20:45 UTC.

Figure a.7: Vertical profiles from 16 April 2010, 21:00 to 22:15 UTC.

Figure a.8: Vertical profiles from 16 April 2010, 22:30 to 23:45 UTC.

Figure a.9: Vertical profiles from 17 April 2010, 00:00 to 01:15 UTC.

Figure a.10: Vertical profiles from 17 April 2010, 01:30 to 02:45 UTC.

Figure a.11: Vertical profiles from 17 April 2010, 03:00 to 04:15 UTC.

Figure a.12: Vertical profiles from 17 April 2010, 04:30 to 05:45 UTC.

Figure a.13: Vertical profiles from 17 April 2010, 06:00 to 07:15 UTC.

Figure a.14: Vertical profiles from 17 April 2010, 07:30 to 08:45 UTC.

Figure a.15: Vertical profiles from 17 April 2010, 09:00 to 10:15 UTC.

Figure a.16: Vertical profiles from 17 April 2010, 10:30 to 11:45 UTC.

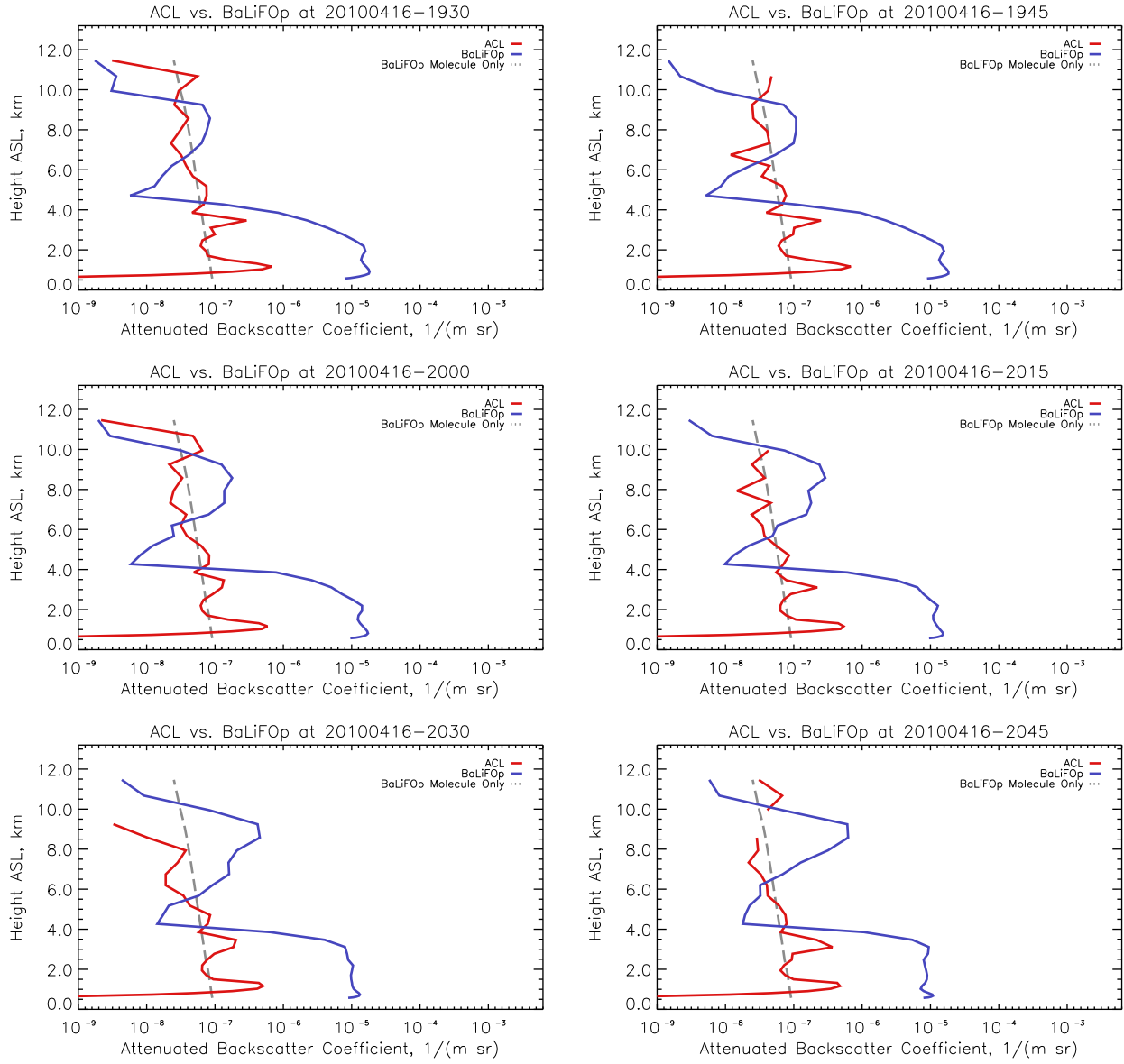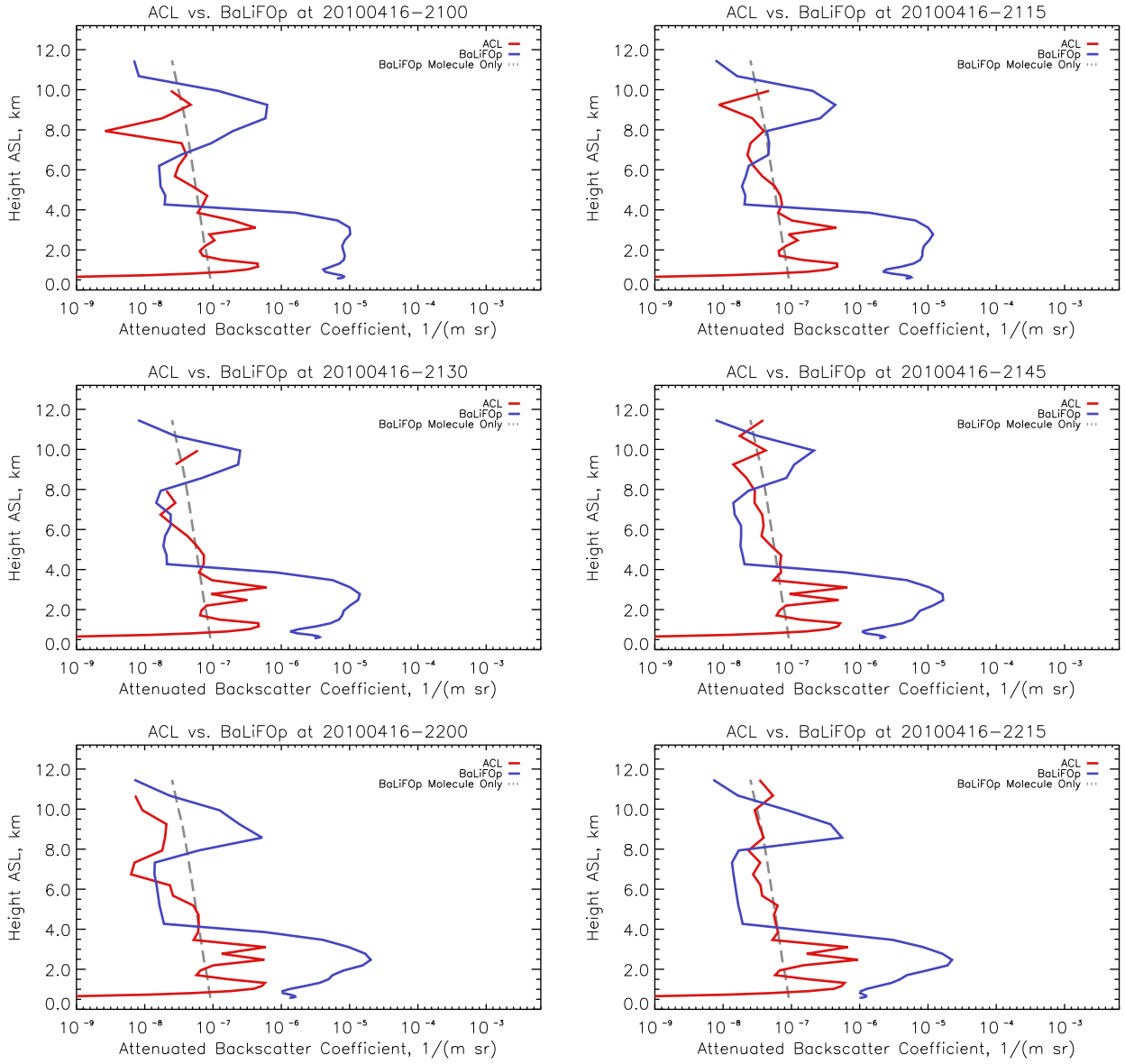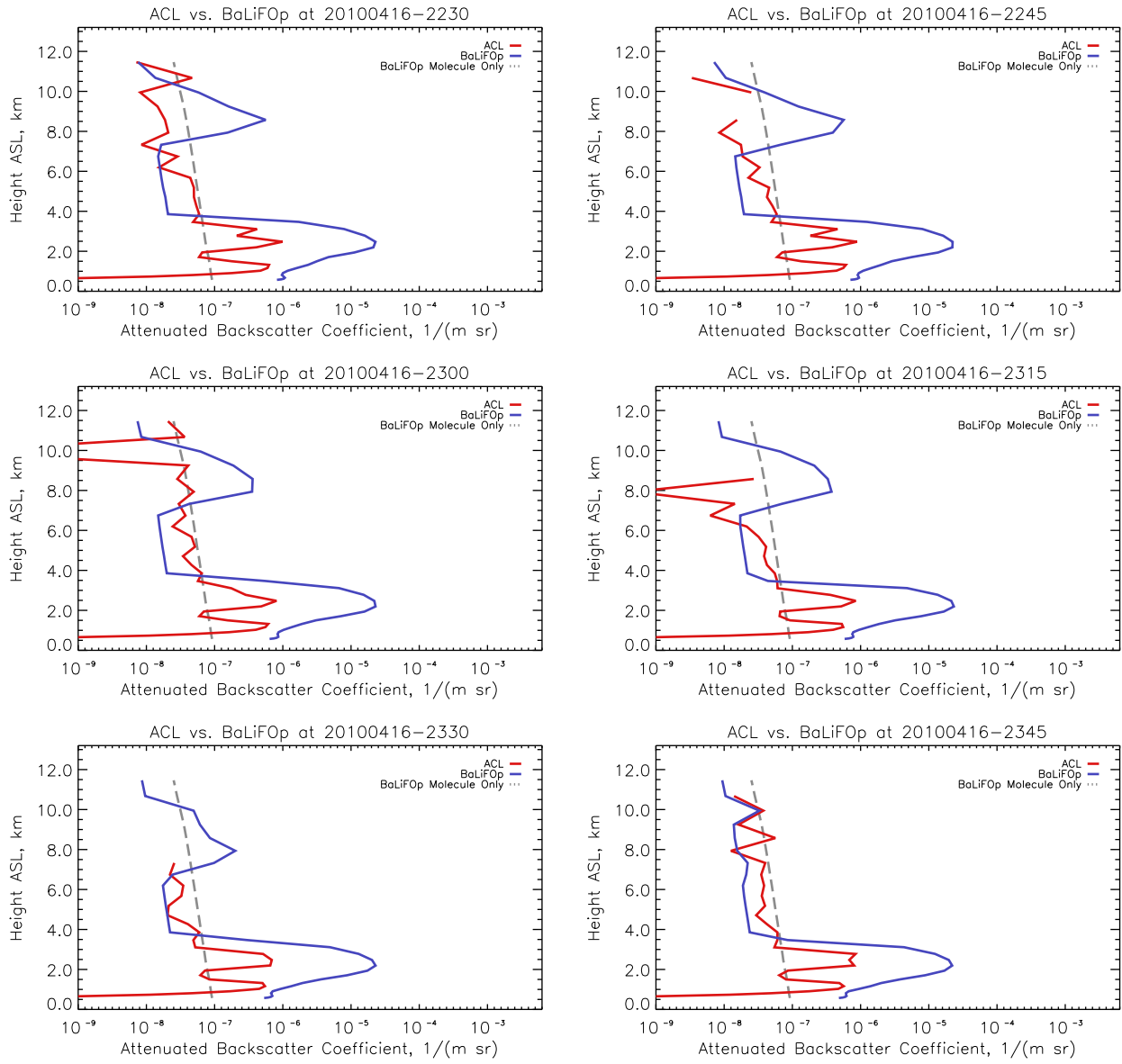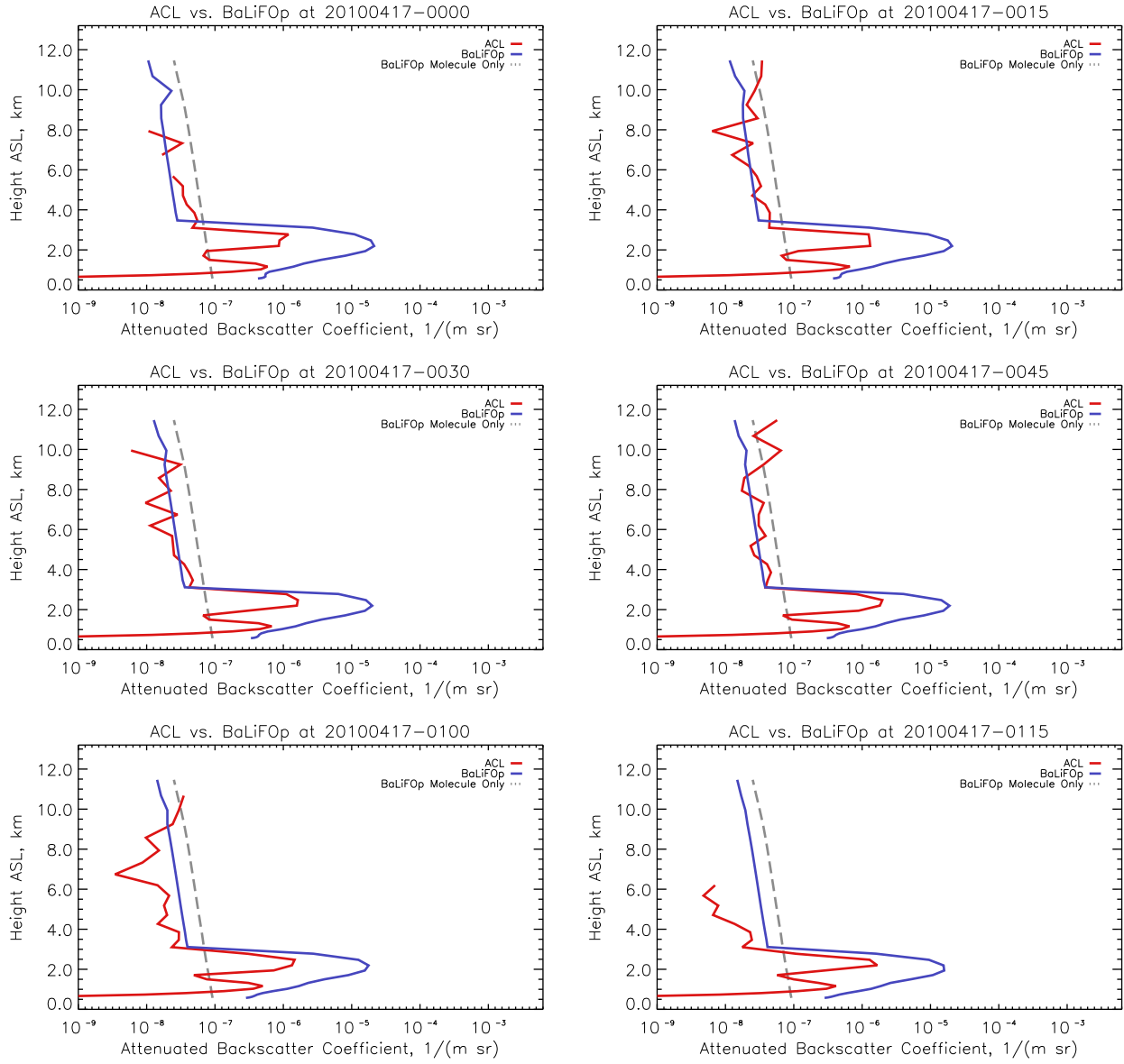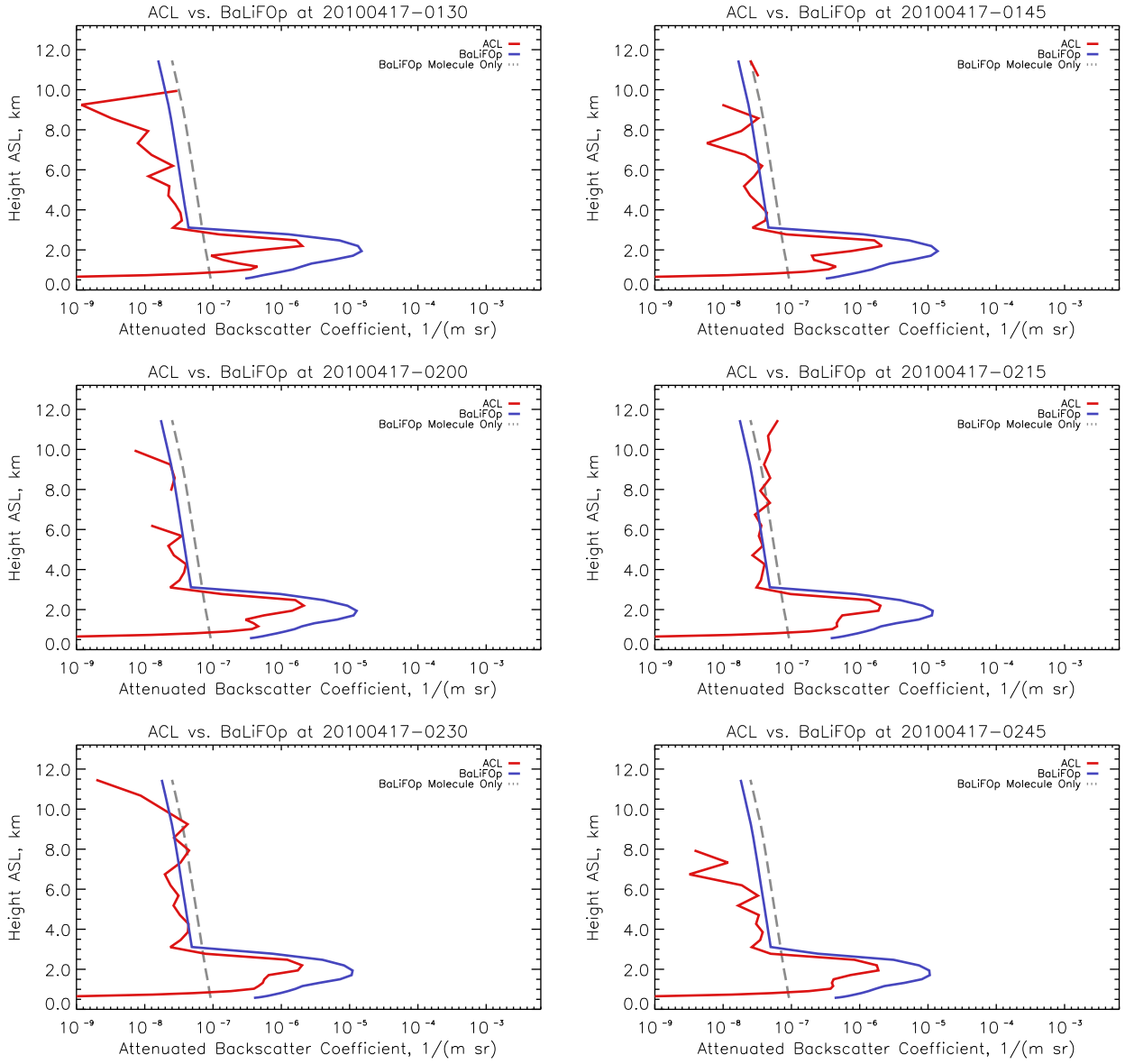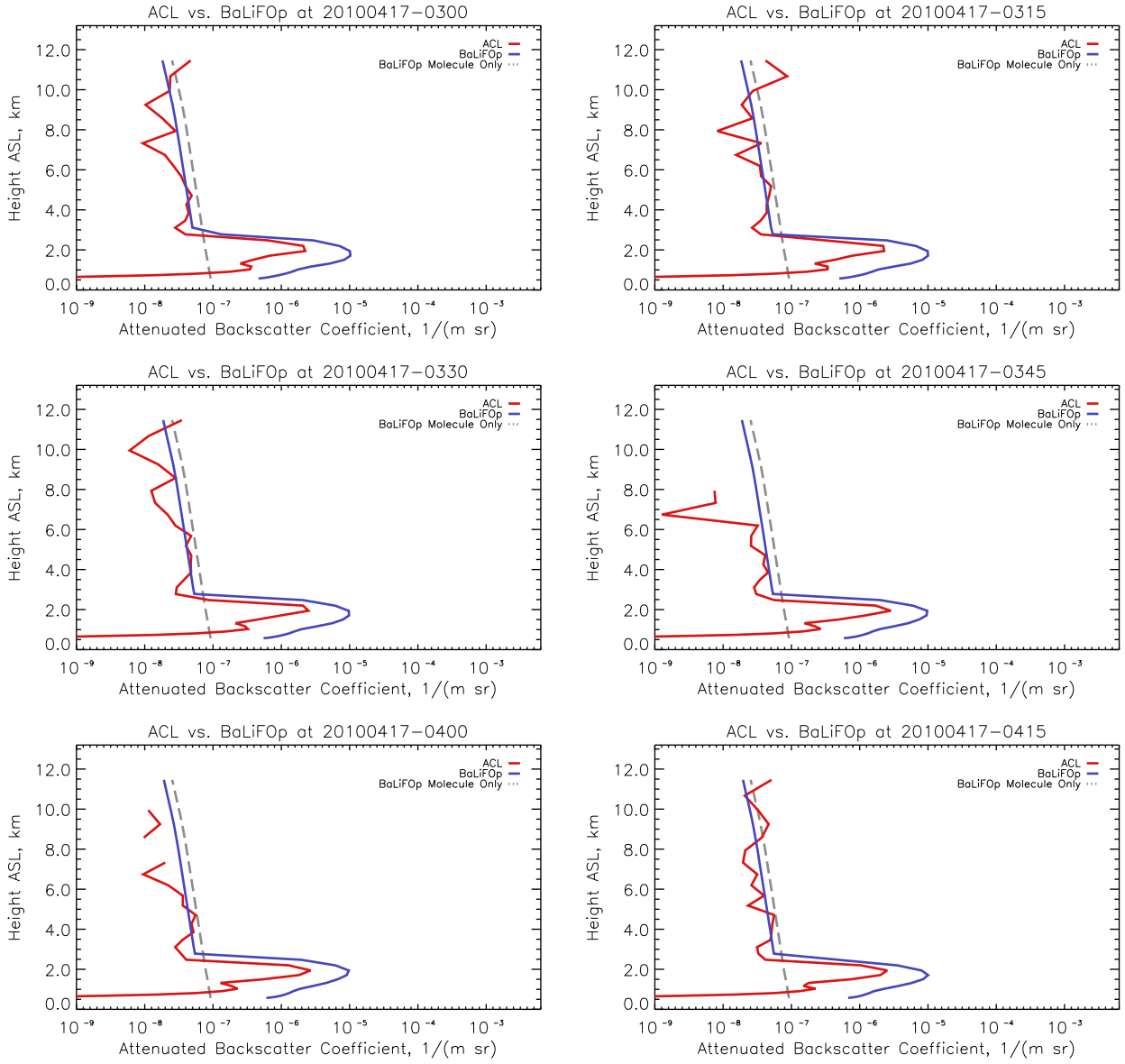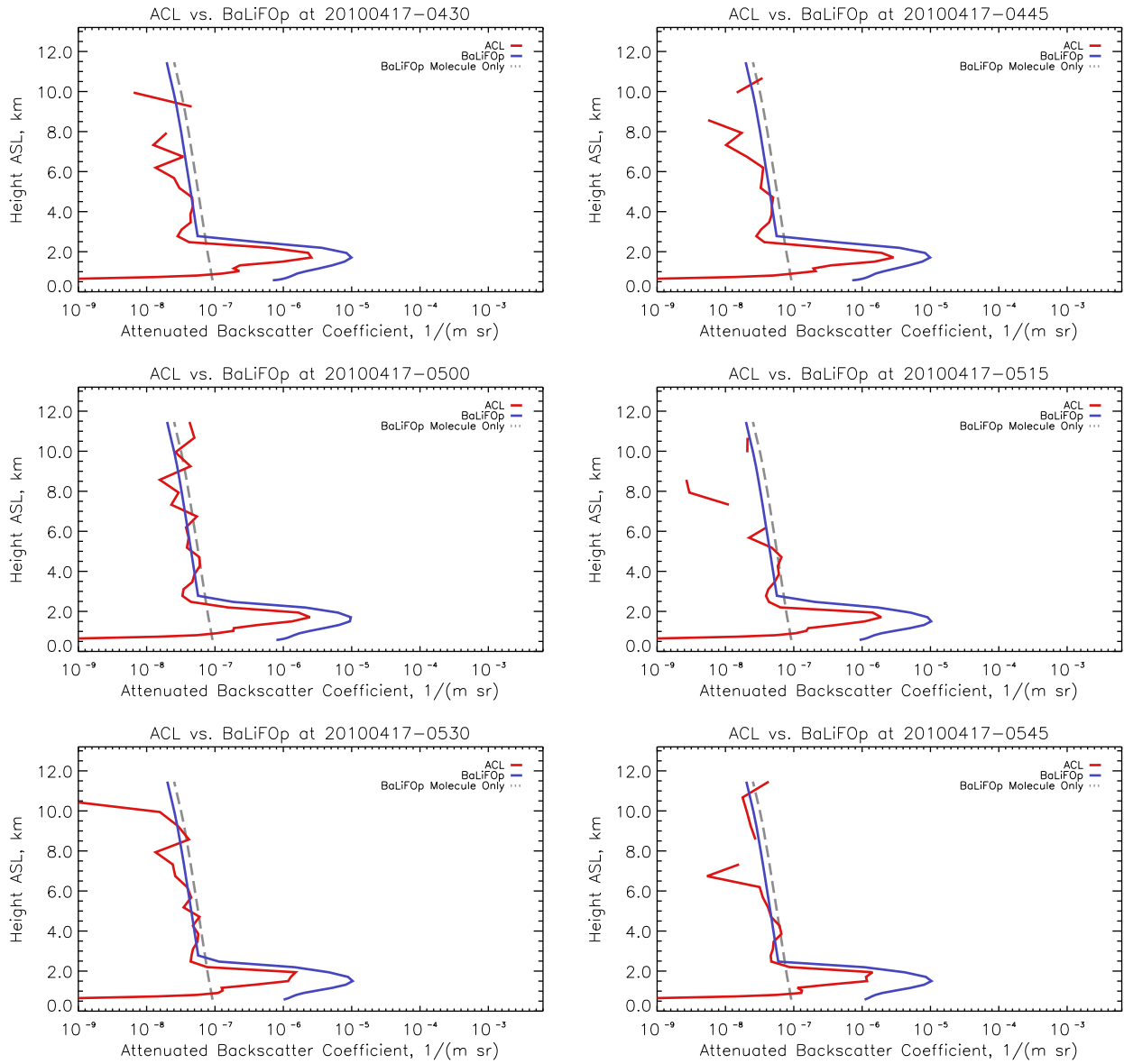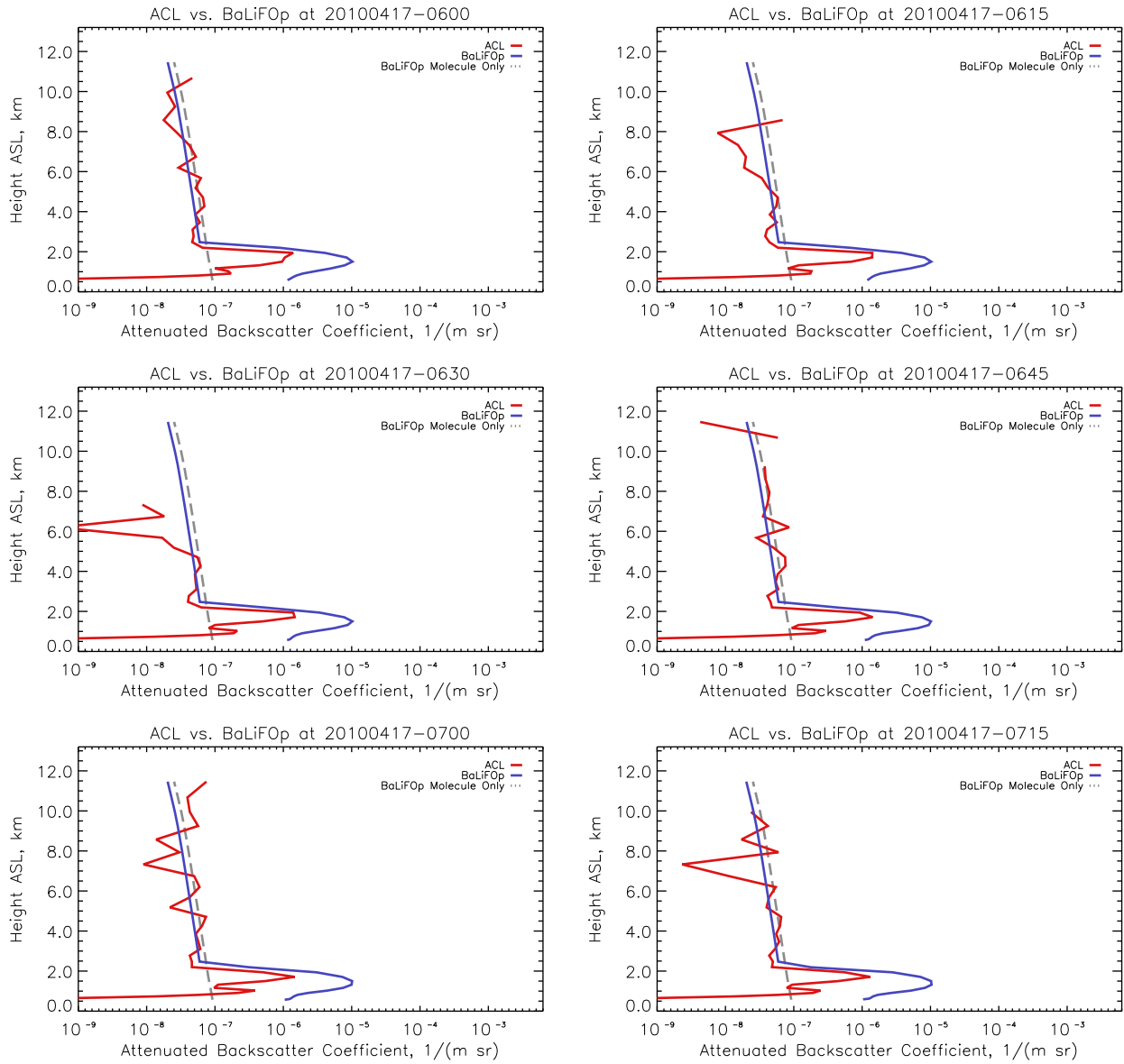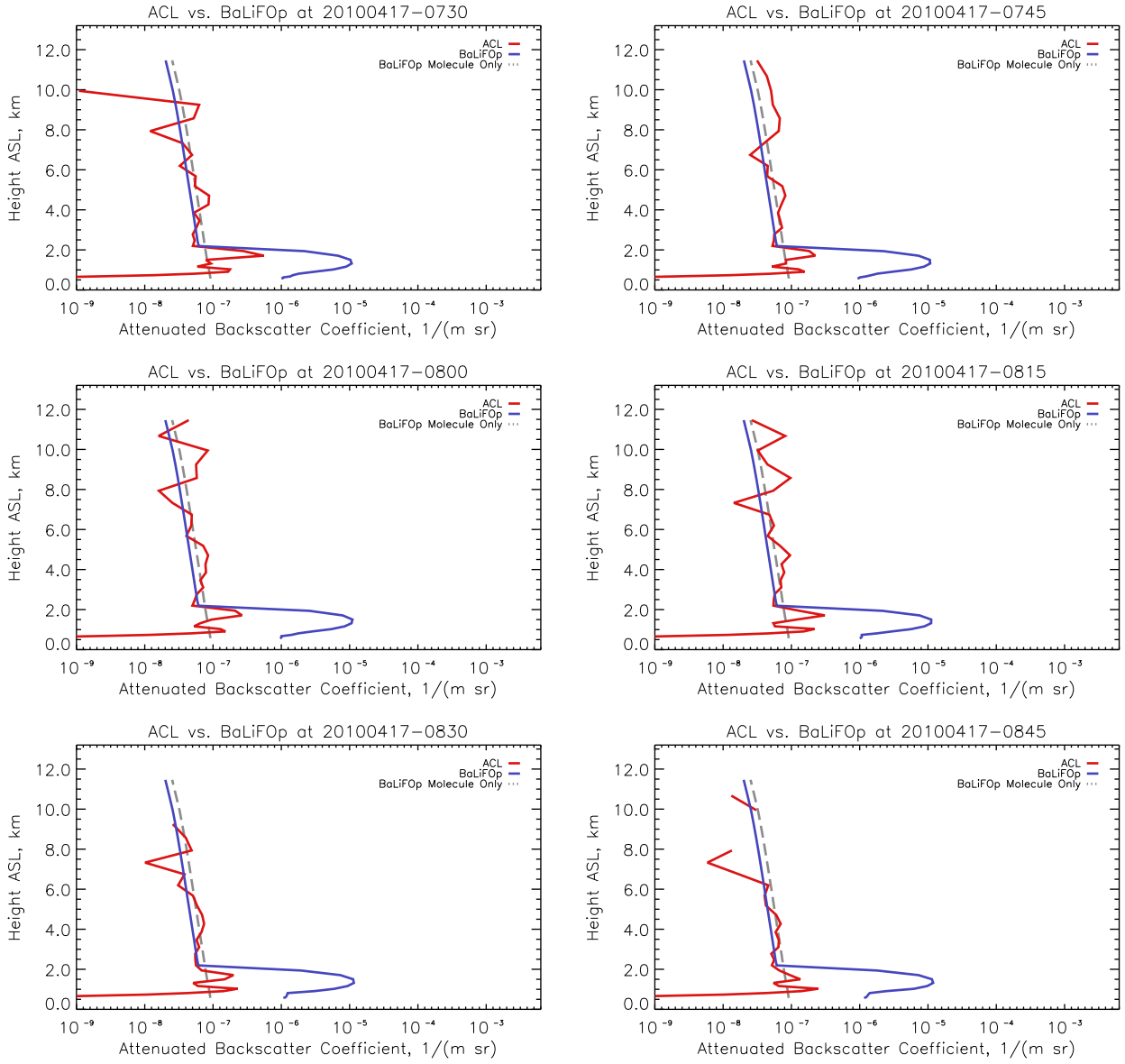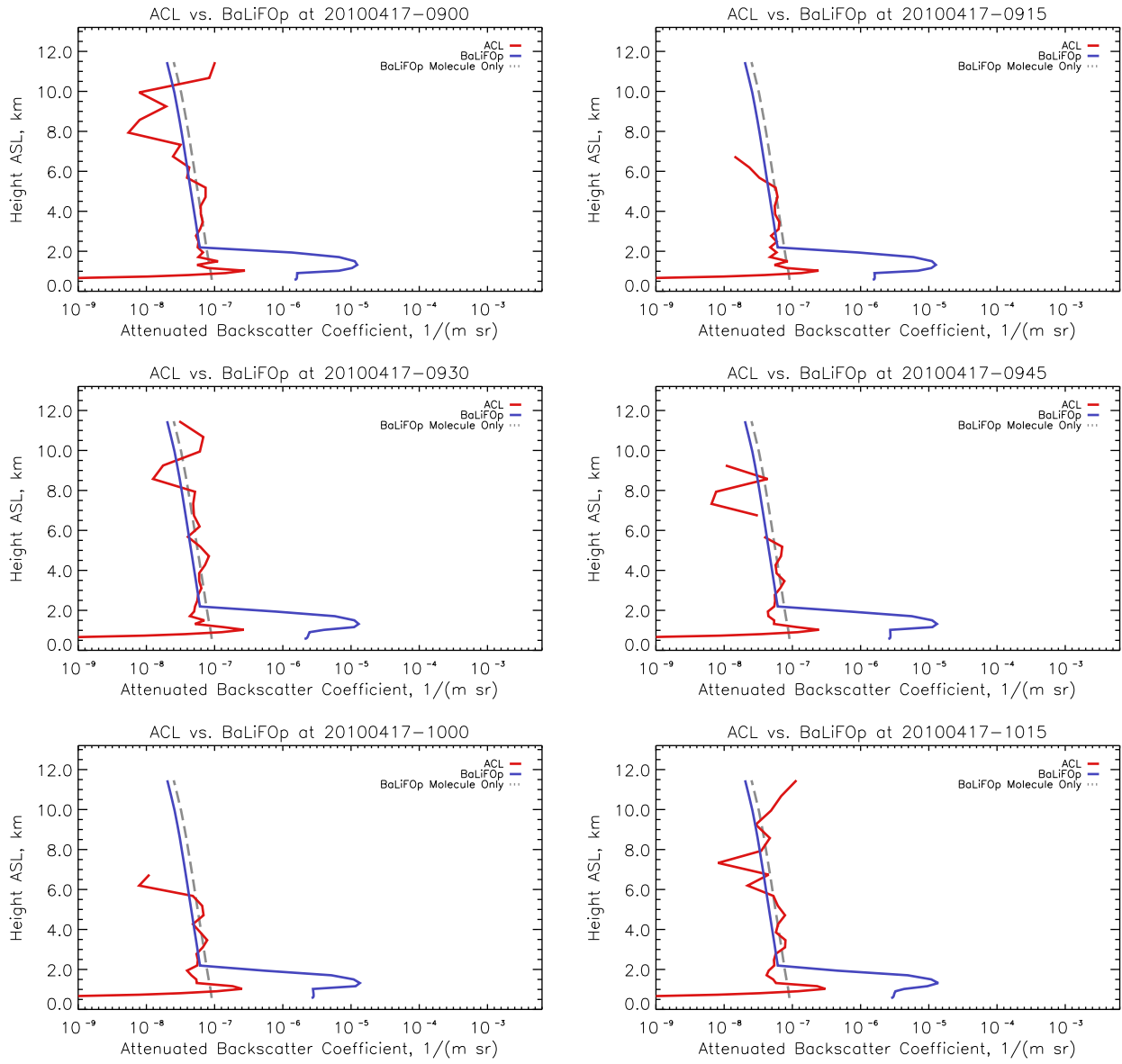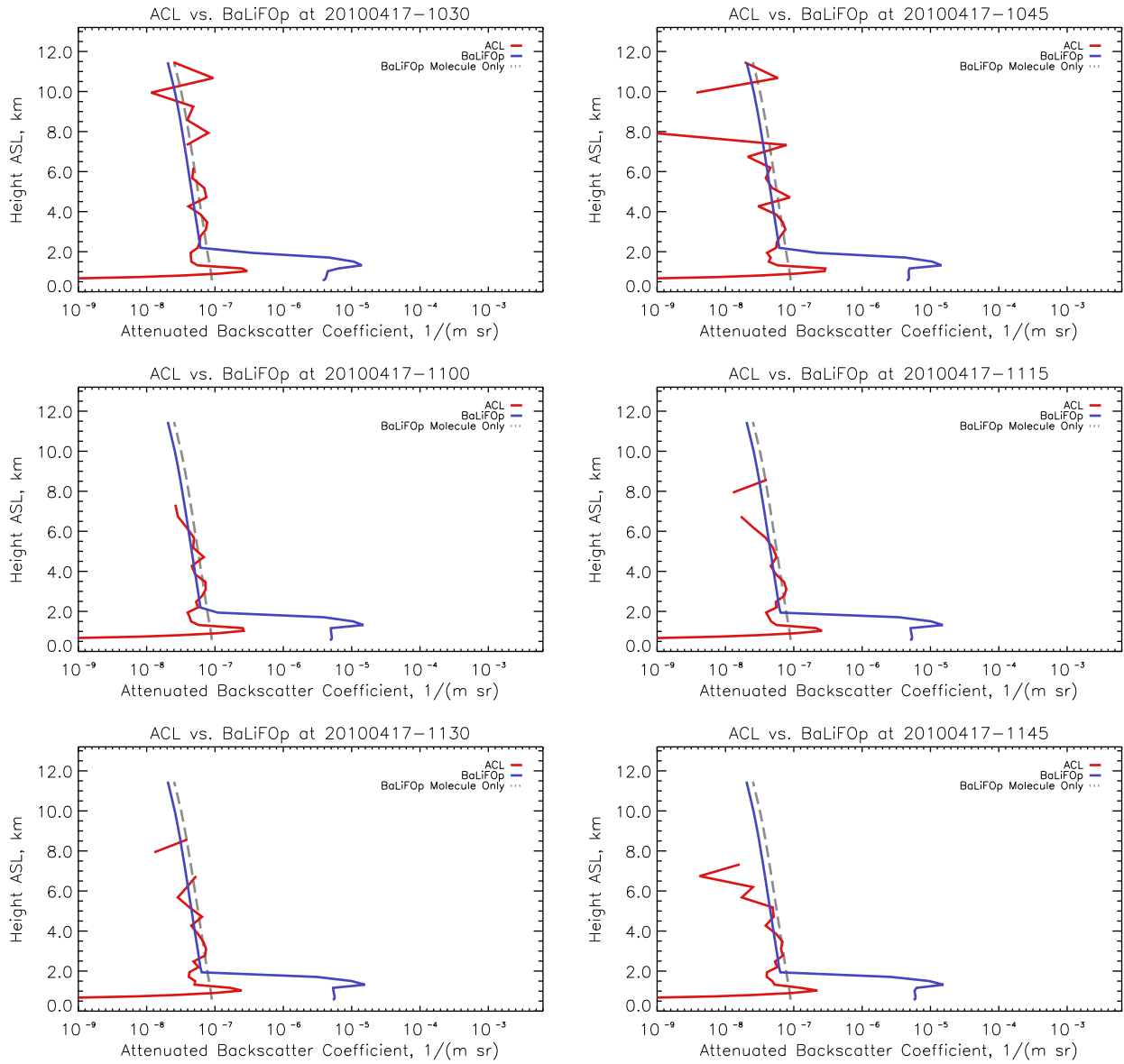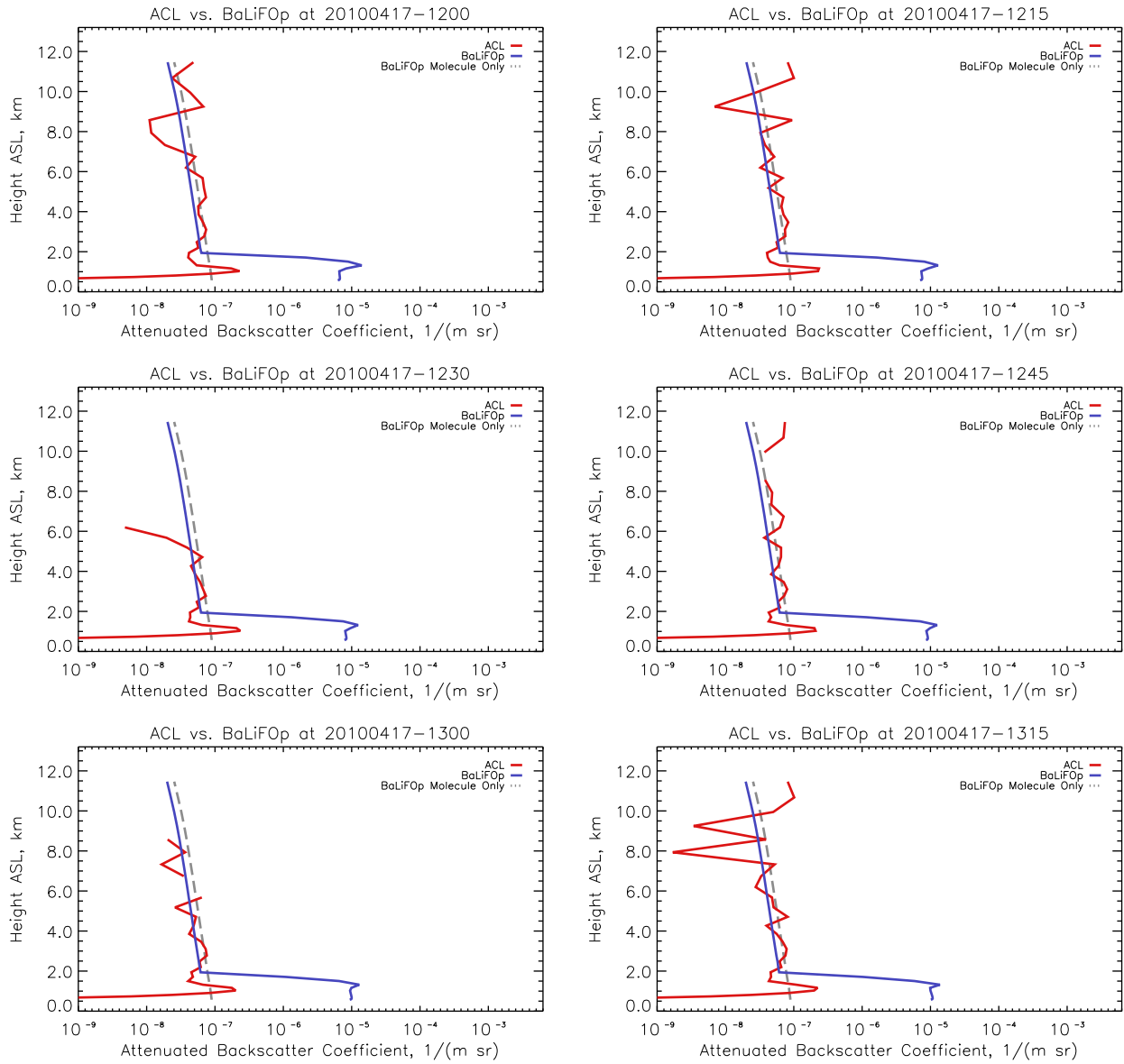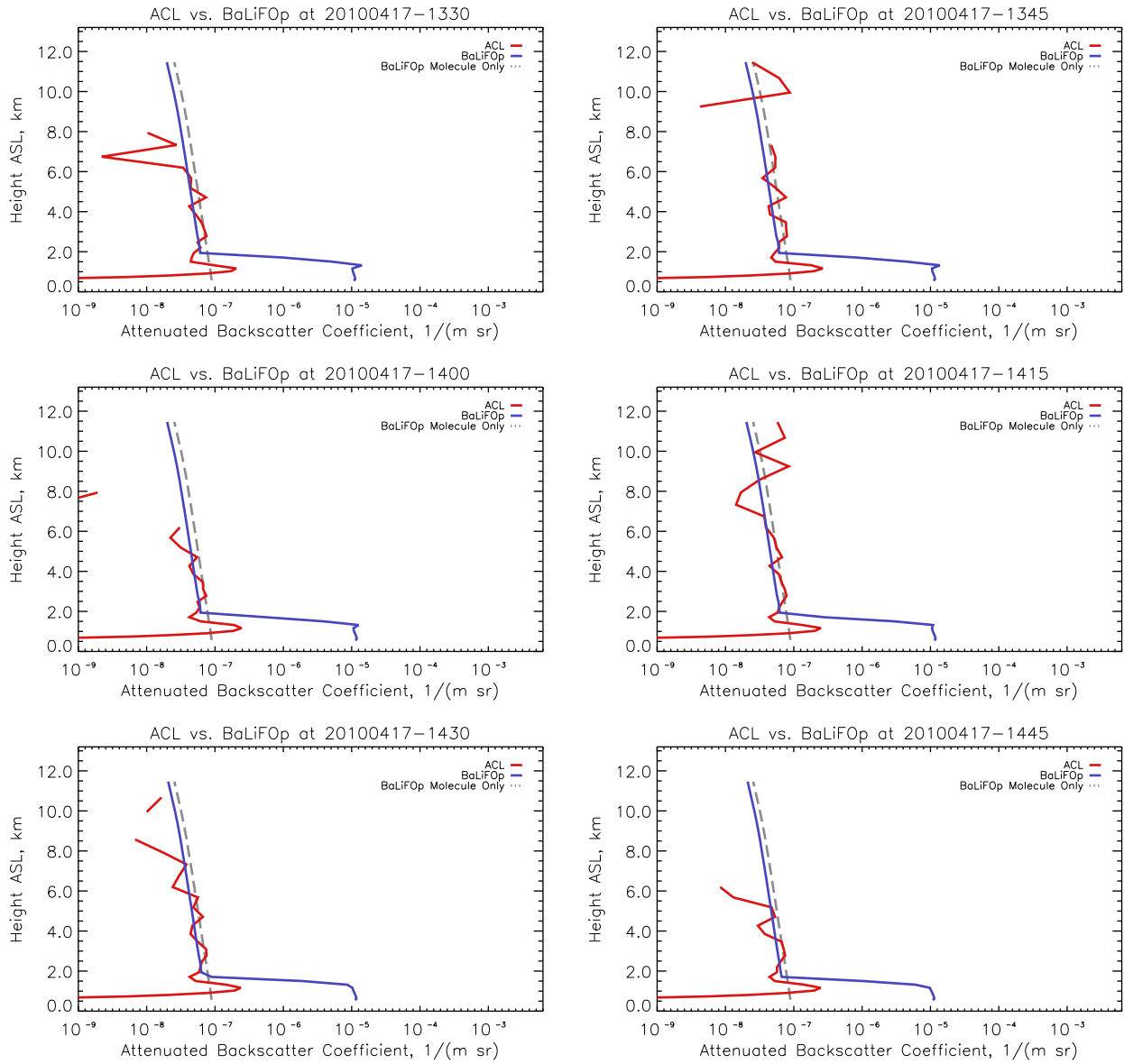Figure a.17: Vertical profiles from 17 April 2010, 12:00 to 13:15 UTC.

Figure a.18: Vertical profiles from 17 April 2010, 13:30 to 14:45 UTC.

REFERENCES

Ansmann, A. et al. (2010). "The 16 April 2010 major volcanic ash plume over central Europe: EARLINET lidar and AERONET photometer observations at Leipzig and Munich, Germany." In: *Geophysical Research Letters* 37.13. L13810, n/a–n/a. ISSN: 1944-8007. DOI: 10.1029/2010GL043809. URL: http://dx.doi.org/10.1029/2010GL043809.

Bangert, M. et al. (2012). "Saharan dust event impacts on cloud formation and radiation over Western Europe." In: *Atmospheric Chemistry and Physics* 12.9, pp. 4045–4063. DOI: 10.5194/acp-12-4045-2012. URL: http://www.atmos-chem-phys.net/12/4045/2012/.

Banta, Robert M. et al. (2012). "Doppler Lidar–Based Wind-Profile Measurement System for Offshore Wind-Energy and Other Marine Boundary Layer Applications." In: *American Meteorological Society* 51.2, pp. 327–349. URL: http://journals.ametsoc.org/doi/abs/10.1175/JAMC-D-11-040.1.

Behrendt, Andreas et al. (2002). "Combined Raman lidar for the measurement of atmospheric temperature, water vapor, particle extinction coefficient, and particle backscatter coefficient." In: *Appl. Opt.* 41.36, pp. 7657–7666. DOI: 10.1364/AO.41.007657. URL: http://ao.osa.org/abstract.cfm?URI=ao-41-36-7657.

Behrendt, Andreas et al. (2011). "A novel approach for the characterization of transport and optical properties of aerosol particles near sources – Part I: Measurement of particle backscatter coefficient maps with a scanning UV lidar." In: *Atmospheric Environment* 45.16, pp. 2795 –2802. ISSN: 1352-2310. DOI: http://dx.doi.org/10.1016/j.atmosenv.2011.02.061. URL: http://www.sciencedirect.com/science/article/pii/S1352231011002056.

Benedetti, A et al. (2009). "Aerosol analysis and forecast in the European Centre for Medium-Range Weather Forecasts Integrated Forecast System: 2. Data assimilation." In: *J. Geophys. Res.* 114.D13205. DOI: 10.1029/2008JD011115.

Buchholtz, Anthony (1995). "Rayleigh-scattering calculations for the terrestrial atmosphere." In: *Optical Society of America* 34.15, pp. 2765–2773.

Chaboureau, Jean-Pierre et al. (2011). "Long-range transport of Saharan dust and its radiative impact on precipitation forecast: a case study during the Convective and Orographically-induced Precipitation Study (COPS)." In: *Quarterly Journal of the Royal Meteorological Society* 137.S1, pp. 236–251. ISSN: 1477-870X. DOI: 10.1002/qj.719. URL: http://dx.doi.org/10.1002/qj.719.

Chen, Siyu et al. (2014). "Regional modeling of dust mass balance and radiative forcing over East Asia using WRF-Chem." In: *Aeolian Research* 15, pp. 15 –30. ISSN: 1875-

9637. DOI: http://dx.doi.org/10.1016/j.aeolia.2014.02.001. URL: http://www.sciencedirect.com/science/article/pii/S1875963714000056.

Cuevas, E. et al. (2015). "The MACC-II 2007–2008 reanalysis: atmospheric dust evaluation and characterization over northern Africa and the Middle East." In: *Atmospheric Chemistry and Physics* 15.8, pp. 3991–4024. DOI: 10.5194/acp-15-3991-2015. URL: http://www.atmos-chem-phys.net/15/3991/2015/.

Dacre, H. F., A. L. M. Grant, and B. T. Johnson (2013). "Aircraft observations and model simulations of concentration and particle size distribution in the Eyjafjallajökull volcanic ash cloud." In: *Atmospheric Chemistry and Physics* 13.3, pp. 1277–1291. DOI: 10.5194/acp-13-1277-2013. URL: http://www.atmos-chem-phys.net/13/1277/2013/.

Dagan, G. (2008). *Lidar - Range-Resolved Optical Remote Sensing of the Atmosphere*. Ed. by Claus Weitkamp. Springer Verlag Gmbh.

Draine, Bruce T. and Piotr J. Flatau (1994). "Discrete-Dipole Approximation For Scattering Calculations." In: *J. Opt. Soc. Am. A* 11.4, pp. 1491–1499. DOI: 10.1364/JOSAA.11.001491. URL: http://josaa.osa.org/abstract.cfm?URI=josaa-11-4-1491.

Emeis, S. et al. (2011). "Measurement and simulation of the 16/17 April 2010 Eyjafjallajökull volcanic ash layer dispersion in the northern Alpine region." In: *Atmospheric Chemistry and Physics* 11.6, pp. 2689–2701. DOI: 10.5194/acp-11-2689-2011. URL: http://www.atmos-chem-phys.net/11/2689/2011/.

Emeis, Stefan, Klaus Schäfer, and Christoph Münkel (2009). "Observation of the structure of the urban boundary layer with different ceilometers and validation by RASS data." In: *Meteorologische Zeitschrift* 18.2, pp. 149–154. DOI: 10.1127/0941-2948/2009/0365.

Flentje, H. et al. (2010a). "Aerosol profiling using the ceilometer network of the German Meteorological Service." In: *Atmospheric Measurement Techniques Discussions* 3.4, pp. 3643–3673. DOI: 10.5194/amtd-3-3643-2010. URL: http://www.atmos-meas-tech-discuss.net/3/3643/2010/.

Flentje, H. et al. (2010b). "The Eyjafjallajökull eruption in April 2010 – detection of volcanic plume using in-situ measurements, ozone sondes and lidar-ceilometer profiles." In: *Atmospheric Chemistry and Physics* 10.20, pp. 10085–10092. DOI: 10.5194/acp-10-10085-2010. URL: http://www.atmos-chem-phys.net/10/10085/2010/.

Gasteiger, J. et al. (2011a). "Volcanic ash from Iceland over Munich: mass concentration retrieved from ground-based remote sensing measurements." In: *Atmospheric Chemistry and Physics* 11.5, pp. 2209–2223. DOI: 10.5194/acp-11-2209-2011. URL: http://www.atmos-chem-phys.net/11/2209/2011/.

Gasteiger, Josef et al. (2011b). "Modelling lidar-relevant optical properties of complex mineral dust aerosols." In: *Tellus B* 63.4. ISSN: 1600-0889. URL: http://www.tellusb.net/index.php/tellusb/article/view/16372.

Haarig, M. et al. (2016). "1064 nm rotational Raman lidar for particle extinction and lidar-ratio profiling: cirrus case study." In: *Atmospheric Measurement Techniques* 9.9, pp. 4269–4278. DOI: 10.5194/amt-9-4269-2016. URL: https://www.atmos-meas-tech.net/9/4269/2016/.

Hammann, E. et al. (2015). "Temperature profiling of the atmospheric boundary layer with rotational Raman lidar during the HD(CP)^2 Observational Prototype Experiment." In: *Atmospheric Chemistry and Physics* 15.5, pp. 2867–2881. DOI: 10.5194/acp-15-2867-2015. URL: http://www.atmos-chem-phys.net/15/2867/2015/.

Kemppinen, O. et al. (2015). "Retrieving microphysical properties of dust-like particles using ellipsoids: the case of refractive index." In: *Atmospheric Chemistry and Physics* 15.19, pp. 11117–11132. DOI: 10.5194/acp-15-11117-2015. URL: http://www.atmos-chem-phys.net/15/11117/2015/.

Kokkalis, P. et al. (2013). "Optical, microphysical, mass and geometrical properties of aged volcanic particles observed over Athens, Greece, during the Eyjafjallajökull eruption in April 2010 through synergy of Raman lidar and sunphotometer measurements." In: *Atmospheric Chemistry and Physics* 13.18, pp. 9303–9320. DOI: 10.5194/acp-13-9303-2013. URL: http://www.atmos-chem-phys.net/13/9303/2013/.

Lange, Anne Caroline and Hendrik Elbern (2014). "Lidar data assimilation for improved analyses of volcanic aerosol events." In: *Geophysical Research Abstracts*. Vol. 16. EGU2014-5987. EGU General Assembly 2014.

Lathem, T. L. et al. (2011). "Hygroscopic Properties of Volcanic Ash." Geophysical Research letters.

M. Valdebenito B, Álvaro et al. (2011). "A novel approach for the characterisation of transport and optical properties of aerosol particles near sources – Part II: Microphysics–chemistry-transport model development and application." In: *Atmospheric Environment* 45.17, pp. 2981 –2990. ISSN: 1352-2310. DOI: http://dx.doi.org/10.1016/j.atmosenv.2010.09.004. URL: http://www.sciencedirect.com/science/article/pii/S1352231010007582.

Madonna, F. et al. (2013). "A study on the use of radar and lidar for characterizing ultragiant aerosol." In: *Journal of Geophysical Research: Atmospheres* 118.17, pp. 10,056–10,071. ISSN: 2169-8996. DOI: 10.1002/jgrd.50789. URL: http://dx.doi.org/10.1002/jgrd.50789.

Mallet, M. et al. (2009). "Impact of dust aerosols on the radiative budget, surface heat fluxes, heating rate profiles and convective activity over West Africa during March 2006." In: *Atmospheric Chemistry and Physics* 9.18, pp. 7143–7160. DOI: 10.5194/acp-9-7143-2009. URL: http://www.atmos-chem-phys.net/9/7143/2009/.

Mamouri, R. E. et al. (2012). "Multi-wavelength Raman lidar, sun photometric and aircraft measurements in combination with inversion models for the estimation of the aerosol optical and physico-chemical properties over Athens, Greece." In: *Atmospheric Measurement Techniques* 5.7, pp. 1793–1808. DOI: 10.5194/amt-5-1793-2012. URL: http://www.atmos-meas-tech.net/5/1793/2012/.

Matthias, Volker et al. (2012). "The ash dispersion over Europe during the Eyjafjal-lajökull eruption – Comparison of CMAQ simulations to remote sensing and air-borne in-situ observations." In: *Atmospheric Environment* 48.Supplement C. Volcanic ash over Europe during the eruption of Eyjafjallajöekull on Iceland, April-May 2010, pp. 184 –194. ISSN: 1352-2310. DOI: https://doi.org/10.1016/j.atmosenv.2011.06.077. URL: http://www.sciencedirect.com/science/article/pii/S1352231011007011.

Mie, Gustav (1908). "Beiträge zur Optik trüber Median, speziell kolloidaler Metallö-sungen." In: *Annalen der Physik*. DOI: 10.1002/andp.19083300302.

Mishchenko, Michael I. and Larry D. Travis (1998). "Capabilities And Limitations Of A Current Fortran Implementation Of The 1-matrix Method For Randomly Oriented, Rotationally Symmetric Scatterers." In: *Journal of Quantitative Spectroscopy and Radiative Transfer* 60.3, pp. 309–324.

Mishchenko, Michael I., Larry D. Travis, and Andrew A. Lacis (2002). *Scattering, Absorption, and Emission of Light by Small Particles*. Cambridge University Press.

Mona, L. et al. (2012). "Multi-wavelength Raman lidar observations of the Eyjafjal-lajökull volcanic cloud over Potenza, southern Italy." In: *Atmospheric Chemistry and Physics* 12.4, pp. 2229–2244. DOI: 10.5194/acp-12-2229-2012. URL: http://www.atmos-chem-phys.net/12/2229/2012/.

Morcrette, J.-J. et al. (2009). "Aerosol analysis and forecast in the European Centre for Medium-Range Weather Forecasts Integrated Forecast System: Forward modeling." In: *Journal of Geophysical Research: Atmospheres* 114.D6. D06206, n/a–n/a. ISSN: 2156-2202. DOI: 10.1029/2008JD011235. URL: http://dx.doi.org/10.1029/2008JD011235.

Mortier, A. et al. (2013). "Detection and characterization of volcanic ash plumes over Lille during the Eyjafjallajökull eruption." In: *Atmospheric Chemistry and Physics* 13.7, pp. 3705–3720. DOI: 10.5194/acp-13-3705-2013. URL: http://www.atmos-chem-phys.net/13/3705/2013/.

Pappalardo, G. et al. (2014). "EARLINET: towards an advanced sustainable European aerosol lidar network." In: *Atmospheric Measurement Techniques* 7.8, pp. 2389–2409. DOI: 10.5194/amt-7-2389-2014. URL: http://www.atmos-meas-tech.net/7/2389/2014/.

Radlach, M., A. Behrendt, and V. Wulfmeyer (2008). "Scanning rotational Raman lidar at 355 nm for the measurement of tropospheric temperature fields." In: *Atmospheric Chemistry and Physics* 8.2, pp. 159–169. DOI: 10.5194/acp-8-159-2008. URL: http://www.atmos-chem-phys.net/8/159/2008/.

Rieger, Daniel et al. (2014). "Impact of aerosol on post-frontal convective clouds over Germany." In: *Tellus B* 66.0. ISSN: 1600-0889. URL: http://www.tellusb.net/index.php/tellusb/article/view/22528.

Rocha-Lima, A. et al. (2014). "Optical, microphysical and compositional properties of the Eyjafjallajökull volcanic ash." In: *Atmospheric Chemistry and Physics* 14.19,

pp. 10649–10661. DOI: 10.5194/acp-14-10649-2014. URL: http://www.atmos-chem-phys.net/14/10649/2014/.

SIČ, Bojan (2014). "Amélioration de la représentation des aérosols dans un modèle de chimie-transport : Modélisation et assimilation de donnèes." PhD thesis. Université Toulouse.

Sandrini, S. et al. (2014). "In situ physical and chemical characterisation of the Eyjafjallajökull aerosol plume in the free troposphere over Italy." In: *Atmospheric Chemistry and Physics* 14.2, pp. 1075–1092. DOI: 10.5194/acp-14-1075-2014. URL: http://www.atmos-chem-phys.net/14/1075/2014/.

Schumann, U. et al. (2011). "Airborne observations of the Eyjafjalla volcano ash cloud over Europe during air space closure in April and May 2010." In: *Atmospheric Chemistry and Physics* 11.5, pp. 2245–2279. DOI: 10.5194/acp-11-2245-2011. URL: http://www.atmos-chem-phys.net/11/2245/2011/.

Shipley, S. T. et al. (1983). "High spectral resolution lidar to measure optical scattering properties of atmospheric aerosols. 1: Theory and instrumentation." In: *Appl. Opt.* 22.23, pp. 3716–3724. DOI: 10.1364/AO.22.003716. URL: http://ao.osa.org/abstract.cfm?URI=ao-22-23-3716.

Späth, F. et al. (2016). "3D Water Vapor Field in the Atmospheric Boundary Layer Observed with Scanning Differential Absorption Lidar." In: *Atmospheric Measurement Techniques Discussions* 2016, pp. 1–40. DOI: 10.5194/amt-2015-393. URL: http://www.atmos-meas-tech-discuss.net/amt-2015-393/.

Strohbach, Jens (Feb. 2015). "Ausbreitung der Eyjafjallajökull-Vulkanasche im April 2010 über Deutschland: Reanalyse der Ceilometermessungen des Deutschen Wetterdienstes." Bachelor Thesis.

Sugimoto, Nobuo et al. (2008). "Lidar network observations of tropospheric aerosols." In: *Lidar Remote Sensing for Environmental Monitoring IX*. Vol. 7153, 71530A–71530A–13. DOI: 10.1117/12.806540. URL: http://dx.doi.org/10.1117/12.806540.

Turner, D. D. et al. (2002). "Automated Retrievals of Water Vapor and Aerosol Profiles from an Operational Raman Lidar." In: *Journal of Atmospheric and Oceanic Technology* 19.

Vogel, B. et al. (2009). "The comprehensive model system COSMO-ART – Radiative impact of aerosol on the state of the atmosphere on the regional scale." In: *Atmospheric Chemistry and Physics* 9.22, pp. 8661–8680. DOI: 10.5194/acp-9-8661-2009. URL: http://www.atmos-chem-phys.net/9/8661/2009/.

Vogel, H. et al. (2014). "Time-lagged ensemble simulations of the dispersion of the Eyjafjallajökull plume over Europe with COSMO-ART." In: *Atmospheric Chemistry and Physics* 14.15, pp. 7837–7845. DOI: 10.5194/acp-14-7837-2014. URL: http://www.atmos-chem-phys.net/14/7837/2014/.

Waquet, F. et al. (2014). "Retrieval of the Eyjafjallajökull volcanic aerosol optical and microphysical properties from POLDER/PARASOL measurements." In: *Atmospheric*

Chemistry and Physics 14.4, pp. 1755–1768. DOI: 10.5194/acp-14-1755-2014. URL: http://www.atmos-chem-phys.net/14/1755/2014/.

Warren, Elliott et al. (2018). "Evaluation of forward-modelled attenuated backscatter using an urban ceilometer network in London under clear-sky conditions." In: *Atmospheric Environment*. ISSN: 1352-2310. DOI: https://doi.org/10.1016/j.atmosenv.2018.04.045. URL: http://www.sciencedirect.com/science/article/pii/S1352231018302760.

Weitkamp, Claus, ed. (2005). *Lidar, Range-Resolved Optical Remote Sensing of the Atmosphere*. Vol. 1. Springer Science + Business Media Inc.

Whiteman, D. N., S. H. Melfi, and R. A. Ferrare (1992). "Raman lidar system for the measurement of water vapor and aerosols in the Earth's atmosphere." In: *Appl. Opt.* 31.16, pp. 3068–3082. DOI: 10.1364/AO.31.003068. URL: http://ao.osa.org/abstract.cfm?URI=ao-31-16-3068.

Wiegner, M. et al. (2014). "What is the benefit of ceilometers for aerosol remote sensing? An answer from EARLINET." In: *Atmospheric Measurement Techniques* 7.7, pp. 1979–1997. DOI: 10.5194/amt-7-1979-2014. URL: http://www.atmos-meas-tech.net/7/1979/2014/.

Wiscombe, W. J. (1980). "Improved Mie scattering algorithms." In: *Optical Society of America* 19.

Wolke, Ralf et al. (2004). "Air Pollution Modeling and Its Application XVI." In: ed. by Carlos Borrego and Selahattin Incecik. Boston, MA: Springer US. Chap. The Chemistry-Transport Modeling System lm-Muscat: Description and citydelta Applications, pp. 427–439. ISBN: 978-1-4419-8867-6. DOI: 10.1007/978-1-4419-8867-6_39. URL: http://dx.doi.org/10.1007/978-1-4419-8867-6_39.

Wulfmeyer, Volker and Graham Feingold (2000). "On the relationship between relative humidity and particle backscattering coefficient in the marine boundary layer determined with differential absorption lidar." In: *Journal of Geophysical Research: Atmospheres* 105.D4, pp. 4729–4741. ISSN: 2156-2202. DOI: 10.1029/1999JD901030. URL: http://dx.doi.org/10.1029/1999JD901030.

Wulfmeyer, Volker et al. (2010). "Can Water Vapour Raman Lidar Resolve Profiles of Turbulent Variables in the Convective Boundary Layer?" In: *Boundary-Layer Meteorology* 136.2, pp. 253–284. ISSN: 1573-1472. DOI: 10.1007/s10546-010-9494-z. URL: http://dx.doi.org/10.1007/s10546-010-9494-z.

Wulfmeyer, Volker et al. (2015). "A review of the remote sensing of lower tropospheric thermodynamic profiles and its indispensable role for the understanding and the simulation of water and energy cycles." In: *Reviews of Geophysics* 53.3. 2014RG000476, pp. 819–895. ISSN: 1944-9208. DOI: 10.1002/2014RG000476. URL: http://dx.doi.org/10.1002/2014RG000476.

Young, Andrew T. (1981). "Rayleigh scattering." In: *Optical Society of America* 20.4, pp. 533–535.

Zakey, A. S., F. Solmon, and F. Giorgi (2006). "Implementation and testing of a desert dust module in a regional climate model." In: *Atmospheric Chemistry and Physics* 6.12, pp. 4687–4704. DOI: 10.5194/acp-6-4687-2006. URL: http://www.atmos-chem-phys.net/6/4687/2006/.

Zakšek, K. et al. (2013). "Monitoring volcanic ash cloud top height through simultaneous retrieval of optical data from polar orbiting and geostationary satellites." In: *Atmospheric Chemistry and Physics* 13.5, pp. 2589–2606. DOI: 10.5194/acp-13-2589-2013. URL: http://www.atmos-chem-phys.net/13/2589/2013/.

The supplement DVD provides code used and written for performing the sensitivity studies as well as running the forward operator itself including output Data of COSMO-ART and the relevant ACL stations.

Lebenslauf

Persönliche Daten

VORNAME / NACHNAME	Armin Geisinger
ADRESSE	Herzogenau 2, 73235 Weilheim an der Teck
TEL.	+49 1577 3305962
E-MAIL	armin.geisinger@uni-hohenheim.de
STAATSANGEHÖRIGKEIT	Deutsch
GEBURTSDATUM	30.09.1987
GESCHLECHT	Männlich

Ausbildung

ZEITRAUM	10/2007-12/2010
ART	**Bachelor-Studium** **Nachwachsende Rohstoffe und Bioenergie**
INSTITUTION	Universität Hohenheim
BACHELOR THESIS	"*Auswertung ausgewählter Messdatensätze des IPM Doppler-Radars von der internationalen Messkampagne COPS und Diskission der Ergebnisse unter Einbeziehung der Auswertungen des POLDIRAD*" (Note: 1,5)

ZEITRAUM	12/2010 - 04/2013
ART	**Master-Studium** **Erdsystemwissenschaft**
INSTITUTION	Universität Hohenheim
MASTER THESIS	"*Niederschlagsanalyse mit einem X-Band Doppler Radar*" (Note: 1,0)

ZEITRAUM	Seit 04/2013
ART	**Promotion** *Entwicklung eines Rückstreu-Lidar Vorwärtsoperators für Atmosphärenchemie- und Aerosoltransportmodelle*

Eidesstattliche Versicherung gemäß § 7 Absatz 7 der Promotionsordnung der Universität Hohenheim zum Dr. rer. nat.

1. Bei der eingereichten Dissertation zum Thema

   ………………………………………………………………………………………………..

   ………………………………………………………………………………………………..

   handelt es sich um meine eigenständig erbrachte Leistung.

2. Ich habe nur die angegebenen Quellen und Hilfsmittel benutzt und mich keiner unzulässigen Hilfe Dritter bedient. Insbesondere habe ich wörtlich oder sinngemäß aus anderen Werken übernommene Inhalte als solche kenntlich gemacht.

3. Ich habe nicht die Hilfe einer kommerziellen Promotionsvermittlung oder -beratung in Anspruch genommen.

4. Die Bedeutung der eidesstattlichen Versicherung und der strafrechtlichen Folgen einer unrichtigen oder unvollständigen eidesstattlichen Versicherung sind mir bekannt.

Die Richtigkeit der vorstehenden Erklärung bestätige ich: Ich versichere an Eides Statt, dass ich nach bestem Wissen die reine Wahrheit erklärt und nichts verschwiegen habe.

_____   _____
Ort und Datum   Unterschrift